AD-A255 616

FINAL TECHNICAL REPORT

A Time-Domain Study of the Relationship

Between Drive Force Time Bandwidth and Farfield

Acoustic Radiation

by

J. Adin Mann III
Daniel Kruger
Aerospace Engineering & Engineering Mechanics
Iowa State University
Ames, IA 50011

August 1992

DTIC
ELECTE
SEP 14 1992
S **A** **D**

92-24782

92 9 04 038

91 8

Radiated sound energy of a point-driven, fluid loaded,

cylindrical, spherically end-capped shell as a function of force

time duration and multiple pulse spacing

by

Daniel Henry Kruger

A Thesis Submitted to the

Graduate Faculty in Partial Fulfillment of the

Requirements for the Degree of

MASTER OF SCIENCE

Department: Aerospace Engineering and Engineering Mechanics
Major: Engineering Mechanics

Approved:

_____
In Charge of Major Work

_____
For the Major Department

_____
For the Graduate College

Iowa State University
Ames, Iowa

1992

TABLE OF CONTENTS

LIST OF FIGURES

LIST OF TABLES

ACKNOWLEDGEMENTS

I'd like to take this opportunity to express my very deep appreciation and gratitude to the following people for their contributions, support, and friendship: Dr. J. Adin Mann III, advisor and chairman of the committee, who showed unfathomable patience and provided invaluable insights and advice as well as the much needed kick in the pants; Dr. Jeffrey C. Huston, committee member, for providing wisdom, encouragement, computer use which greatly speeded the completion of this work, and for special projects when I most needed them; Dr. Donald R. Flugrad Jr., committee member, for helpful advice and constructive criticism; Gayle Fay, Sally Vandepol, and Tammy Boyd, department secretaries, for their kind assistance; and Matthew Carney, Michael Sellberg, Dennis Cronin, and Joel Kness who provided helpful comments, encouragement, fellowship, and some much needed comic relief. Special thanks to Chili and Rhonda for all of the computer help.

I especially want to thank my wife, Cheryl, for all of her love, support, and understanding during the completion of this work. Also, I want to thank my parents, Henry and Deanna, and my brother Larry for their love and support, and above all, always believing in me. Thanks also to Laurin, Esther, and Bryan Eichhorn for their support and spiritual guidance.

Finally, I would like to thank Earl G. Williams and the Naval Research Laboratory of Washington, D. C., for sponsoring this research.

1

CHAPTER 1

INTRODUCTION

Interaction between a vibrating cylindrical shell and a surrounding fluid is of keen interest to many acousticians working in structural acoustics. Much analysis has been done on the scattering and radiation properties of such a system in the frequency domain. However, these analyses rarely consider the shell - fluid interaction in the time domain. Hence, the main objecive of this thesis is to examine energy radiated by a fluid loaded, point driven, finite cylindrical shell in the time domain.

Due to the cost in both time and resources, relatively few measurements are available for study in the time domain. Thus, transfer functions for the acoustic pressure and acoustic velocity in the radial direction of the shell obtained via Nearfield Acoustical Holography were provided for study by the Naval Research Laboratory of Washington, D. C. A Linear system model and signal processing techniques were employed at Iowa State University to simulate the acoustic pressure and normal acoustic velocity at the shell surface for numerous point excitations. Then integration techniques were used to obtain the total energy radiated by the shell for a given excitation. This quantity was then normalized by the amount of energy input by the forcing function to yield the fraction of input energy radiated to the farfield. Along the way, active acoustic intensity and impulsive power of the shell were examined as a means to gain physical insight to variations in the percent of input energy radiated by the shell. The work on this thesis began with the problem of implementing the linear system model on a new computer system at Iowa State University.

Though acoustic pressure and velocity were recreated by using a linear system model for the interaction between the shell and the fluid, the calculation of normalized energy radiated to the farfield by the forcing function producing this pressure and velocity is not linear. The idea that this quantity could be influenced in a way that is not linear by varying the

time duration of single excitation forces, as well as the time spacing between multiple shell excitations, served as inspiration for the work performed in this thesis.

It is worth noting that performing the research via computer simulation and linear system model techniques instead of actually performing all of the measurements on a fluid loaded shell saved a great deal of time. Performing a measurement in a fluid loaded environment and calculating all of the desired quantities for the entire shell can take up to three or four days. A simulation, however, only requires about two hours of computer time. Thus, obtaining the results in this thesis would have taken about five years longer if all of the measurements were done in real life instead of by computer simulation. What's more, facilities and equipment for performing the actual measurements is costly and only exists at a few research facilities. Simulating the shell response requires only computer equipment that is readily available at almost any facility.

One major goal of this thesis was to explain the relationship between the pulse time duration of the forcing function and the normalized energy radiated by the shell. The second major goal was to create a model for the behavior of the normalized energy radiated by the shell when the spacing between multiple pulse forcing functions was varied. Overall, it was desired to be able to design forcing functions to fit specific normalized energy prameters, particularly, minimizing the normalized energy radiated by the shell.

Achieving these goals will aid in understanding actual physical phenomena which occur inside cylindrical shells. Events that could be modeled by this analysis include operation of a motor, opening and closing of valves, and rotation of a propulsion device.

Also, this analyis can be extrapolated to other physical systems which do not consist of cylindrical shells. Almost any system with a periodic or repetitive excitation, such as engine valves opening, can be thought of in terms of the analysis done in this thesis. Other system that could be modeled include ventilation or air-conditioning ducts with fans, air compressor valves, and even assembly line machines.

Chapter 2 develops the linear system model technique for the specific shell geometry studied in this research. Assumptions used in employing a linear system model, as well as its advantages and disadvantages are discussed.

Chapter 3 briefly describes the role of Nearfield Acoustical Holography and the specific parameters for its use in this research.

Chapter 4 details the aspects of implementing fast Fourier transforms on the data provided for this research. Specific concerns include proper reconstruction of the transfer function spectra provided for the work, filtering, and zeropadding.

Chapter 5 introduces the Gaussian time window force. Parameters and equations are explained and developed for single and multiple pulse forces in both the time and frequency domains. Proper force spectra for use in FFT algorithms and examples of the force in the time domain are shown.

Chapter 6 explains how various quantities are calculated from the computer simulated acoustic pressure and normal velocity. Quantities studied include normalized energy as a function of single pulse time spacing and multiple pulse time spacing, acoustic intensity as a function of frequency, and the impulsive sound power radiated by the shell as a funciton of frequency.

Chapter 7 includes the results from two studies that were done. Normalized energy vs. single pulse force time duration for four shell areas is explored first. Then the results from varying multiple pulse time spacing for the same four areas are discussed. Physical insight to the fluid - shell interaction is gained by studying the active intensity. Finally, models to explain both sets of results are developed using the impulsive power spectrum.

Chapter 8 summarizes results, explains the conclusions, and makes recommendations for further work. Some criteria for develping forcing functions that produce specific normalized energy results are discussed, and recommendations on how to develop better impulsive power spectrum models are made.

CHAPTER 2

LINEAR SYSTEM MODEL

Perhaps the most fundamental concept employed in this research is the use of a single input - single output linear system model. The acoustic field around a fluid loaded, point driven, finite cylindrical shell with spherical end caps is described via such a model. In a linear system, a single input $f(t)$ is operated upon by a transfer function $h(\tau)$ in order to produce an output field quantity $y(t)$. All three quantities may be thought of as either functions of time or functions of frequency. In this research, a point driving force is operated on by the fluid loaded cylindrical shell which produces, in turn, the field quantities of acoustic pressure and velocity. A symbolic diagram of the linear system is shown in Figure 2.1.
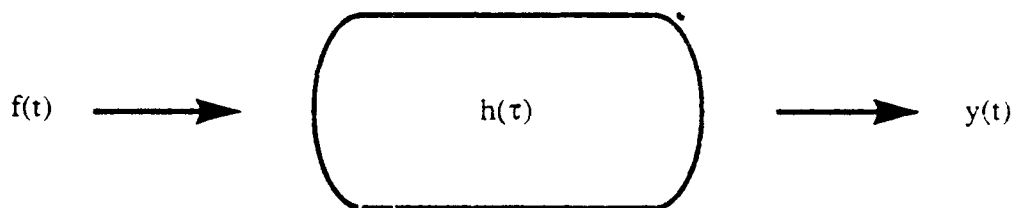
Figure 2.1: A single input - single output linear system model

One important characteristic of such a system is that it adheres to the principle of superposition. For example, presume a quantity $y(t)$ is produced by the simultaneous operation on two excitations, $f_1(t)$ and $f_2(t)$, by $h(\tau)$. Assume further that if $f_1(t)$ and $f_2(t)$ were operated on by the transfer function separately, the field quantities produced would be $y_1(t)$ and $y_2(t)$, respectively. In a linear system, $y(t)$ would be equal to the algebraic sum of $y_1(t)$ and $y_2(t)$.

A second important property of linear systems is time shift invariance. This means that

if, for a given excitation f(t), the result is y(t), the y(t) is independent of when f(t) was applied to the system. That is, the resulting field quantity will be the same whether the excitation is applied today, tomorrow, or next week, except the result will be time shifted.

And finally, a linear system model can be described mathematically by a convolution integral. When the input excitation, f(t) is operated on by the transfer function of the system, $h(\tau)$, the response of the system, y(t) is calculated by

$$y(t) = \int_{-\infty}^{\infty} h(\tau)f(t-\tau)d\tau, \qquad (2.1.1)$$

the convolution integral in the time domain. According to the literature, the convolution process can be carried out much more rapidly and efficiently as a simple multiplication if all three system quantities are calculated as a function of frequency via the Fourier transform integral. Equation (2.1.2),

$$H(f) = \int_{-\infty}^{\infty} h(\tau)e^{2j\pi f\tau}d\tau \qquad (2.1.2)$$

is the form of the Fourier integral used to calculate the transfer function as a function of frequency. For the purpose of clarity, $h(\tau)$ will be referred to as the impulse response function of the linear system and H(f) will be referred to as the transfer function, or frequency response function for the system, although the terms are sometimes used interchangeably in the literature.

Once the linear system response and the input excitation as functions of frequency, Y(f) and F(f), respectively, are obtained via use of Equation (2.1.2), the convolution integral in the time domain becomes,

$$Y(f) = H(f)F(f), \qquad (2.1.3)$$

an easy multiplication in the frequency domain. A desired field quantity can then be calculated as a function of time via the inverse Fourier transform integral. In this research, the form

shown below,

$$y(t) = \int_{-\infty}^{\infty} Y(f)e^{-2j\pi ft}\,dt, \qquad (2.1.4)$$

was used for the inverse Fourier transform.

Describing the shell structure which these equations were performed on in this research necessitates some slight modification of the linear system model notation. For instance, excitation of the system may occur at almost any location on the shell. To allow for this fact, all three system properties, whether written as functions of time or frequency, are also written as functions of x_0, the position on the shell where excitations are input. Further, the operation of the impulse response on the input excitation, as well as the resulting acoustic field quantity, are functions of where on the shell they are observed. The variable x is used to denote this characteristic. Thus $F(f, x_0)$, $H(f, x_0, x)$ and $Y(f, x_0, x)$ represent the three system components in the frequency domain and $f(t, x_0, x)$, $h(\tau, x_0, x)$, and $y(t, x_0, x)$ describe them in the time domain. Figure 2.2 shows this idea in the time domain a little more clearly.

$\bullet\, y(t, x_0, x_1)$

$\bullet\, y(t, x_0, x_2)$
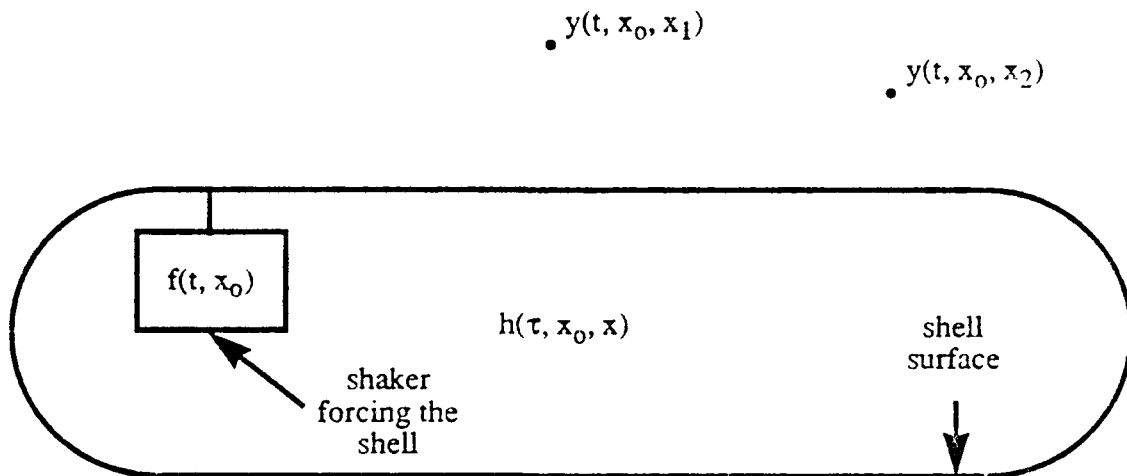
Figure 2.2: Specific linear system model for the shell in this research

In actual practice, the driving force as a function of time is known, or can he measured or calculated, as can field quantities such as acoustic pressure or velocity. Then, their frequency domain counterparts are calculated by Fast Fourier Transform (FFT) - the discrete, computerized algorithm for performing Equation (2.1.2). Finally, Equation (2.1.3) can be manipulated to obtain the transfer function,

$$H(f, x_o, x) = \frac{Y(f, x_o, x)}{F(f, x_o)}, \tag{2.1.5}$$

for the shell being studied. An inverse FFT - the discrete computerized method of performing Equation (2.1.4) - can then be used to calculate the impulse response for the system, $h(\tau, x_o, x)$, if desired.

For ideal accuracy and ease of calculation of the transfer function , the shell should be driven by a unit impulse forcing function (Tse et al. 53). The Dirac delta function, which will be denoted $\delta(t, x_o)$ for the described shell model, is such an impulse function (Bendat and Piersol 15). According to the literature, the Dirac delta has a Fourier transform, denoted $\delta(f, x_o)$, which is equal to one for all frequencies from minus infinity to infinity. This allows Equation (2.1.5) to reduce to

$$H(f, x_o, x) = Y(f, x_o, x) \tag{2.1.6}$$

for an excitation $\delta(t, x_o)$.

In reality, it is not possible to create a mechanical device which can produce a $\delta(t, x_o)$ input on the shell. Some other impulsive force $f_o(t, x_o)$ is used to create a response $y_o(t, x_o, x)$ for determination of the system transfer function using Equation (2.1.6). An excitation may be considered sufficiently impulsive for use in Equation (2.1.6) if its total time duration is much less than the period of any natural resonance frequency of the shell. Because little is usually known about such aspects of shells before the initial determination of $H(f, x_o, x)$, Equation (2.1.5) is typically used with the original measurement force, $f_o(t, x_o)$, and the resulting

acoustic pressure or velocity, $y_0(t, x_0, x)$ inserted. Two frequency response functions, one for acoustic velocity and one for acoustic pressure, were calculated via the linear system model method for use in this research. In the remainder of this thesis, they are denoted as $H_v(f, x_0, x)$ and $H_p(f, x_0, x)$, respectively. Further, the notation used in this paragraph for the forcing function (subscript o) and its resulting response will be used *only* when referring to the quantities used in the initial determination of the system transfer functions in the remainder of this thesis.

By definition of a linear system and the calculations it facilitates, the acoustic pressure or velocity for any synthetic force, F_{syn}, is then computed by

$$P_{syn}(t, x_o, x) = FFT^{-1}[H_p(f, x_o, x)F_{syn}(f, x_o)], \qquad (2.1.7)$$

or

$$V_{syn}(t, x_o, x) = FFT^{-1}[H_v(f, x_o, x)F_{syn}(f, x_o)], \qquad (2.1.8)$$

where the subscript p denotes the pressure transfer function, the subscript v denotes the velocity transfer function, the subscript o denotes the point x where the force is applied, and the subscript "syn" indicates that a quantity is simulated as a result of computer application of a synthetic force. A primary advantage of the linear system model is that it allows acoustic fields to be generated for numerous shell excitations while requiring only one initial measurement to be performed on an actual fluid loaded, point driven shell. Due to the fact that a computer simulation done by using Equations (2.1.7) and (2.1.8) is much faster than performing a measurement, tremendous savings of time and resources is another major advantage of the model. Finally, this method is much more convenient because only a few facilities capable of producing such acoustic measurements exist.

An important limitation on the linear model does, however, exist. Because the components of a given system used in Equation (2.1.5) exist only at a finite number of discrete

frequencies in an actual measurement, the division of the response by input force is done frequency by frequency. Specifically, this means that only frequencies where $F_0(f, x_0)$ exists can be calculated for a desired transfer function. At all other frequencies, the force has a value near zero, which would result in very inaccurate results at these frequencies for $H_{(p \text{ or } v)}(f, x_0, x)$.

More specific information on the role of acoustical holography and FFTs in implementation of the linear system model will follow.

CHAPTER 3

ROLE OF NEARFIELD ACOUSTICAL HOLOGRAPHY (NAH)

Nearfield acoustical holography (NAH) is the method used to determine all unknown desired quantities in the linear system model. Theory and implementation methods of NAH are thoroughly discussed in the literature (Williams et al.), therefore only a brief overview of how data was obtained for this research project will be given.

The NAH method requires simultaneous measurement of the driving force at x_0 and the acoustic pressure at many points x in the fluid. For a cylindrical geometry, a force transducer produces a time history of the input force. At the same time, a robotic arm fitted with a hydrophone, and a device for rotating the shell about its central axis measure the acoustic pressure at each point of a predefined cylindrical measurement grid in the acoustic nearfield of the fluid (Washburn et al.). In terms of the linear system model, $f_0(t, x_0)$ is the force measured by the transducer and $y_0(t, x_0, x)$ is the time record of the acoustic pressure measured by the hydrophone at a large number of points x on the grid. Next, an FFT is performed on $f_0(t, x_0)$ and then on $y_0(t, x_0, x)$ at every point on the measurement surface. The resulting pressure spectra, $Y_0(f, x_0, x)$, and the force spectrum $F_0(f, x_0)$, are then substituted into Equation (2.1.5) for each point x to calculate the pressure transfer function, $H_p(f, x_0, x)$, frequency by frequency. The frequency response function can then be subjected to an inverse FFT algorithm to produce the pressure impulse response function, $h_p(\tau, x_0, x)$, at each point x in the measurement. In general, both functions are also a function of r_m, where r_m is the radial distance of the hydrophone from the central axis of the cylinder. Also, r_m must be greater than r_0, the radius of the shell, and less than r_1, the radial distance from the axis which is determined to be the limit of the acoustic nearfield. Thus, the frequency response function is written as $H_p(f, x_0, x, r_m)$, and the impulse response is denoted as $h_p(\tau, x_0, x, r_m)$.

Next the NAH method uses an inversion of the Helmholtz-Huygen integral for

cylindrical geometry to produce a pressure transfer function at any desired radius r_h such that

$r_o \leq r_h$. A symbolic diagram is given in Figure 3.1. Along with the $H_p(f, x_o, x, r_h)$
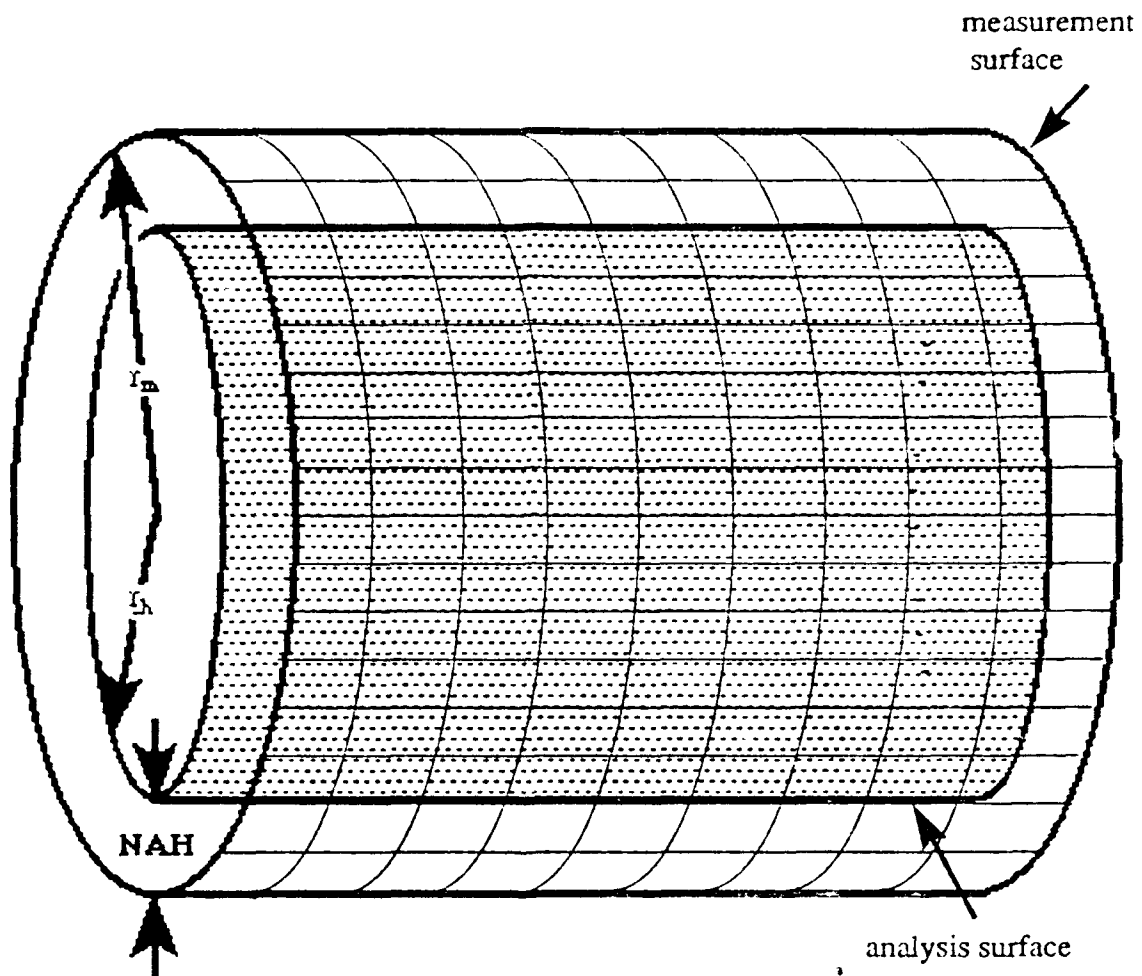
Figure 3.1: Symbolic diagram of NAH process

hologram, a velocity transfer function, denoted $H_v(f, x_o, x, r_h)$, is calculated. The NAH method only provides the velocity transfer function for velocity in the radial (normal to the shell surface) direction.

The holograms for the r_h equal to r_o were provided by the Naval Research Laboratory (NRL) in Washington, D. C. Pressure was measured at sixty-four locations in the axial direction of the shell and sixty-four points around the circumference of the shell. For each of the resulting 4096 spacial locations, 2048 time samples spaced forty microseconds apart were recorded. The radius, r_o, of the shell was 5.54 cm, and the grid points were spaced 0.84 cm apart in the axial direction of the shell. Further, the circumferential points were spaced evenly throughout the 2π radian circumference of the shell. The cylindrical shell occupied space from axial point nineteen to point forty-five, with eighteen extra points on each end.

Since $F_o(f, x_o)$ only existed from about 2kHz to 8kHz in the original measurement, only 508 of the possible 2048 frequencies were stored for each point x in the holograms. Explanations of the terms in the preceding paragraph, as well as reconstruction of a 2048 bin spectrum for each x, will be discussed in the next chapter.

CHAPTER 4

FFT IMPLEMENTATION

4.1. Overview

As was stated in the previous section, transfer functions for acoustic pressure and radial acoustic particle velocity consisting of sixty-four axial points, sixty-four circumferential points, and 508 frequency bins at each of these 4096 (64x64) grid points, were obtained via the linear system model and NAH for a cylindrical shell. The initial measurement was done with a sampling rate of 25 kHz and 2048 time sample points, resulting in a forty microsecond spacing between time samples for $f_0(t, x_0)$ and $y_0(t, x_0, x)$. According to Fourier transform theory, the resulting frequency response functions will contain 2048 frequencies ranging from 0-25 kHz with a 12.207 Hz (Bracewell 189-94).

The number of meaningful frequencies in $H_p(f, x_0, x)$ and $H_v(f, x_0, x)$ (the dependence on r is now dropped from the notation, since all spectra will occur at $r = r_0$ from here on) is reduced to 1024 because the Nyquist cutoff frequency, denoted f_c, is 12.5 kHz (half the sampling frequency). The Nyquist frequency has this effect because for a given sampling rate and number of sample points, the sample values for a frequency f_1 will have the same magnitude, and thus appear to be the same frequency to an FFT, as another frequency $f_2 = 2f_c - f$, only the two frequencies will appear 180 degrees out of phase. This phenomenon is called aliasing.

A simple analogy for aliasing is shown in Table 1. Because FFTs used in this research compute spectra with complex values, the value of the frequency f_1 above, denoted simply as g_1, can be thought of as having a real part and an imaginary part such that $g_1 = \cos 2\pi f_1 t + i \sin 2\pi f_1 t$. Similarly, $g_2 = \cos 2\pi f_2 t + i \sin 2\pi f_2 t$, where $f_2 = 2f_c - f$, as in the preceding paragraph. $\sin(2\pi f_1 t)$, $\sin[2\pi(2f_c - f_1)t]$, $\cos(2\pi f_1 t)$, and $\cos[2\pi(2f_c - f_1)t]$ values for a time spacing of 40 microseconds and an arbitrary f_1 of 6000 Hz are given. Opposite

signs and equal magnitudes on the sine terms and equal cosine terms in the table indicate that the two signals are the same frequency only 180 out of phase. Note that the linear magnitude of the two g terms (the square root of the sum of the sine and cosine parts squared) is equal. The main idea is that g_1 and g_2 are complex conjugates of each other.

Table 1: Aliasing analogy values for f = 6 kHz and f_c = 12.5 kHz

Time t, μsec	0.0	40.0	80.0	120.0	160.0	200.0	240.0	280.0
$\cos(2\pi ft)$	1.0	0.063	-0.992	-0.187	0.968	0.309	-0.929	-0.426
$\cos[2\pi(2f_c\text{-}f)t]$	1.0	0.063	-0.992	-0.187	0.968	0.309	-0.929	-0.426
$\sin(2\pi ft)$	0.0	0.998	0.125	-0.982	-0.249	0.951	0.368	-0.904
$\sin[2\pi(2f_c\text{-}f)t]$	0.0	-0.998	-0.125	0.982	0.249	-0.951	-0.358	0.904

Because $F_o(f, x_o)$ only existed from 2 - 8 kHz, only these frequencies could be accurately obtained for the two transfer functions using Equation (2.1.5). This is because values of the initial driving force for frequencies outside this range are very close to zero, and would cause large errors if divided into $Y_o(f, x_o, x)$. As a result, only 508 meaningful frequencies remain in the spectra, ranging from 1953.125 to 8142.069 Hz for each measurement point in the pressure and velocity holograms provided by NRL. Figures 4.1 and 4.2 show the magnitude of $H_p(f, x_o, x)$ and $H_v(f, x_o, x)$ for the driver point, x_o (axial point 25, circumferential point 33) on the shell. This point was chosen because it tends to dominate sound radiation in the results.

4.2. Spectral Reconstruction

In order to multiply synthetic force spectra by the transfer function spectra for the purpose of simulating sound radiation for the shell, the 508 point spectra provided must be reconstructed into spectra of 2048 frequencies. Once again, the 2048 points are mandated by the original measurement situation - all transfer functions and impulse response functions must have the same number of points, with the same spacing, as the original measurement.
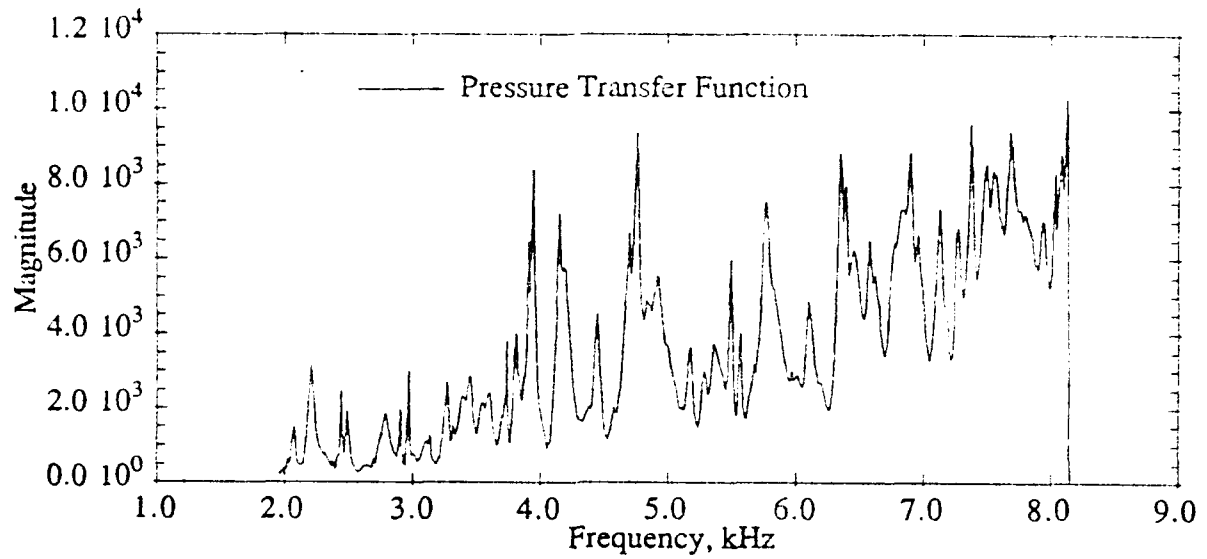
Figure 4.1: Original 508 frequencies of $H_p(f, x_o, x_o)$ obtained from NRL
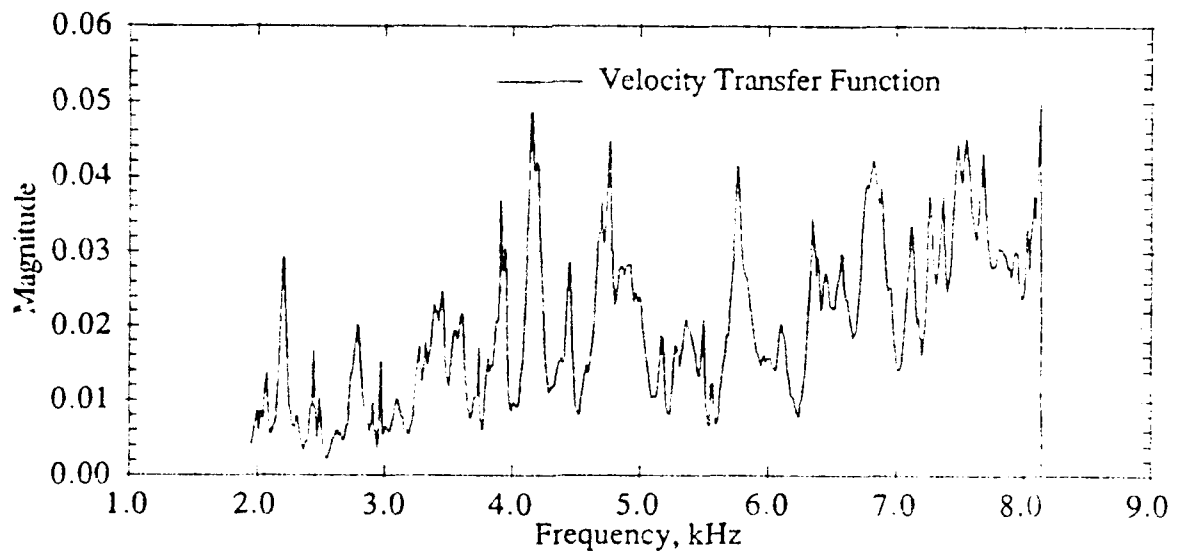
Figure 4.2: Original 508 frequencies of $H_v(f, x_o, x_o)$ obtained from NRL

When beginning this process, it is helpful to note some properties of FFT algorithms as they are carried out by computer. Most FFTs take an input array of N (2048 in this research) time points and return an array of N frequency coefficients. If both arrays are passed to the FFT as complex values, the phase shift of each frequency of the returned array is also given. Typically, the first bin of this returned array contains a zero hertz value, or DC offset, which has no corresponding alias frequency. The next $N/2$ frequency bins contain all frequencies up to the Nyquist cutoff, f_c. Thus, f_c is placed in the $N/2 + 1$ bin of the array. Finally, the alias frequencies are placed in bins $N/2 + 2$ to N with the relationship described in Equation (4.2.1),

$$([H_{(p \, or \, v)} \, (f, x_o, x)]_{i+1} = [H_{(p \, or \, v)} \, (f, x_o, x)]^*_{N-i+1}) \quad (i=1,\dots,N/2-1) \, . \qquad (4.2.1)$$

* Denotes complex conjugate.

The equation is a result of the fact that Fourier series theory presumes data given to an FFT are periodic functions which repeat every N points (Bendat and Piersol 11-13). Further, each value at a given bin i is the complex conjugate of the value at the bin $N/2 + i$. Realizing these facts about FFTs, the provided spectra were constructed into 2048 bin spectra for each of the 4096 hologram points by first placing each of the 508 given frequencies in the proper slots from zero hertz up to f_c. This corresponds to bins 161 through 668 in a 2048 point spectra. Finally, the alias frequencies are placed in bins 1382 through 1890, according to Equation (4.2.1). The resulting spectra for the driver point are shown in Figures 4.3 and 4.4 for comparison to Figures 4.1 and 4.2, respectively.

4.3. Need to Time Shift Data

When the calculation of the two transfer functions was performed, the starting time of the force excitation, and thus the pressure and velocity of the system, was lost. Because this starting time appears as a phase shift in the frequency domain and is the same for the inputforce as it is for pressure or velocity, it is divided out when Equation (2.1.5) is performed. As a result, no start or end of the signal is apparent when the transfer functions are
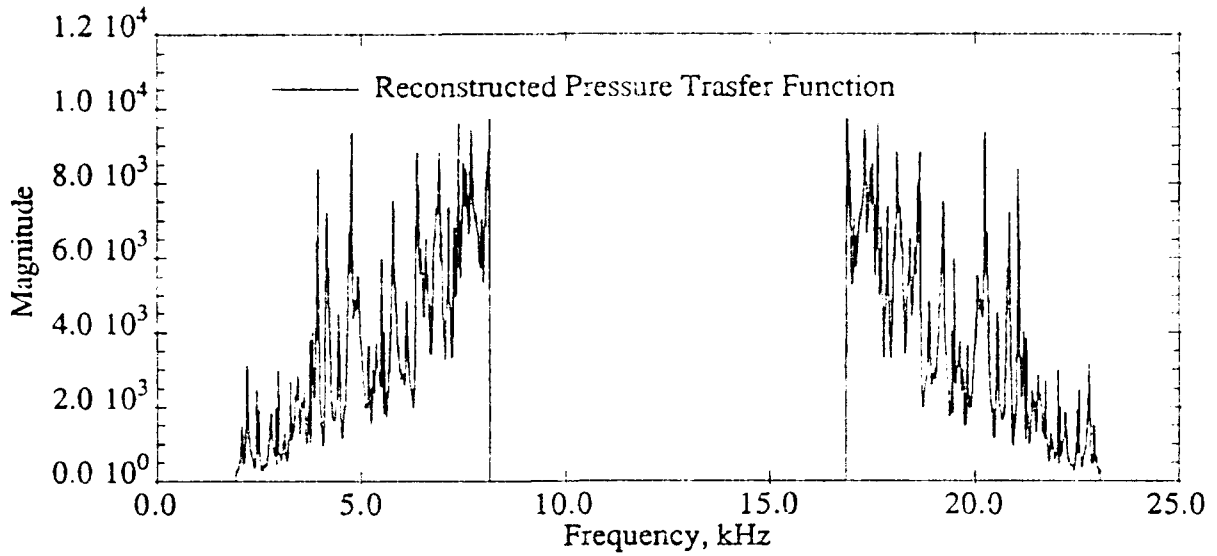
Figure 4.3: 2048 bin $H_p(f, x_0, x_0)$, reconstructed via Equation (4.2.1) for the driver point, x_0
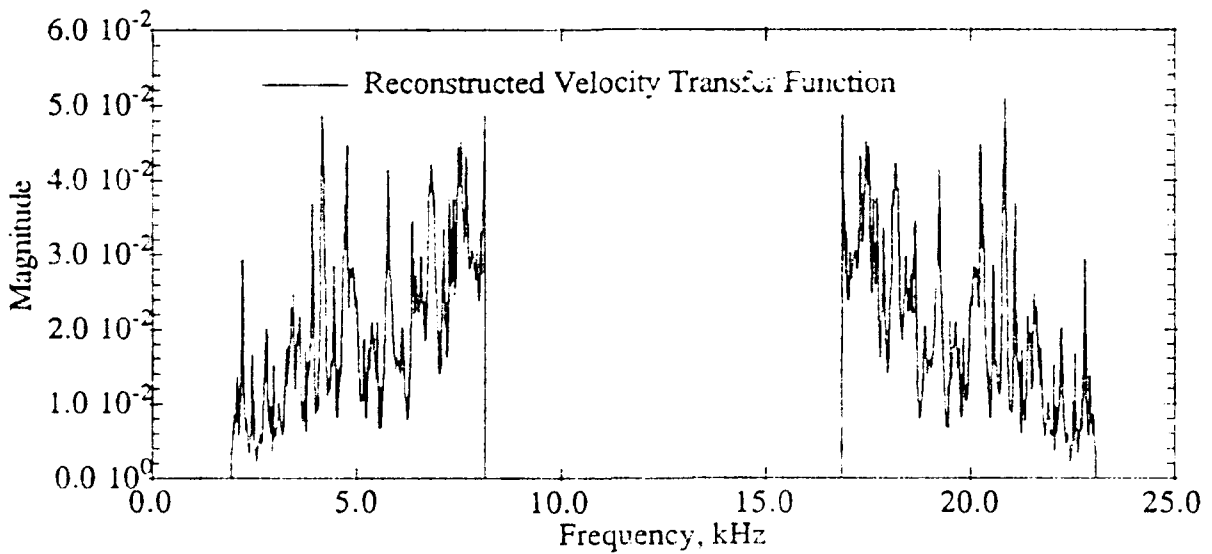
Figure 4.4: 2048 bin $H_v(f, x_0, x_0)$, reconstructed via Equation (4.2.1) for the driver point, x_0

again transformed to the time domain. Figure 4.5 demonstrates this fact for the pressure and Figure 4.6 demonstrates for the velocity impulse response functions for the driver point. These are obtained by taking the inverse Fourier transform of $H_p(f, x_o, x)$ and $H_v(f, x_o, x)$.
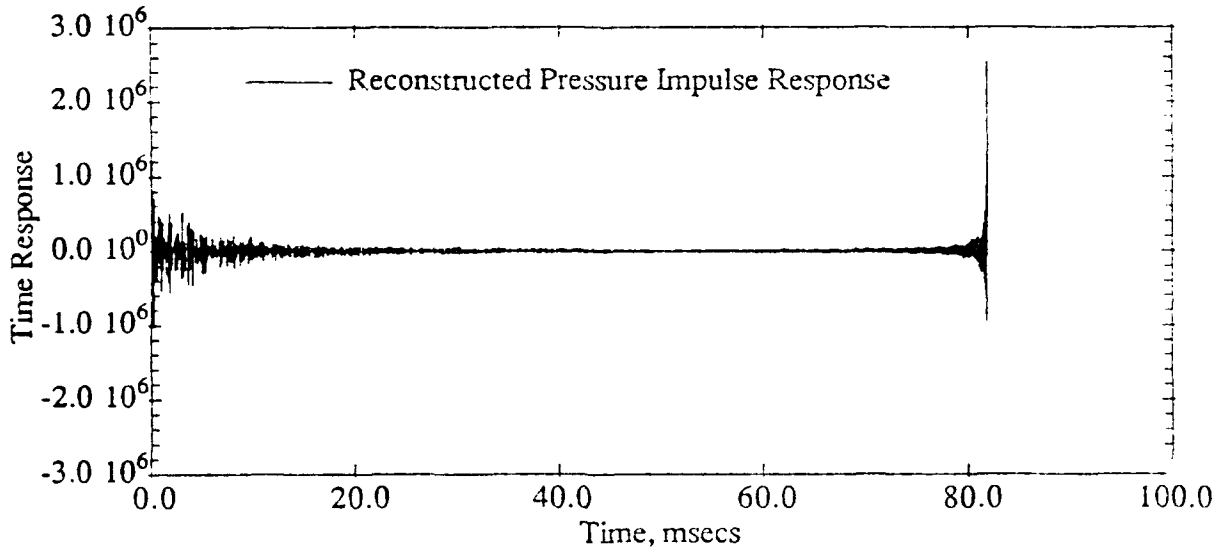
Figure 4.5: Pressure impulse response $h_p(\tau, x_o, x_o)$ without time shifting

It is now necessary to time shift the data by an appropriate amount. A 121 tap Kaiser-Bessel filter was recommended by NRL and used in this project, which resulted in a time shift, denoted t_o, equal to sixty-one time bins. Thus, t_o was 2.44 milliseconds. As will be demonstrated later, this time shift is very important for applying synthetic forces to the data, whether performing the convolution in time or the multiplication in frequency. Time shifting the data is performed as in Equation (4.3.1),

$$h_{(p \, or \, v)}(\tau, x_o, x) = FFT^{-1}[H_{(p \, or \, v)}(f, x_o, x) \cdot e^{-(2\pi f t_o)}], \qquad (4.3.1)$$

and can be done as a separate operation, but is usually incorporated in a filter. The results after time shifting are transformed to the time domain and shown in Figures 4.7 and 4.8.
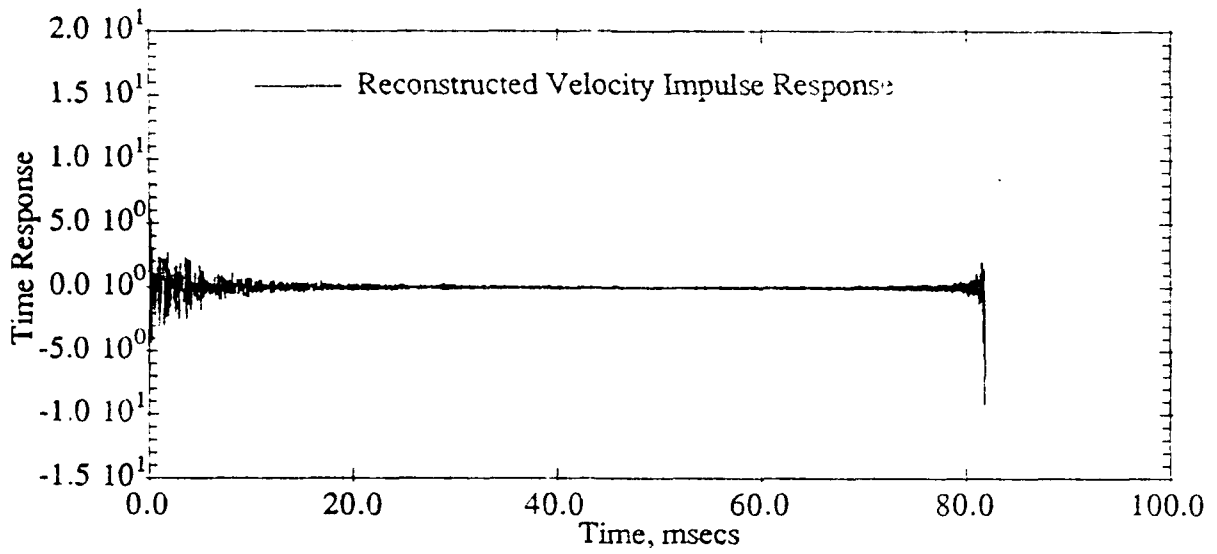
Figure 4.6: Velocity impulse response $h_v(\tau, x_0, x_0)$ without time shifting
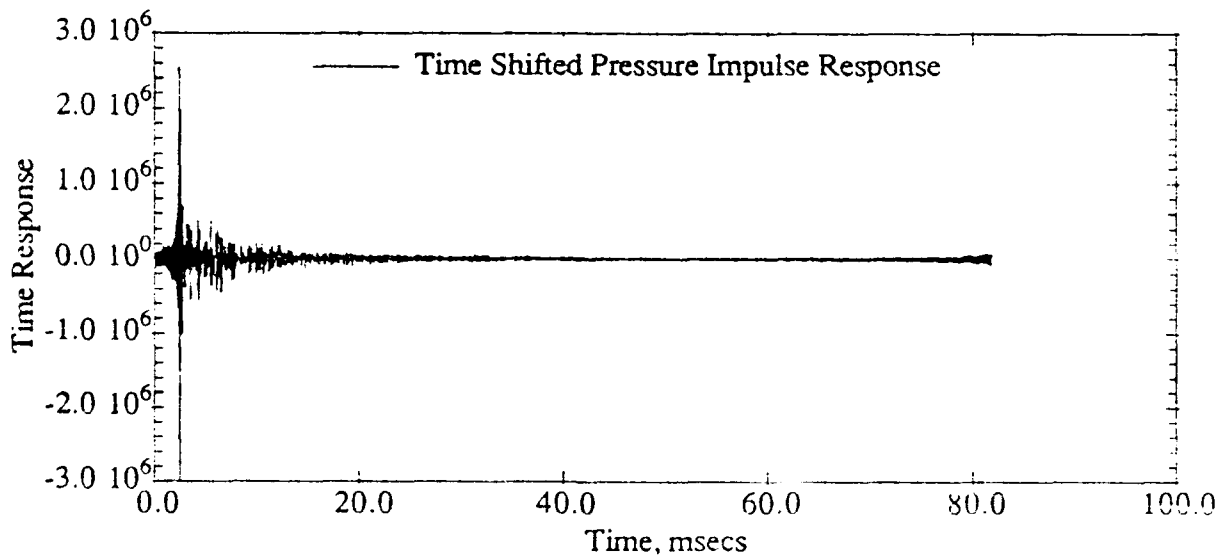
Figure 4.7: Pressure impulse response $h_p(\tau, x_0, x_0)$ time shifted sixty-one time bins
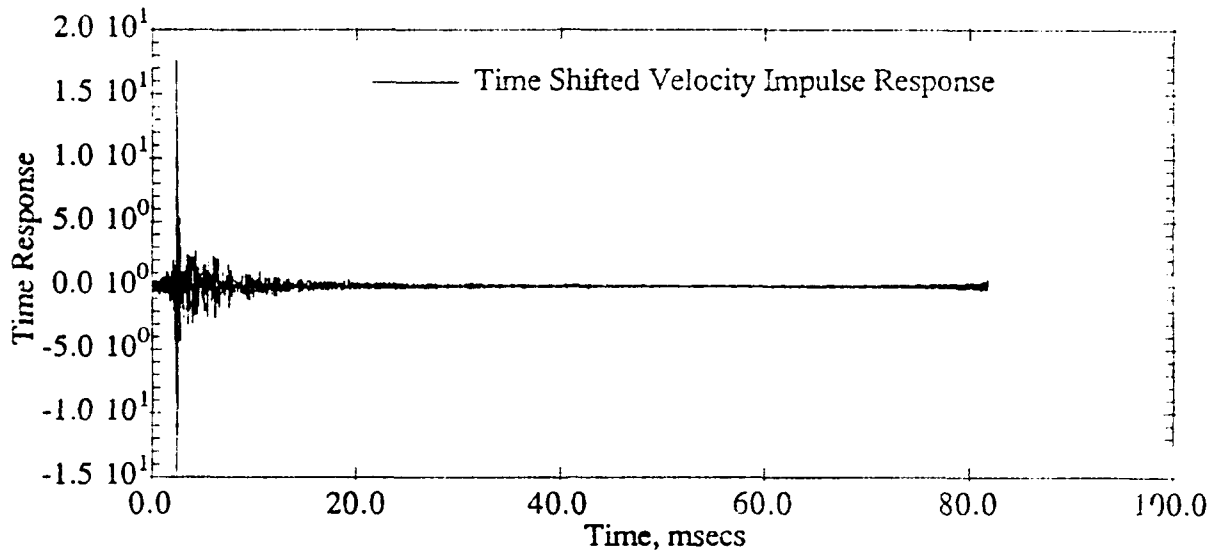
Figure 4.8: Velocity impulse response $h_v(\tau, x_0, x_0)$ time shifted sixty-one time bins

4.4. Importance of Spectral Symmetry

A simple demonstration is probably the most clear way to convey the importance of spectral symmetry that was described in Equation (4.2.1). Figure 4.9 shows the error produced in the pressure impulse response function when its corresponding spectrum is made symmetric about the $N/2$ bin rather than the $N/2 + 1$ bin. This figure shows that moving the alias frequencies by just one point causes error in the pressure impulse response with a maximum magnitude of about three percent of the maximum correct impulse response. This error grows to over ten percent when the second half of the spectra is made symmetric about the $N/2 - 1$, only two frequency bins away from the correct bin. These errors seem large even though an error of one or two bins in the point of symmetry appears to be a minor mistake on the surface, but an inverse FFT views all the alias frequencies in the second half of the spectrum as having incorrect magnitudes.
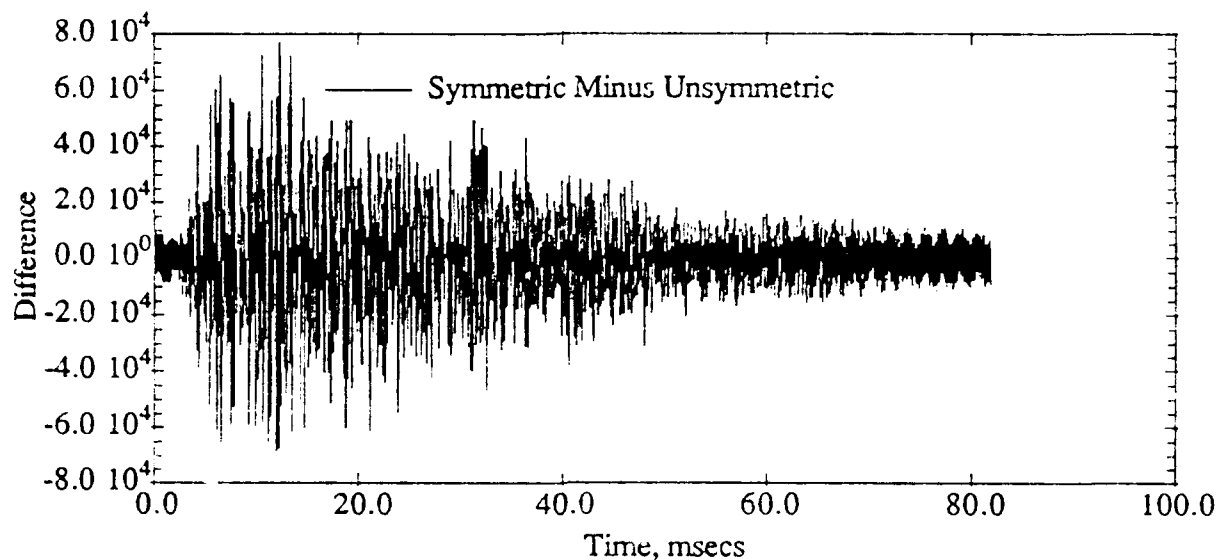
Figure 4.9: Symmetric minus unsymmetric pressure impulse response function.

Figure 4.10 shows that the unsymmetric pressure frequency response actually produces an impulse response with a large imaginary portion when using complex valued FFTs, as opposed to one with zero magnitude, which is produced by a symmetric $H_p(f, x_o, x)$. This imaginary part must be viewed as errant, since only real signals are possible in the time domain. Its maximum amplitude is also roughly 3% of the maximum amplitude of the correct impulse response function.

4.5. Filtering

Another very important step in the FFT implementation of the linear system model is filtering. Filtering multiplies every spectrum in the pressure and velocity transfer functions by a smooth frequency domain function, or filter. The data provided by NRL was filtered by a Kaiser-Bessel filter which had a central frequency of 5 kHz, a bandwidth of 6 kHz and a time shift of 61 bins. This filter was also made symmetric about the Nyquist frequency in the same
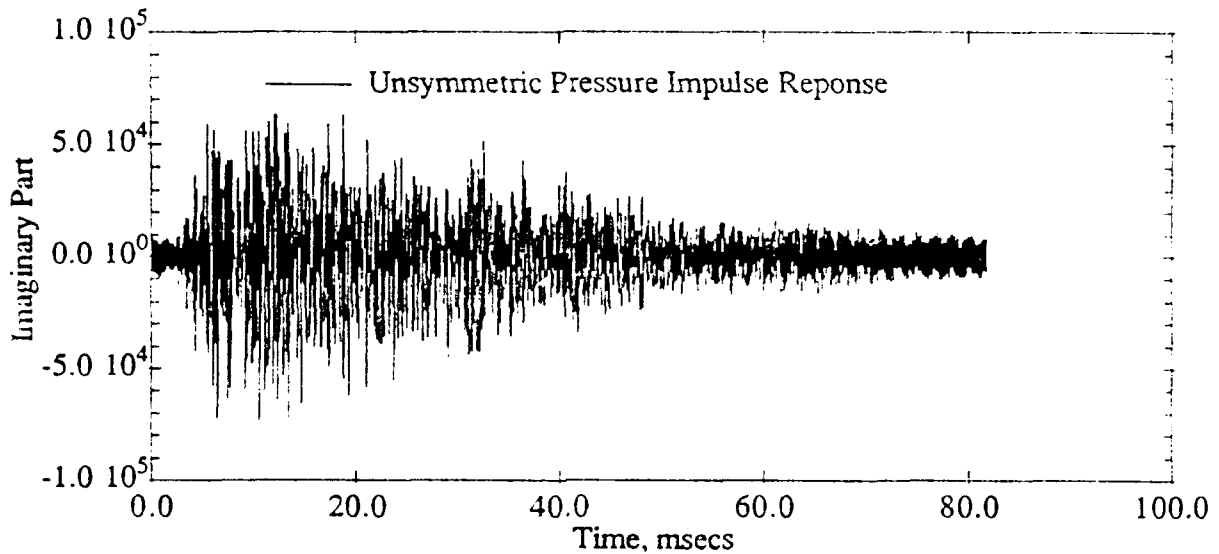
Figure 4.10: Imaginary part of pressure impulse response due to lack of spectral symmetry (should be zero)

way as the data was. The central frequency and the bandwidth correspond to the 2-8 kHz spectra provided in the data. Figure 4.11 shows the filter used in this research.

The need for filtering is twofold. First of all, the filter incorporates the needed time shift previously described. The second, and the most important reason for filtering, is continuity of the data. Figures 4.3 and 4.4 show pressure and velocity spectra for the driver point on the shell. Careful observation of these spectra indicates that they drop suddenly to zero at the edge of the spectra These sharp drops appear as discontinuities to the FFT algorithm. Figure 4.12 shows that the filter removes these discontinuities by multiplying the entire spectrum by a smooth, continuous function, namely the filter. Notice that the edges of $H_p(f, x_0, x)$ shown in Figure 4.12 are brought gradually to zero, and that the outline matches that of the filter shown in Figure 4.11. The same filter was applied to all points of the velocity transfer function as well.

The inverse FFT algorithm relies on this continuity when returning a spectrum to the
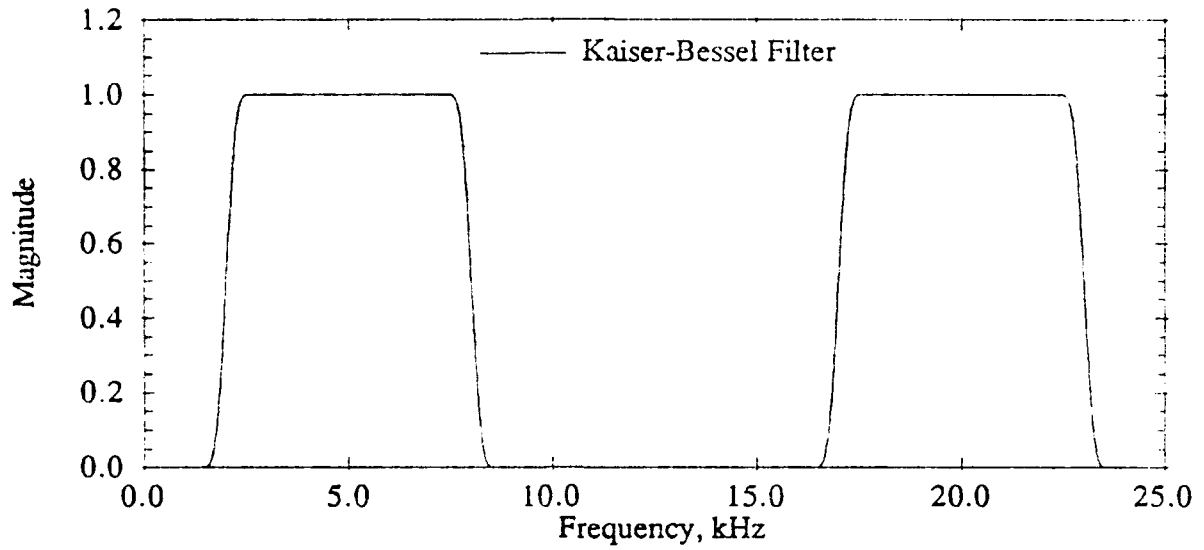
Figure 4.11: Kaiser-Bessel filter with 5 kHz central frequency, 6 kHz bandwidth, 61 bin time shift, and symmetric about the Nyquist frequency
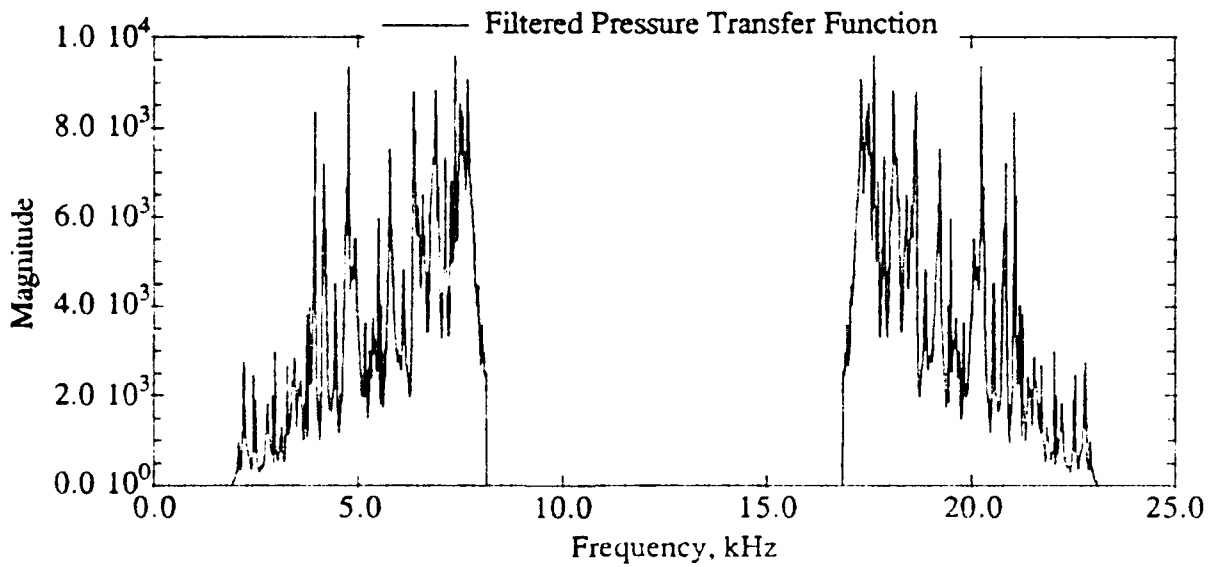
Figure 4.12: Filtered pressure transfer function $H_p(f, x_o, x)$ for the driver point, x_o

time domain (Bracewell 8-11). Combined with this assumption is the fact that the FFT uses a linear combination of each bin in the frequency spectrum to produce a time domain description. The result is that, depending on the size of the edge discontinuity compared to the rest of the data, percent errors ranging from small to very large can be produced. Figure 4.13 shows the filtered minus the unfiltered pressure impulse response for the driving point of the shell. Note that the maximum magnitude of the difference is about 10% of the maximum amplitude of the filtered pressure impulse response shown in Figure 4.12.
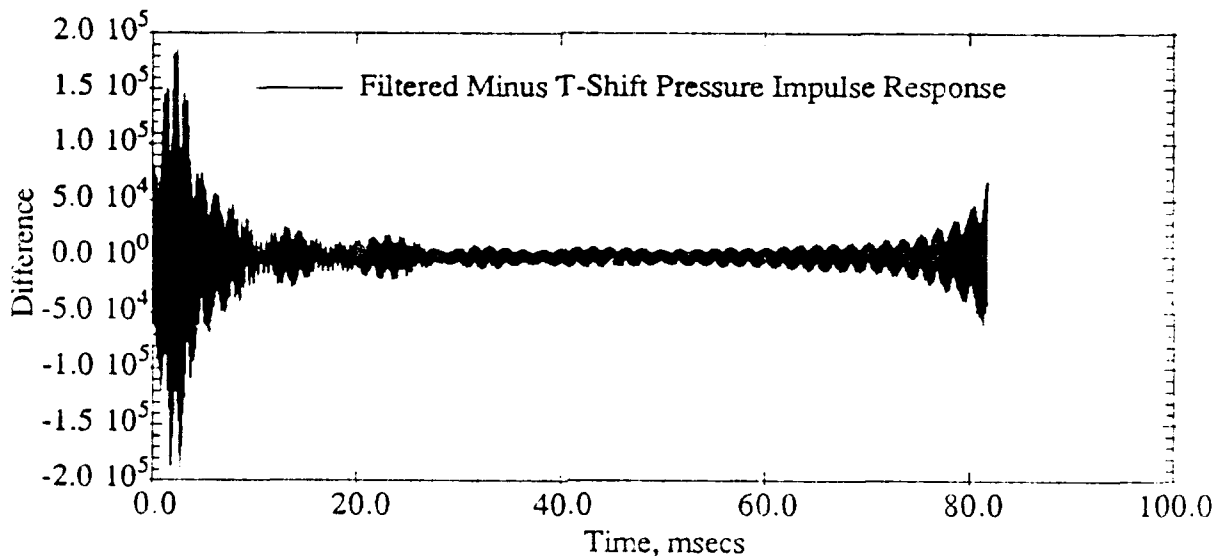
Figure 4.13: Filtered minus time shifted pressure impulse response for the driver point

Comparison of Figure 4.14 and Figure 4.7 shows that the filtered pressure impulse response has a more clearly defined starting point than the time shifted only counterpart. Most of the difference in Figure 4.13 is a result of this feature.

4.6. Considerations for Zeropadding

The way in which the convolution integral. Equation (2.1.1), is implemented with FFTs requires zeropadding. Zeropadding is the process by which a signal in the time domain
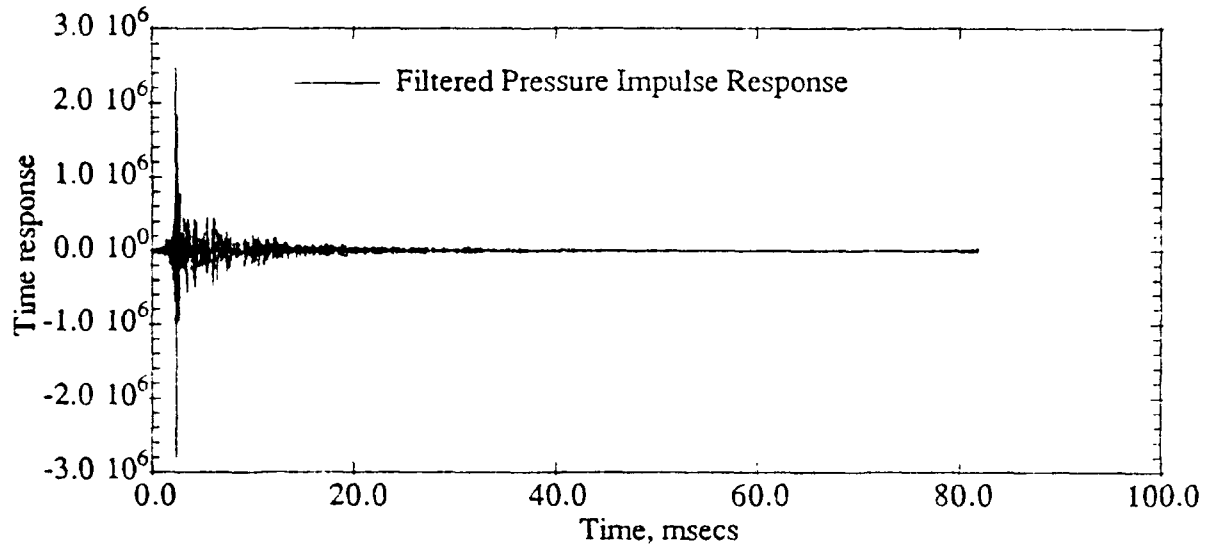
Figure 4.14: Filtered pressure impulse response for the driver point of the shell

is made longer than its original length by placing zeros on the end of the signal. For this research, both transfer function data at each point x in the holograms and the synthetic forces were transformed to the time domain after the proper reconstruction and filtering was performed. Then the signals were made twice as long by placing zeros in bins 2049 through 4096. Finally, both the transfer functions and the synthetic forces were transformed back to the frequency domain for use in Equations (2.1.7) and (2.1.8).

Two main types of computer algorithms exist for the purpose of carrying out the convolution integral shown in Equation (2.1.1) for discrete, finite data and force arrays. The first is the linear, or sometimes referred to as the picket fence algorithm. The second type is the circular convolution algorithm which, due to the nature of the FFT algorithm, is the type of convolution actually performed when pressure and velocity are calculated in the frequency domain via Equations (2.1.7) and (2.1.8).

Suppose we have a discrete force array and a pressure transfer function array for a

given point x, both containing only four data points in the time domain for the purpose of easy illustration. Presume further that these arrays have values f_1, f_2, f_3, f_4 and h_{p1}, h_{p2}, h_{p3}, h_{p4}, respectively. Then the pressure array, p_1, p_2, p_3, p_4, resulting from the picket fence convolution algorithm is given by Equations (4.6.1) to (4.6.5)

$$p_1 = f_1 \cdot h_{p1},$$ (4.6.1)

$$p_2 = f_1 \cdot h_{p2} + f_2 \cdot h_{p1},$$ (4.6.2)

$$p_3 = f_1 \cdot h_{p3} + f_2 \cdot h_{p2} + f_3 \cdot h_{p1},$$ (4.6.3)

$$p_4 = f_1 \cdot h_{p4} + f_2 \cdot h_{p3} + f_3 \cdot h_{p2} + f_4 \cdot h_{p1},$$ (4.6.4)

or

$$p_i = \sum_{n=1}^{i} f_n \cdot h_{p(i-n+1)} \qquad i = 1 \text{ to } N.$$ (4.6.5)

The resulting pressure array is also shown in Figure 4.15 for $f_1 = 2$, $f_2 = 1$, $f_3 = 3$, $f_4 = 2$, and $h_{p1} = 1$, $h_{p2} = 2$, $h_{p3} = 1$, $h_{p4} = 1$, where * denotes convolution and $N = 4$ for Equation (4.6.5). Resulting pressure array values are $p_1 = 2$, $p_2 = 5$, $p_3 = 7$, $p_4 = 11$, which are considered to be the correct pressure values for this force and pressure impulse response in the time domain (Bracewell 24-48).

If the same force and pressure impulse response function are convolved via the circular convolution integral in their present form, the resulting pressure is quite different, and incorrect. This is because the circular convolution presumes that the arrays are arranged in a circular fashion, and uses all points in both the force and pressure impulse response arrays. Equations (4.6.6) to (4.6.9),

$$p_1 = f_1 \cdot h_{p1} + f_2 \cdot h_{p4} + f_3 \cdot h_{p3} + f_4 \cdot h_{p2}.$$ (4.6.6)

synthetic force   impulse response   resultant pressure
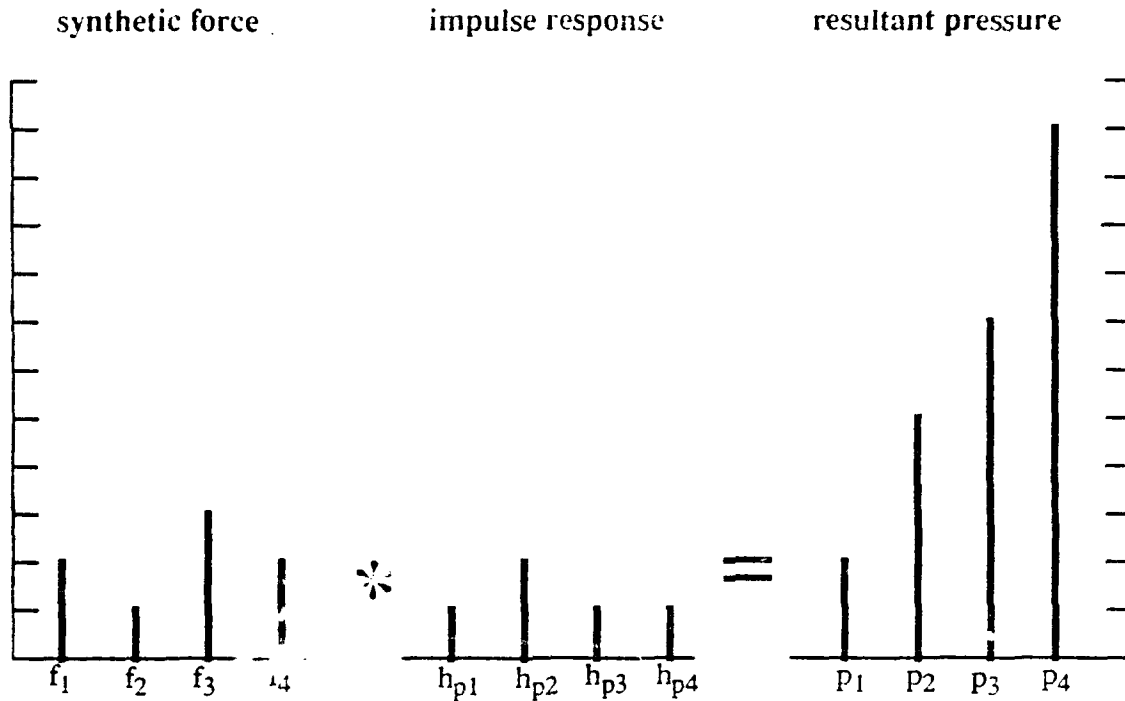
Figure 4.15. Pictorial diagram of the picket fence convolution algorithm for $N = 4$

$$p_2 = f_1 \cdot h_{p2} + f_2 \cdot h_{p1} + f_3 \cdot h_{p4} + f_4 \cdot h_{p3} \; , \hspace{2cm} (4.6.7)$$

$$p_3 = f_1 \cdot h_{p3} + f_2 \cdot h_{p2} + f_3 \cdot h_{p1} + f_4 \cdot h_{p4} \; , \hspace{2cm} (4.6.8)$$

$$p_4 = f_1 \cdot h_{p4} + f_2 \cdot h_{p3} + f_3 \cdot h_{p2} + f_4 \cdot h_{p1} \; , \hspace{2cm} (4.6.9)$$

demonstrate this fact for $N = 4$. This idea is shown pictorially in Figure 4.16. The new result is $p_1 = 10$, $p_2 = 10$, $p_3 = 9$, $p_4 = 11$. To better understand circular convolution, imagine the transfer function circle being placed upside down on top of the force circle with f_1 and h_{p1} aligned. Equation (4.2.6) then multiplies all aligned quantities and sums the products to obtain the first pressure value. Then the upside down pressure transfer function circle is rotated one position counter clockwise and the process is repeated. In this case, four iterations of this

process were performed to obtain the pressure result shown in Figure 4.16. If, however, the forcing function and the pressure transfer function are zeropadded, the correct result can be obtained as shown in Equations (4.6.10) to (4.6.13)

$$p_1 = f_1 \cdot h_{p1} + f_2 \cdot h_{p8} + f_3 \cdot h_{p7} + f_4 \cdot h_{p6} + f_5 \cdot h_{p5} + f_6 \cdot h_{p4} + f_7 \cdot h_{p3} + f_8 \cdot h_{p2}, \quad (4.6.10)$$

$$p_2 = f_1 \cdot h_{p2} + f_2 \cdot h_{p1} + f_3 \cdot h_{p8} + f_4 \cdot h_{p7} + f_5 \cdot h_{p6} + f_6 \cdot h_{p5} + f_7 \cdot h_{p4} + f_8 \cdot h_{p3}, \quad (4.6.11)$$

$$p_3 = f_1 \cdot h_{p3} + f_2 \cdot h_{p2} + f_3 \cdot h_{p1} + f_4 \cdot h_{p8} + f_5 \cdot h_{p7} + f_6 \cdot h_{p6} + f_7 \cdot h_{p5} + f_8 \cdot h_{p4}, \quad (4.6.12)$$

$$p_4 = f_1 \cdot h_{p4} + f_2 \cdot h_{p3} + f_3 \cdot h_{p2} + f_4 \cdot h_{p1} + f_5 \cdot h_{p8} + f_6 \cdot h_{p7} + f_7 \cdot h_{p6} + f_8 \cdot h_{p5}. \quad (4.6.13)$$
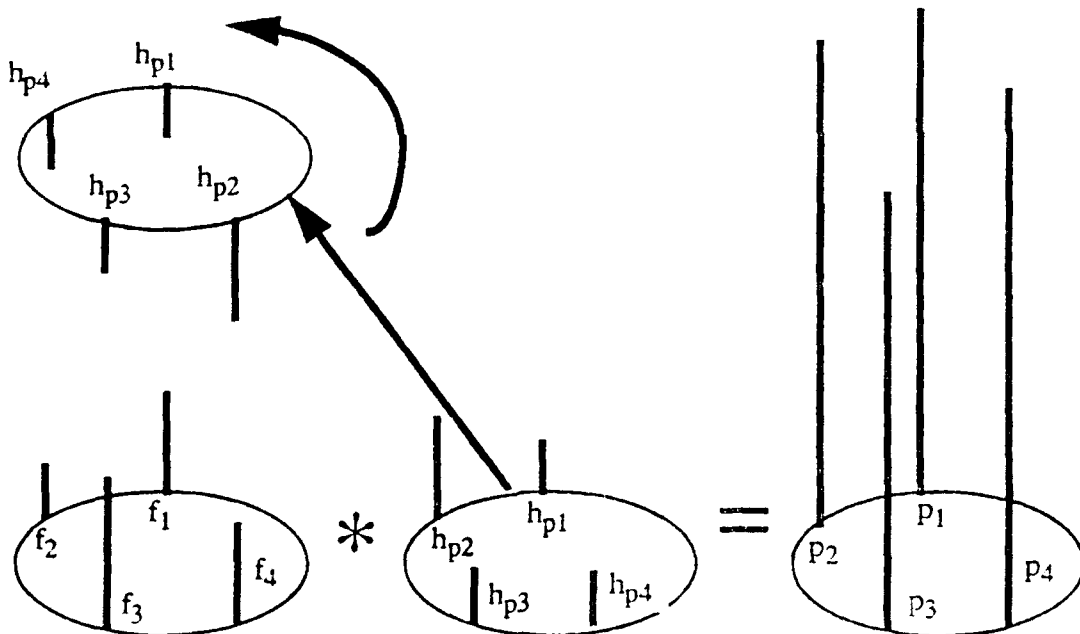
Figure 4.16: Pictorial representation of the circular convolution algorithm for N = 4

Since f_5 through f_8 and h_{p5} through h_{p8} are zero because they were extra zeros added on for the purpose of zeropadding, Equations (4.6.10) to (4.6.13) reduce to be exactly the same as

Equations (4.6.1) to (4.6.4), respectively. This means that zeropadded arrays convolved via circular convolution give the same result as non-zeropadded arrays convolved via picket fence type convolution. Thus, the circular convolution can only be done correctly if the two arrays to be convolved are zeropadded to at least twice their original length. Because circular time domain convolution is the type represented by the multiplication in frequency domain of Equations (2.1.7) and (2.1.8), all data and forces were inverse Fourier transformed to time, zeropadded, and returned to frequency for further processing.

CHAPTER 5

DESCRIPTION OF FORCES

5.1. Measured Force

In the initial measurement, only the time signal of the driving force, $f_0(t, x_o)$ was known. This measurement force was a chirp, consisting of a sine wave swept uniformly from 2000 Hz to 8000 Hz. The force time duration was only about 25% of the total acquisition time, so the measurement contained a build up and decay of the fluid loaded cylinder's acoustic radiation as well as its structural vibration. An FFT was performed to obtain $F_0(f, x_o)$ for calculation of the pressure transfer function via the deconvolution process already described.

5.2. Synthetic Forces

A Gaussian windowed cosine function was chosen as the synthetic force input to simulate shell sound radiation. This force was chosen due to ease of computation and control of time duration and frequency bandwidth. The Gaussian force consists of a single frequency cosine wave windowed by a Gaussian exponential function. For a force consisting of a single Gaussian pulse, the analytic expressions in the time and frequency domains are shown in Equations (5.2.1) and (5.2.2),

$$f_{syn}(t, x_o) = \cos[2\pi f_o(t - t_o)]\, e^{-\pi\{(t-t_o)/\tau\}^2}, \tag{5.2.1}$$

and

$$F_{syn}(f, x_o) = (\tau/2)\, e^{2\pi jft_o}\, e^{-\pi\{(f-f_o)\tau\}^2} + e^{-\pi\{(f+f_o)\tau\}^2}. \tag{5.2.2}$$

The frequency of the cosine portion, also referred to as the central frequency (in Hz), is represented by f_o. The quantity t_o is a time delay at which the pulse is centered, τ is a constant that is related to the time duration of a single pulse, and $j = \sqrt{-1}$. Examples of the Gaussian
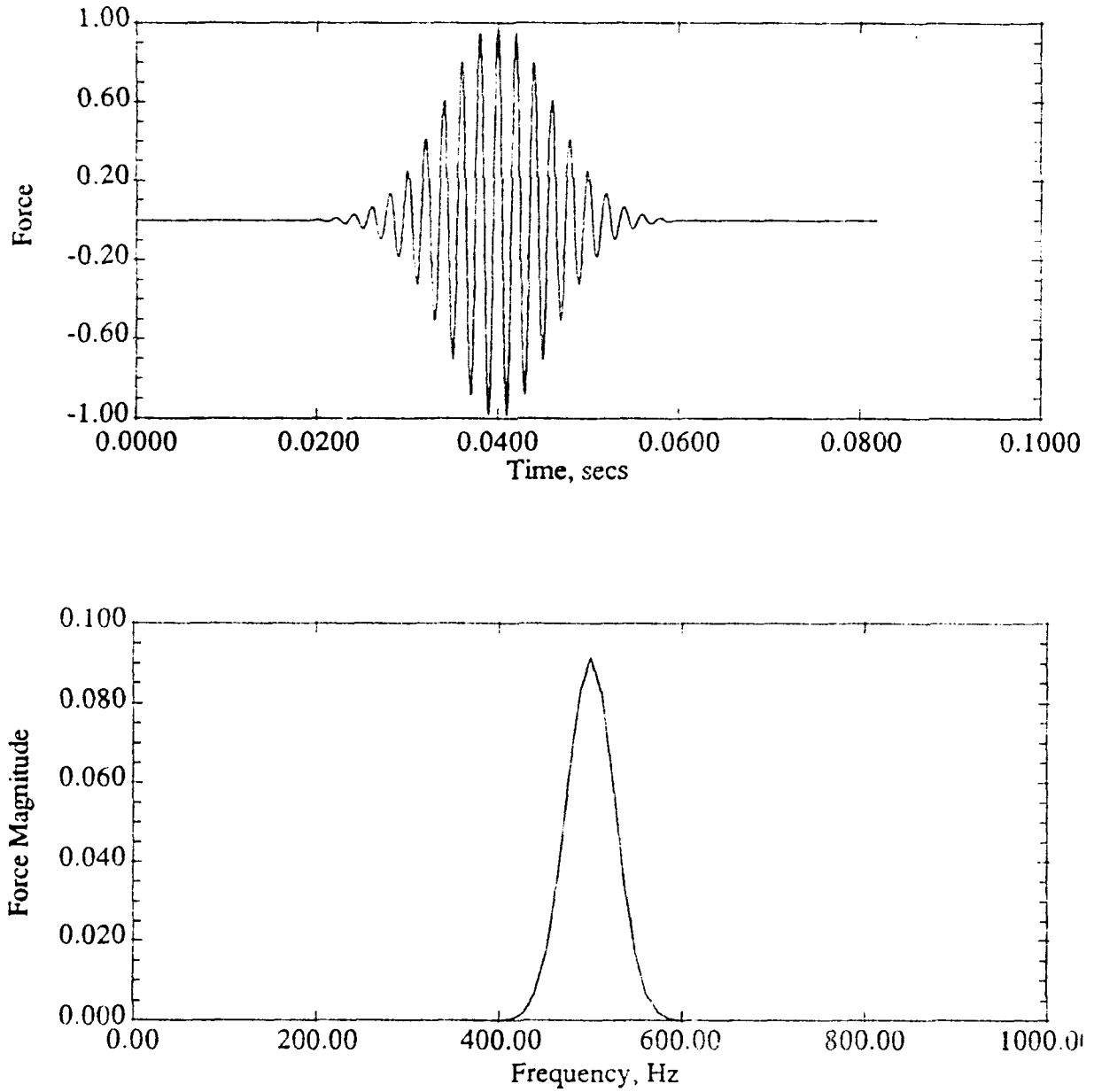
Figure 5.1: Example of the Gaussian window force with $f_o = 500$ Hz, $\tau = 0.0125$, and $t_o = 0.04$s a) in the time domain (top), and b) in the frequency domain (bottom)

force in time and frequency domains for a central frequency of 500 Hz are shown in Figure 5.1. For simplicity, the force has an amplitude of one unit in the time domain, although the function could be scaled to any amplitude. Also, units are not important, since results of forces are compared to one another. Only the relative change produced by forces is of interest, not the value of individual results. In Figure 5.1b, only the first half of the spectrum required for the FFTs is shown. All forces used for simulation of sound radiation were made symmetric about the Nyquist cutoff frequency in the manner described in sections 4.2 and 4.4.

Gabor (434) relates the force time duration and frequency bandwidth to the constant τ via the uncertainty relations

$$\Delta t = \tau \sqrt{\pi/2}, \tag{5.2.3}$$

and

$$\Delta f = (1/\tau)\sqrt{1/(2\pi)}, \tag{5.2.4}$$

where Δt is the force time duration and Δf is the frequency bandwidth. Note that as τ (tau) is
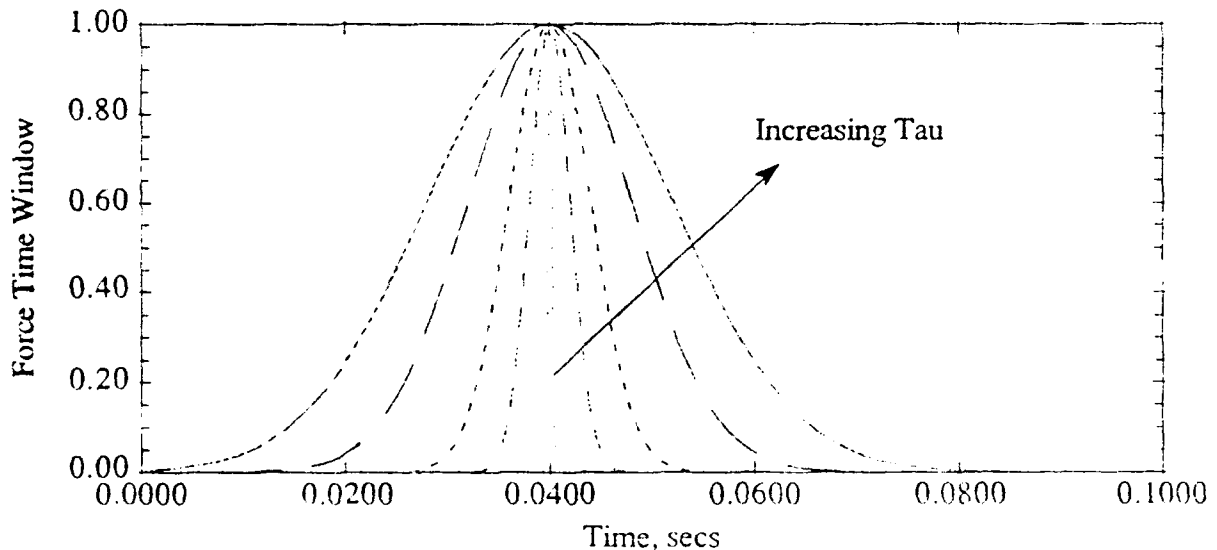
Figure 5.2: Gaussian force time window duration increases with tau
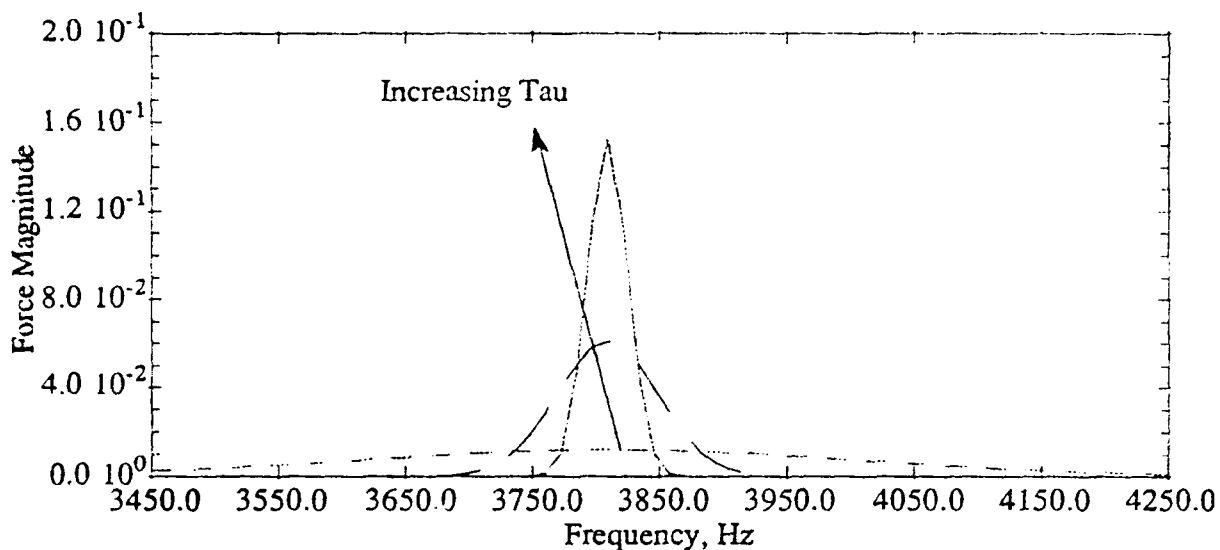
Figure 5.3: Gaussian force frequency bandwidth decreases with increasing tau

increased the frequency bandwidth decreases while the force time duration increases. This fact is pertinent in section 7.1 of the results. Figures 5.2 and 5.3 demonstrate this relationship.

Finally, the Gaussian force is easily modified to include multiple pulse forces

$$f_{syn}(t, x_o) = \sum_{i=1}^{N} \cos\left[2\pi f_o (t - t_o - (i-1)s)\right] e^{-\pi[(t - t_o)/\tau]^2}, \qquad (5.2.5)$$

and

$$F_{syn}(f, x_o) = \sum_{i=1}^{N} (\tau/2) e^{2\pi j f[t_o + (i-1)s]} \left[e^{-\pi\{(f - f_o)\tau\}^2} + e^{-\pi\{(f + f_o)\tau\}^2} \right], \qquad (5.2.6)$$

where all parameters are the same as before, and s represents the space between successive force pulses in seconds. The total number of pulses, N, is limited by the total sample time and the time duration of each pulse. Pulses may be spaced from zero seconds apart to as much as will fit in the total sample time. In this research, all forces used in simulating acoustic radiation were designed to be contained entirely within the original sample time of 83

milliseconds (2048 times 40 microseconds). Only multiple pulse forces with uniform time duration between pulses are calculated in the equations above. The equations could be easily modified to include non-uniform spacing by removing the summation symbol and including a different variable, such as t_1, t_2, etc., for each successive pulse. Also note that the force has analytical descriptions in both the time and frequency domain. Either may be used to calculate the desired force, and then the force can be transformed to time or frequency by FFTs with negligible error. However, it is recommended that a force be created in the frequency domain for use in sound simulation via Equations (2.1.7) and (2.1.8) in the time domain to make sure it decays within the 83 milliseconds of the original time sample. Further, only a version of the time domain force provided by Gabor was used in this thesis. The frequency domain description was derived from the time domain description using Fourier transform techniques (Bracewell 98-120). This section concludes with examples of single and multiple pulse forces shown in the time domain for two different pulse spacings by Figures 5.4 and 5.5.
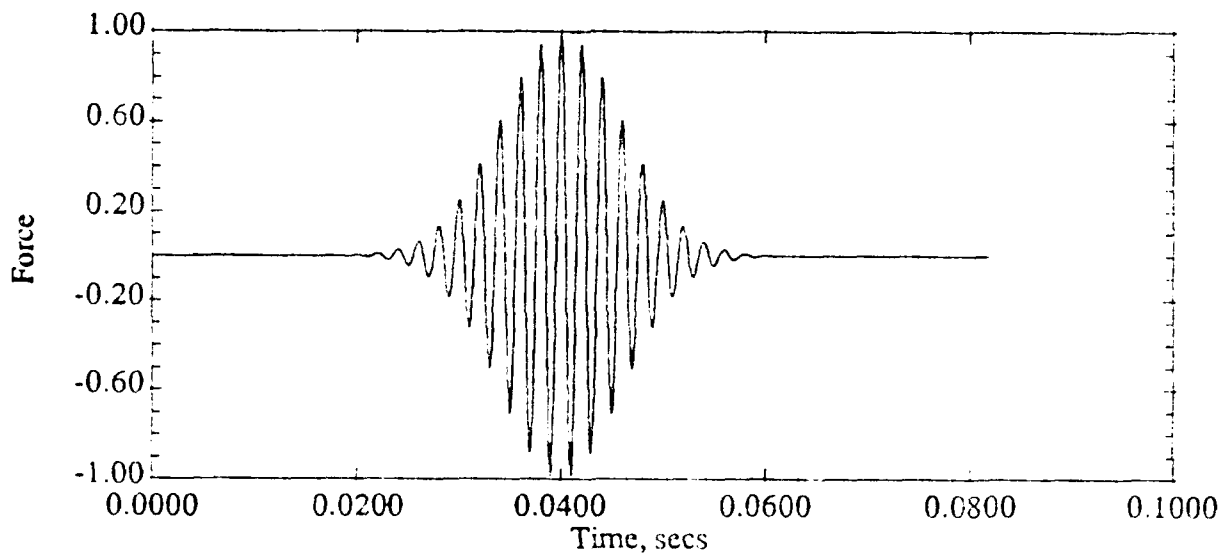
Figure 5.4: A multiple pulse Gaussian time force with zero seconds between pulses; $f_0 = 500$ Hz, s = 0.0 seconds. $\tau = 0.01$, and $t_0 = 0.02$ seconds
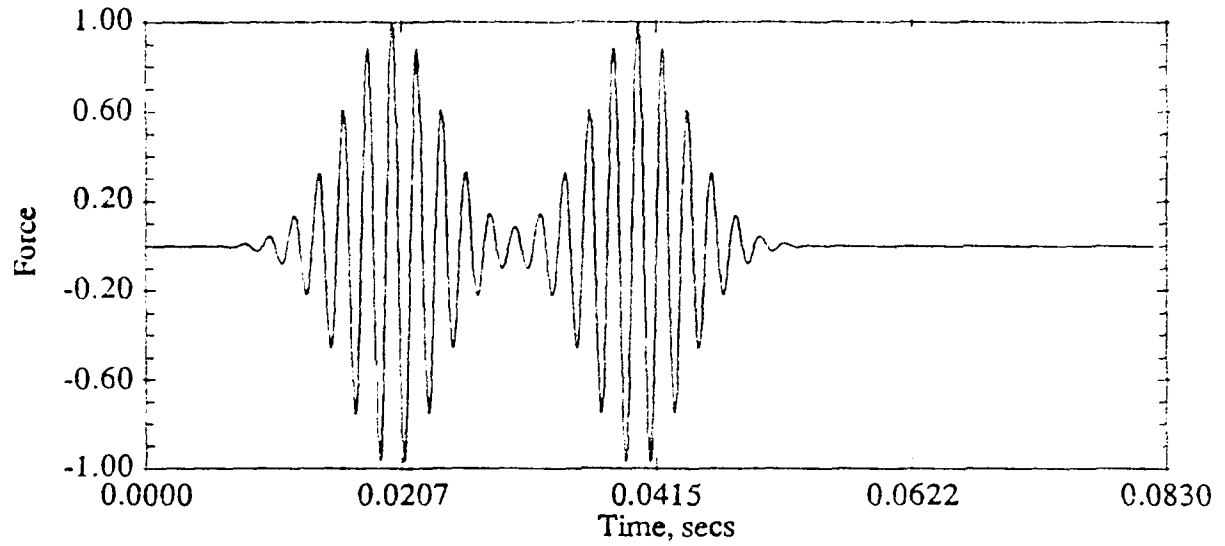
Figure 5.5: A multiple pulse Gaussian time force with 0.02 seconds between pulses; $f_o = 500$ Hz, s = 0.02 seconds, $\tau = 0.01$, and $t_o = 0.02$ seconds

CHAPTER 6

CALCULATED QUANTITIES

6.1. Overview

Applying a synthetic force to the entire shell produces enormous amounts of acoustic data. For each applied force there are 64 axial and 64 circumferential spatial locations which have 2048 time steps for both the acoustic pressure and the normal acoustic velocity. One possible means of viewing so much data is animation. Another method could be to view a series of snapshots of the data in time. Neither of these methods, however, are adequate for presentation in a thesis. Thus, total energy radiated by the shell was the means chosen to best show all of the data for the entire shell. Calculation of this quantity and some other quantities useful in explaining the results will be discussed in this chapter.

6.2. Normalized Energy

Total energy of the shell proved to be a very valuable means to analyze the results for the entire shell. To more fully understand this quantity, it is helpful to look at a fundamental power balance for the situation as presented by Mann et. al. (1661). The total change in energy of a given volume V can be represented by an integral of the instantaneous intensity over any surface S enclosing the volume, which is stated in integral form as

$$\frac{\partial}{\partial t}\iiint_V [E(t,x)_{kin} + E(t,x)_{pot}]\,dV = -\iint_S I_i(t,x)\,dS , \qquad (6.2.1)$$

where $E(t,x)_{kin}$ is the kinetic energy, $E(t,x)_{pot}$ is the potential energy, and $I_i(t,x)$ is the instantaneous acoustic intensity normal to the surface S where S is the surface enclosing the volume V. Thus, calculating the right hand side of Equation (6.2.1) provides the total energy leaving the shell at an instant. S is designated as the hologram surface where the acoustic pressure and normal acoustic velocity transfer functions exist.

Because all synthetic forces are now applied at the same point, the x_0 dependence is

removed from the notation in further equations. Then the instantaneous acoustic intensity normal to the shell is provided by

$$I_i(t, \phi, z) = p(t, \phi, z) \cdot v(t, \phi, z), \qquad (6.2.2)$$

where $p(t, \phi, z)$ is the acoustic pressure given by Equation (2.1.7), and $v(t, \phi, z)$ is the normal acoustic velocity given by Equation (2.1.8), with the dependence on x_0 dropped from the notation. The general field point x in Eqns. (2.1.7) and (2.1.8) is now given by the coordinates ϕ and z to denote circumferential and axial dependence, respectively.

Second, an intermediate quantity called instantaneous acoustic power, denoted $\Pi_i(t)$, is calculated for the whole shell by

$$\Pi_i(t) = \int_{z_1=0}^{z_2=L} \int_{\phi_1=0}^{\phi_2=2\pi} I_i(t, \phi, z) d\phi dz, \qquad (6.2.3)$$

where the limits $z_1 = 0$ and $z_2 = L$ represent the entire 64 axial points in the pressure and velocity holograms, and the limits $\phi_1 = 0$ and $\phi_2 = 2\pi$ represent the entire 64 circumferential points in the holograms. It is useful to note that the instantaneous power can be calculated for any z_1, z_2, ϕ_1, and ϕ_2 within the 64 by 64 point measurement hologram. This fact will be utilized in the results section. An example of the instantaneous power for the entire shell is given in Figure 6.1 a for a one pulse Gaussian synthetic force. The most important feature of this plot is that power is alternately positive and negative. The positive values signify that the shell is radiating energy into the fluid and negative values signify that the shell is absorbing energy form the fluid. Thus, sound is being radiated by the shell to the fluid and being reabsorbed by the shell from the fluid

Third, the total energy leaving the shell via sound radiation is obtained by

$$E(t) = \int_0^t \Pi_i(\tau) d\tau, \qquad (6.2.4)$$

where $E(t)$ represents the total energy which has been transferred from the shell to the fluid up
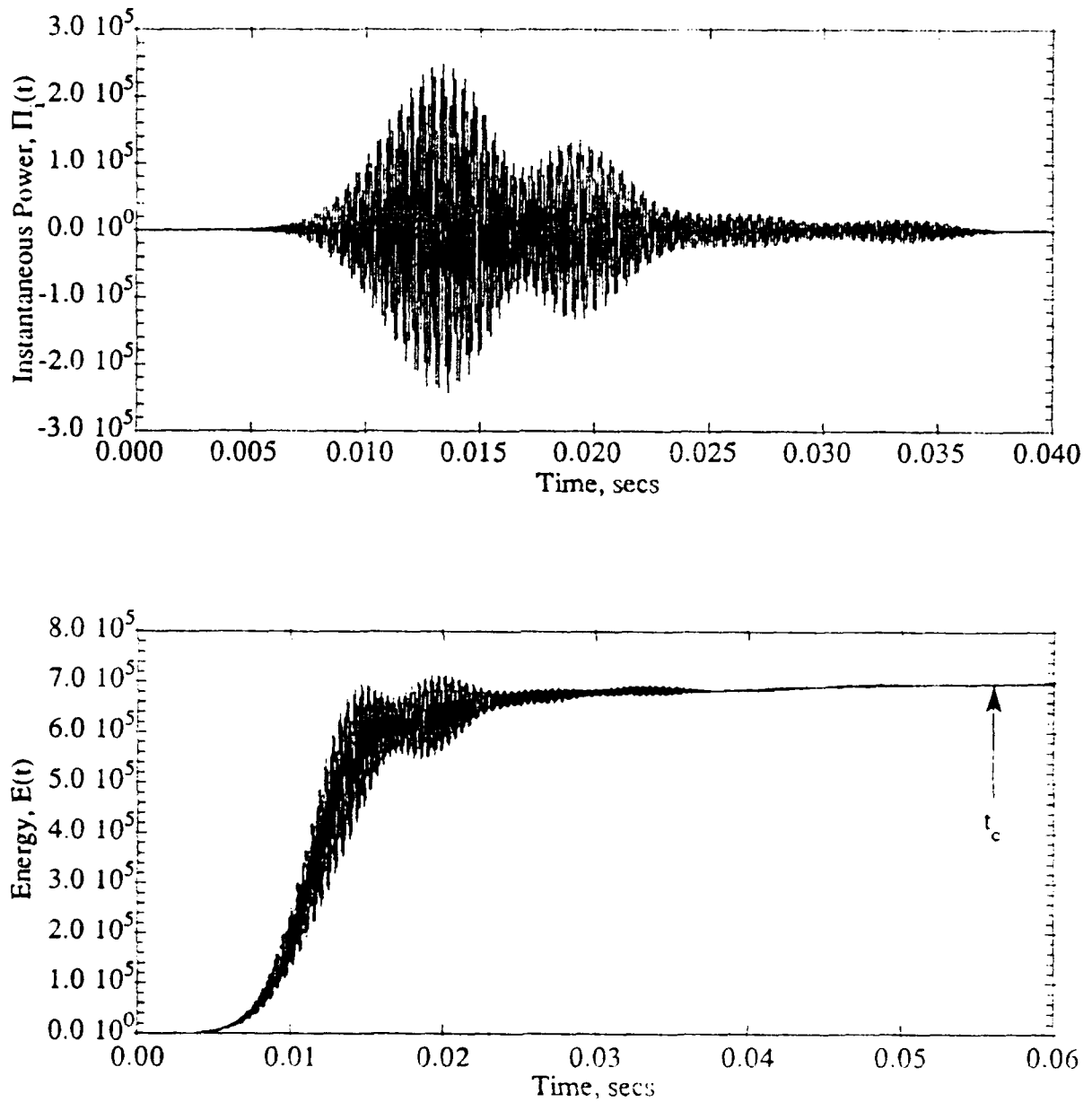
Figure 6.1: Instantaneous power and total energy radiated for the entire shell produced by a single pulse Gaussian force with $f_0 = 3808.6$ Hz, $\tau = 0.01$, and $t_0 = 0.01$ seconds

to this time. An example of total radiated energy for the entire shell is shown in Figure 6.1b. Note that total energy fluctuates and then finally converges at t_c. Thus, $E(t_c)$ represents the total energy radiated by the shell for this particular pulse. A second example of total radiated energy is shown in Figure 6.2, but in this instance $E(t_c)$ is never reached because the radiated energy does not converge within 83 milliseconds. Only energies that converge at a distinct t_c, as pointed out in Figure 6.1b are reported in this research. It is important to notice that the quantities calculated in Equations (4.2.2) to (4.2.4) could have been calculated in the frequency domain as well, but then the existence of t_c could not be observed.
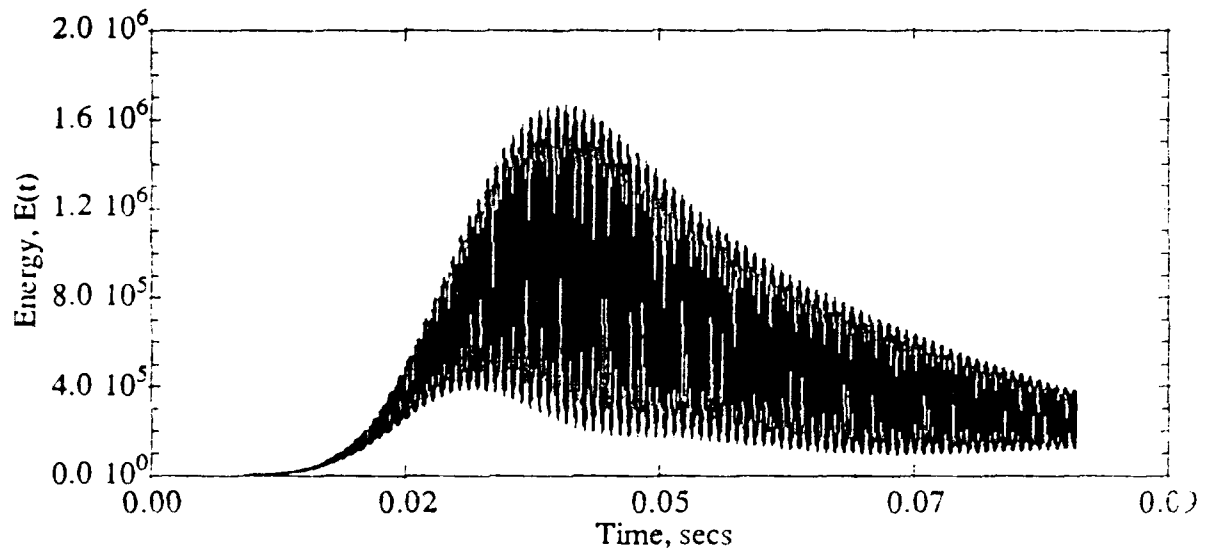
Figure 6.2: Total energy radiated by the entire shell when driven by a one pulse Gaussian force with $f_o = 2966.3$ Hz, $\tau = 0.02$, and $t_o = 0.04$ seconds

The fourth step in computing normalized energy is performed. Namely, the total mechanical energy input by the synthetic driving force is computed by

$$E_{in} = \left\{ \int_0^T [f(t, \phi_o, z_o) \cdot v(t, \phi_o, z_o)] \, dt \right\} \cdot dA, \qquad (6.2.5)$$

where E_{in} is the total input mechanical energy, and $f(t, \phi_0, z_0)$ is the force at the driver point. The resulting shell velocity at the driver point is given by $v(t, \phi_0, z_0)$, which, from the boundary condititions, must be equal to the normal acoustic velocity. Finally, dA represents the differential area of the driver point.

Finally, the normalized energy radiated by the shell is the quotient

$$E_N = \frac{E(t_c)}{E_{in}},$$

(6.2.6)

where E_N is the fraction of the total energy input by the driving force that is radiated as sound. The need to compute this quantity is clearly seen by comparing an example of the results that is not normalized with an example of the input mechanical energy . Figures 6.3 and 6.4 show
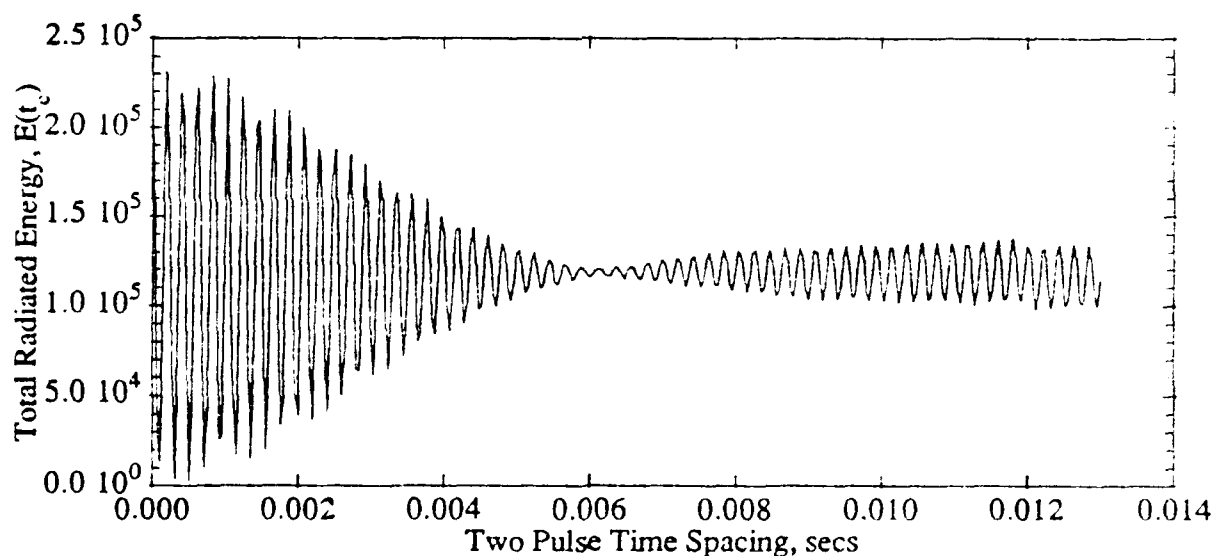
Figure 6.3: Total energy, $E(t_c)$, radiated vs.two pulse force time separation for the entire shell resulting from driving forces with $f_0 = 4785.2$ Hz, $t_0 = 0.0125$ seconds, and $\tau = 0.005$ seconds

such examples. Note that while the total energy radiated, $E(t_c)$, varies as a function of the time separation of two pulses, so does the input mechanical energy. Thus, it is not possible to determine if an increase in radiated energy occurred because of the interaction between pulses
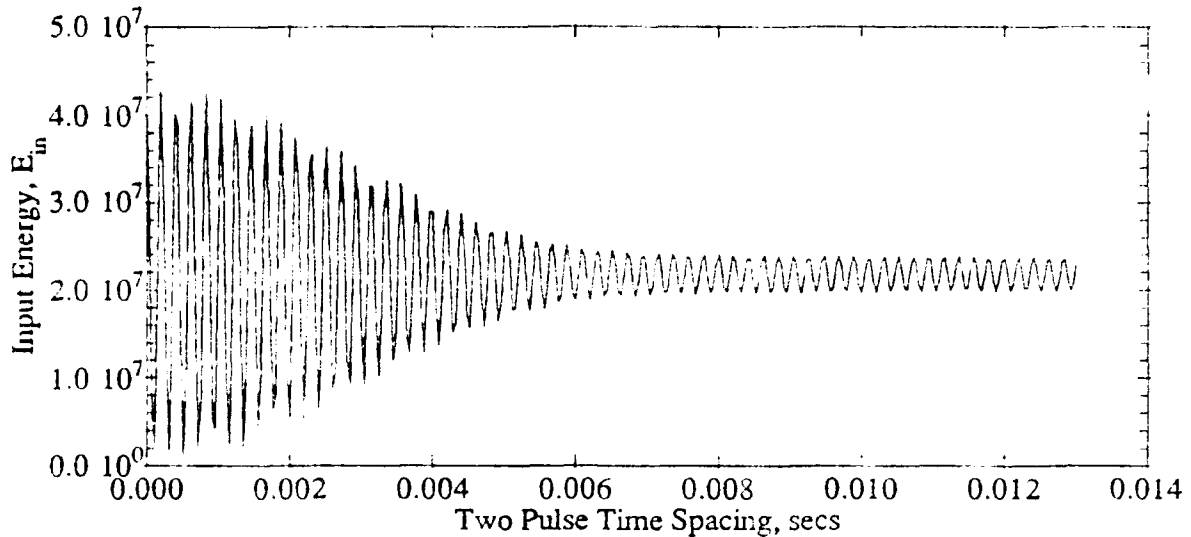
Figure 6.4: Input mechanical energy, E_{in}, vs.two pulse force time separation resulting from driving forces with $f_0 = 4785.2$ Hz, $t_0 = 0.0125$ seconds, and $\tau = 0.005$ seconds

or because of a change in the amount of input mechanical energy. Thus, normalized energy is more significant than simply reporting the radiated energy $E(t_c)$ because it incorporates the amount of energy input to the system as well as the amount radiated. A larger value of $E(t_c)$ means only that more sound was radiated, while a larger value of E_N means that, for a given amount of input energy, a greater percentage of that energy was radiated by the shell as sound.

6.3. Acoustic Intensity

Another quantity of interest that is used to help explain some of the results presented in this thesis is active acoustic intensity. This quantity represents the time integral of the instantaneous acoustic intensity normal to the shell boundary, in Equation (6.2.2). However, the active acoustic intensity is calculated in the frequency domain via

$$I(\phi, z) = \int_0^{2f_c} \frac{1}{2} Re \{ [F_{syn}(f)H_p(f, \phi, z)] \cdot [F^*_{syn}(f)H_v^*(f, \phi, z)] \} \, df, \qquad (6.3.1)$$

where $F_{syn}(f)$ is the synthetic forcing function at the driver as a function of frequency, Re

denotes the real part of the complex frequency domain product, $H_p(f, \phi, z)$ is the pressure transfer function, and $H_v(f, \phi, z)$ is the normal velocity transfer function.

6.4. Impulsive Acoustic Power

The final quantity that is used to explain results, is the impulsive acoustic power. Impulsive acoustic power is defined in this research as

$$\Pi_{imp}(f) = \int\limits_{z_1\phi_1}^{z_2\phi_2} \frac{1}{2} \text{Re}\,\{H_p(f, \phi, z) \cdot H_v^*(f, \phi, z)\}\, d\phi dz, \qquad (6.4.1)$$

a function of frequency. Impulsive acoustic power is best thought of as the time average at each frequency of the energy per unit area radiated by a purely impulsive force. A purely impulsive force has an amplitude of unity for every frequency. Impulsive acoustic power, Π_{imp}, similar to instantaneous power, can be computed for any z_1, z_2, ϕ_1, and ϕ_2 of the hologram surface data provided by NRL. This represents the sound power radiated from a particular area of the shell for an impulsive force. A major difference, however, is that impulsive acoustic power is a function of frequency, while instantaneous power is a function of time.

Total energy radiated by the entire shell up to 83 milliseconds (the total sample time) when excited by a force $F(f)$ is related to the impulsive acoustic power by

$$E_{tot} = \int\limits_{-\infty}^{\infty} [F(f) \cdot F^*(f)] \cdot \Pi_{imp}(f) df, \qquad (6.4.2)$$

if the limits in Equation (6.4.1) include the entire surface area of the shell. Actually, the integration limits used in this research were 0 kHz and 25 kHz because of the sampling time and other parameters discussed in Chapter 4. Recall that when the total energy radiated by the shell converges, Equation (6.2.4) yields $E(t_c)$.

Impulsive power was computed for four areas of the shell. The first area was the entire shell, which was approximated as an integration over all 64 axial and 64 circumferential

points. The second area was a small sector around the driver point corresponding to integration from axial points 24 to point 26 and circumferential points 32 to 34, and is referred to as the driver area. The end of the shell nearest the driver was the third area of integration. Axial points 18 to 20 and circumferential points 1 to 64 comprised this area, which is referred to as the driver end area. Finally, the impulsive power due to the end of the shell farthest from the driver was computed. The integration was performed over axial points 44 to 46 and circumferential points 1 to 64 for this region and will be referred to as the non-driver end area of the shell. Figures 6.5 and 6.6 show the Impulsive power for the four areas described. These plots will be very important in explaining the first section of results. The three frequencies used in the explanation, 2966.3 Hz, 3808.6 Hz, and 4785.2 Hz, are pointed out on the plots. Finally, all four plots are shown in linear and not logarithmic scale because the impulsive power is negative for some frequencies in three of the four areas. Such an area actually absorbs sound power of that frequency instead of radiating sound power.
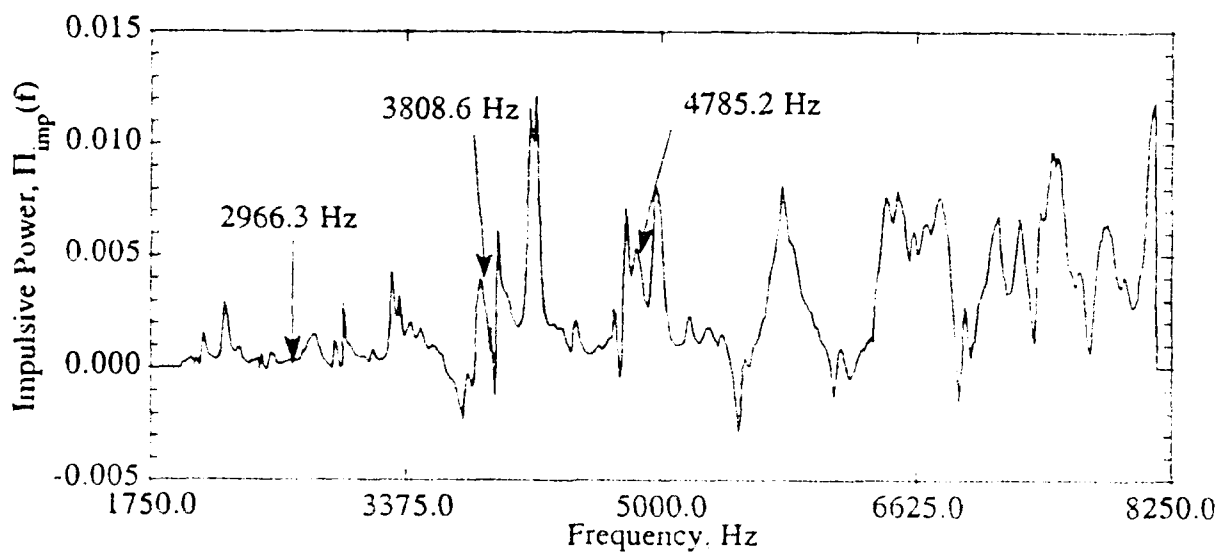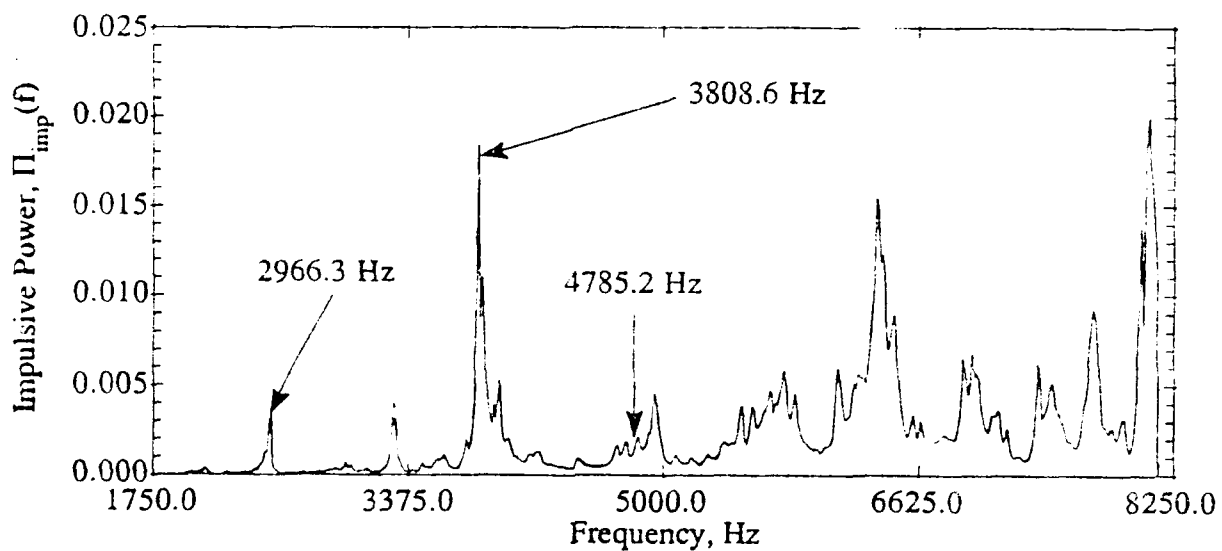
Figure 6.5: Impulsive power, $\Pi_{imp}(f)$ for a) the entire shell, and b) the driver area
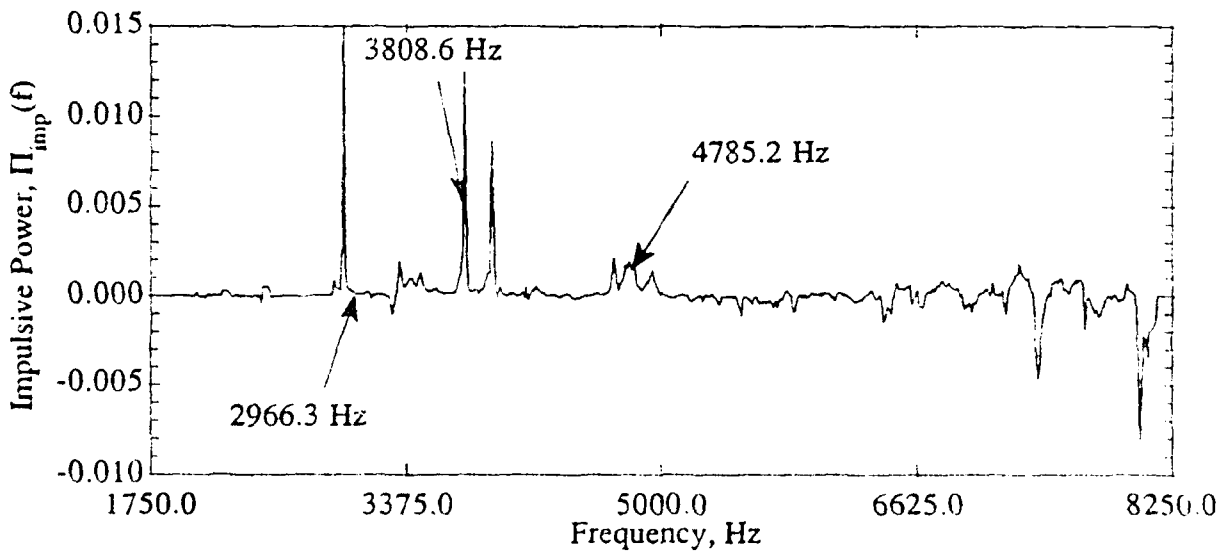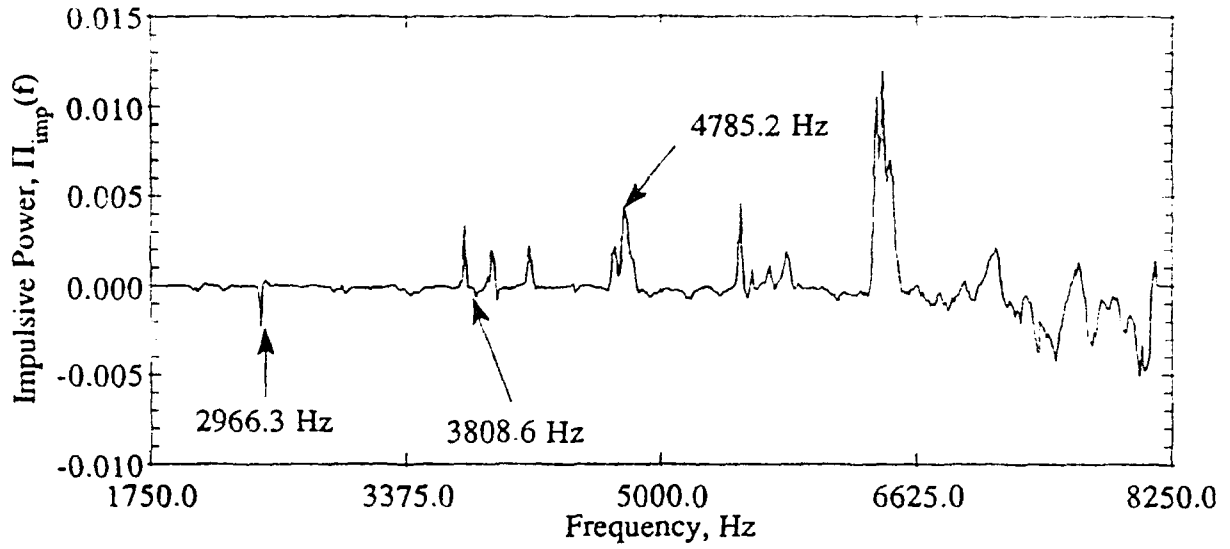
Figure 6.6: Impulsive power, $\Pi_{imp}(f)$ for a) the driver end area, and b) the non-driver end

CHAPTER 7

RESULTS AND DISCUSSION

7.1. Normalized Energy vs. Pulse Time Duration

7.1.1. Precursory

In an earlier paper (Mann et al.), it was concluded that the percent of input energy radiated as sound power for a fluid loaded, point driven, cylindrical shell increased as force time duration of a one pulse Gaussian force, increased. It appeared, however, that this conclusion was incorrect due to the very specific type of frequencies studied. It was decided that an insufficient number of frequencies of different types were studied to support the conclusion. Therefore, the study in this thesis was done to test the earlier conclusion.

Three frequencies, 2966.3 Hz, 3808.6 Hz, and 4785.2 Hz were chosen for study. The first two were chosen for duplication of the earlier results. The first, 2966.3 Hz, was reported to be a very resonant frequency of the shell by NRL, while the second was concluded to be a very acoustically radiant frequency (Mann et al. 1663). Finally, 4785.2 Hz was chosen since it occurred amidst a group of several local maxima in the impulsive power spectrum for the entire shell (look back to Figure 6.5a) and because it was reported to be both structurally resonant and acoustically radiant, though not as radiant as 3808.6 Hz, by NRL.

Normalized energy as a function of single pulse time duration was calculated for each of the three frequencies and each of the four shell areas, resulting in a total of twelve sets of results. The normalized energy vs. single pulse time duration for each area of interest was obtained by first calculating normalized energy for a synthetic force of short time duration, then calculating it again for a force of increased time duration. This process was repeated until increasing the parameter τ caused the force time duration to be so long that the energy did not converge in the 83 milliseconds available for time domain viewing. The following sections describe the results and use the impulsive power spectra to explain the results.

7.1.2 Results and Discussion

Figures 7.1 and 7.2 present the results for driving forces with a single Gaussian pulse, and with $f_0 = 2966.3$ Hz and $t_0 = 0.04$ seconds for the four shell areas described earlier. The pulse time duration variable τ was varied from 0.0004 to 0.01 seconds. A lower limit of 0.0004 seconds was required in order to keep the driving force frequency spectrum bandwidth within the 2-8 kHz range of the data, while the upper limit of 0.01 seconds was the maximum τ for which the normalized energy converged for this central driving frequency (2966.3 Hz).

In Figure 7.1a, the fraction of energy first decreases, and then increases steadily from a minimum as pulse time duration is increased. Although the results presented here are in agreement with those in the paper by Mann et. al., referred to earlier, for equal values of τ compared. However, the general trend predicted is contradicted by the extra values studied in this thesis.

Some insight into why an increase in input energy may not necessarily increase radiated energy is gained by examining the three partial shell areas. Energy radiated by the driver area, Fig. 7.1b, as well as the non-driver end area, Fig. 7.2b, steadily increases with force time duration while the driver end area absorbs more and more energy. This absorption is evidenced by the negative values for normalized energy radiated. If absorption is increased with increasing τ for this area of the shell, there may be other areas which absorb as well as other shell areas which radiate. The net result for the whole shell, as pointed out in Figure 7.1a, is that increases in absorption by such areas as the driver end was greater than increases in radiation by the driver end and other radiating areas until a τ of 0.002 sec. is reached, then increases in radiation take over.

Figure 7.1: Normalized energy, E_N, radiated vs. one pulse force time duration for
a) the entire shell and b) the driver area only, both resulting from driving
forces with $f_o = 2966.3$ Hz and $t_o = 0.04$ seconds

Figure 7.2: Normalized energy, E_N, radiated vs. one pulse force time duration for
a) the driver end area and b) the non-driver end area, both resulting
from driving forces with $f_o = 2966.3$ Hz and $t_o = 0.04$ seconds

Figures 7.3 and 7.4 present the results for single pulse driving forces with a central frequency of $f_0 = 3808.6$ Hz and a starting time delay of $t_0 = 0.04$ seconds for all four shell areas. For this frequency, τ was varied from 0.0005 to 0.02 seconds. Again, the lower limit was required to maintain force frequency spectrum bandwidth within the 2-8 kHz range, while the upper limit was the maximum τ for which radiated normalized energy converged.

In this case, the fraction of input energy radiated by the entire shell increases steadily with force time duration, as does that radiated by the driver area only. This time, however, energy radiated by the non-driver end increases sharply up to a τ of 0.004 and then decreases as τ is increased to 0.02. The driver end also has a different behavior. For smaller time durations, radiation increases steadily. But as the parameter tau is increased, the radiation from the driver end reaches a maximum, then begins to decrease until τ reaches about 0.005. After that, the driver end area absorbs an increasing fraction of the input energy as time duration is increased.

At this point in the experiment, it was expected that the normalized energy radiated by the whole shell would increase with longer time duration for a central driving frequency of 4785.2 Hz as well. However, as Figure 7.5a shows, just the opposite occurred. Normalized energy decreases, sharply at first and then more steadily, with increasing pulse time duration. The fraction of energy radiated by the driver area of the shell first increases sharply, then decreases somewhat, and finally increases slowly with increasing τ. Both ends of the shell, radiate increasing percentages of the input energy as time duration is made larger, as shown in Figure 7.6.

For both the 2966.3 Hz and 3808.6 Hz driving forces, it appears that the normalized energy for the whole shell is dominated by what is occurring at the driver area of the shell. For 4785.2 Hz, however, the driver area and entire shell area have very different behaviors. What's more, the energy radiated by the shell did not necessarily correspond to the activity on either end of the shell ends for any of the three driving frequencies.
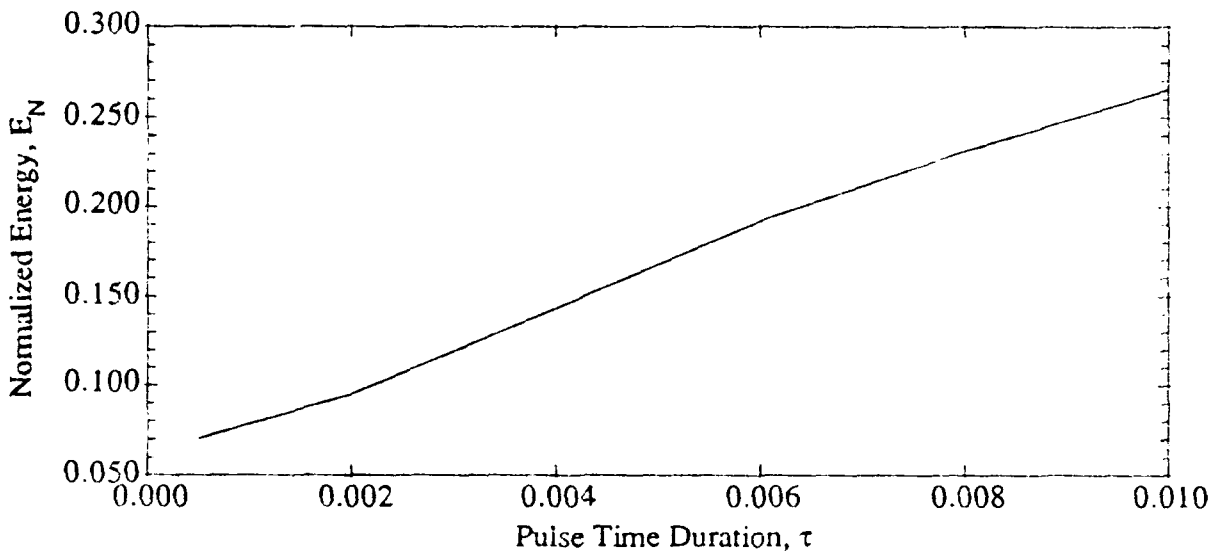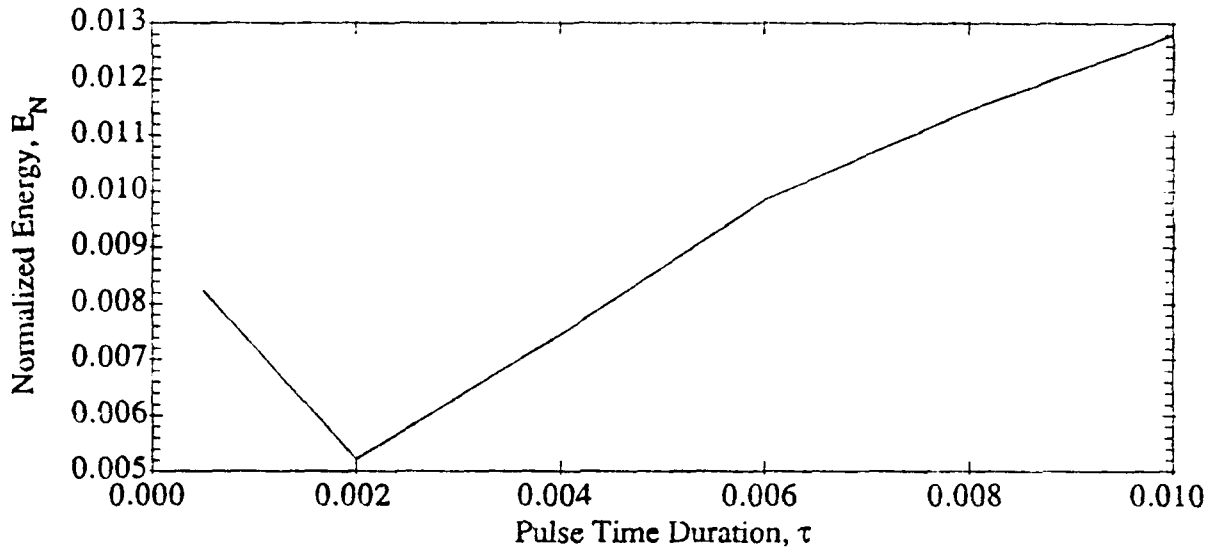
Figure 7.3: Normalized energy, E_N, radiated vs. one pulse force time duration for
a) the entire shell and b) the driver area only, both resulting from driving
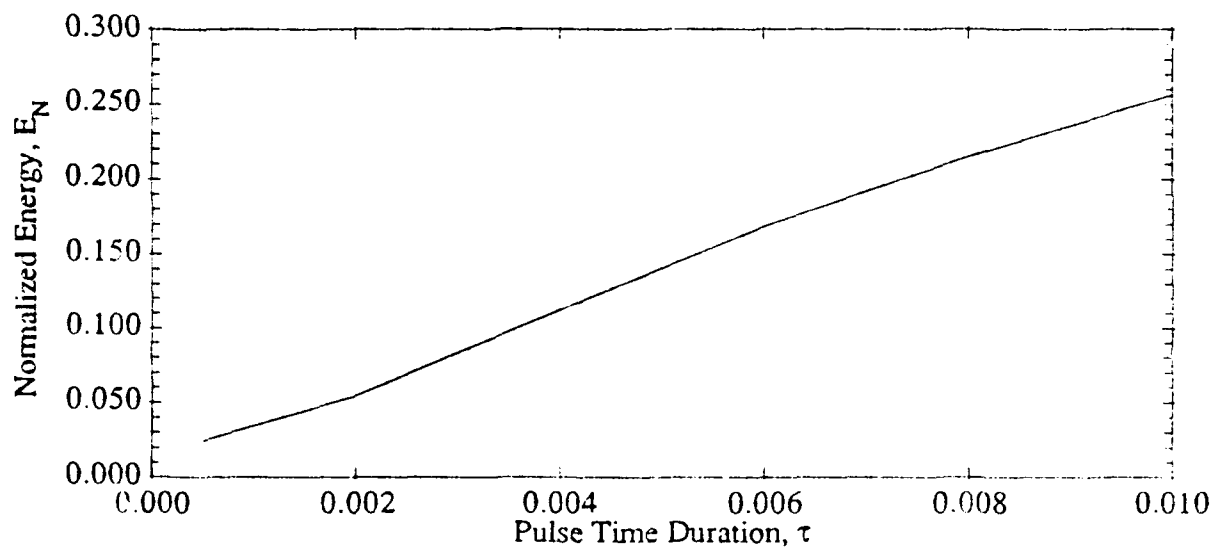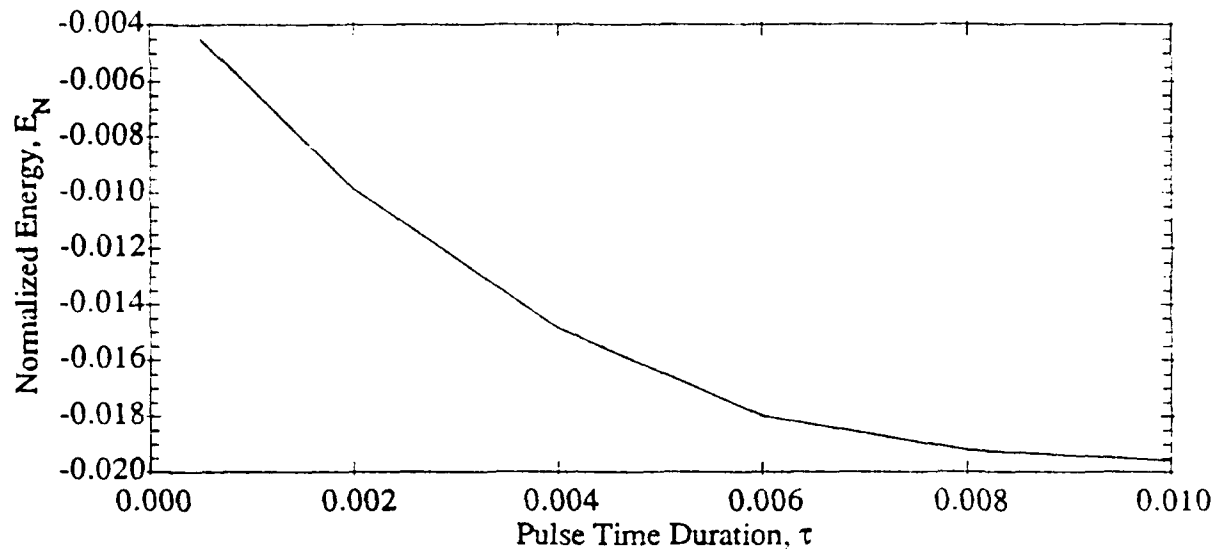forces with $f_o = 3808.6$ Hz and $t_o = 0.04$ seconds

Figure 7.4: Normalized energy, E_N, radiated vs. one pulse force time duration for
a) the driver end area and b) the non-driver end area, both resulting
from driving forces with f_o =3808.6 Hz and t_o = 0.04 seconds
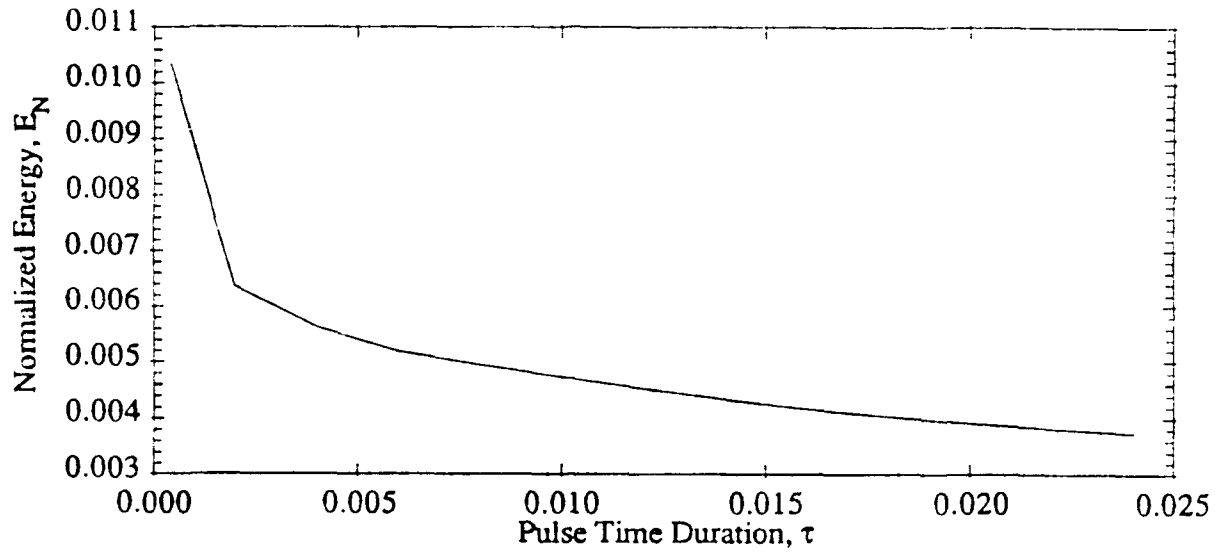
Figure 7.5: Normalized energy, E_N, radiated vs. one pulse force time duration for
a) the entire shell and b) the driver area only, both resulting from driving
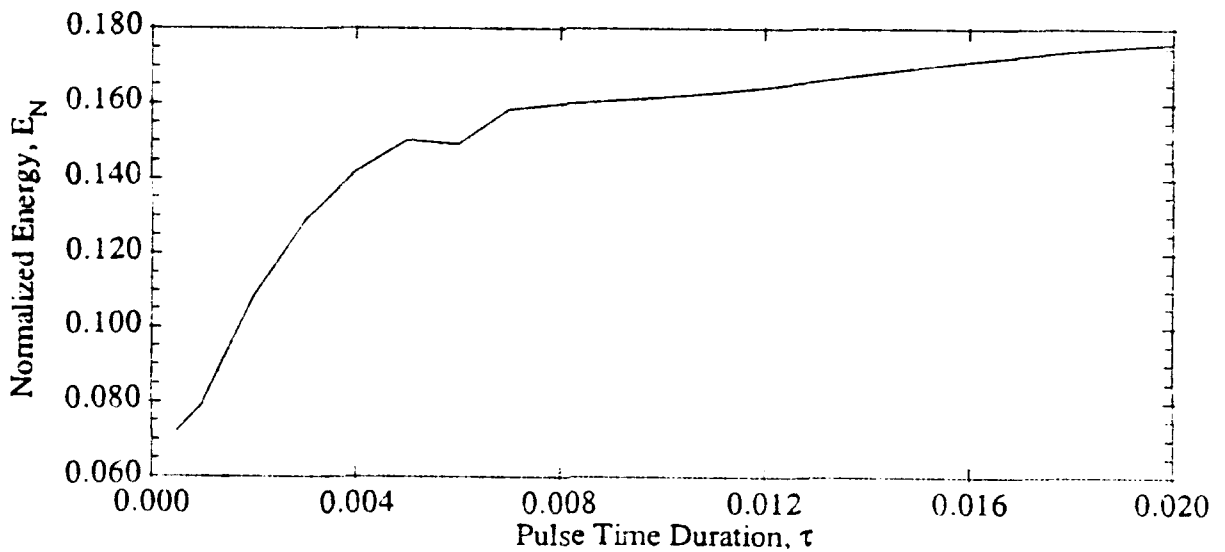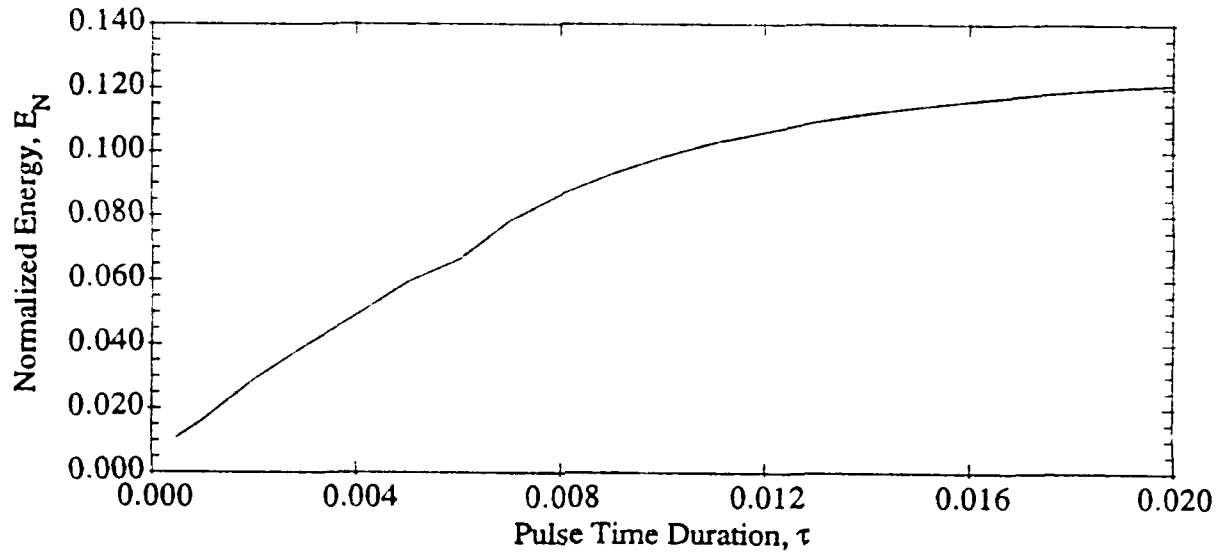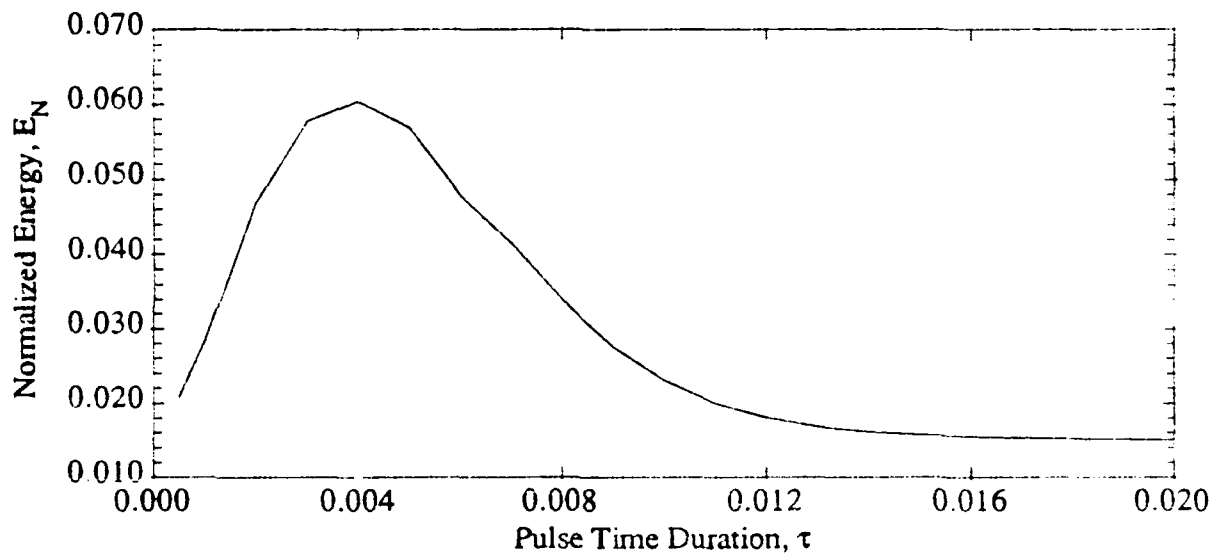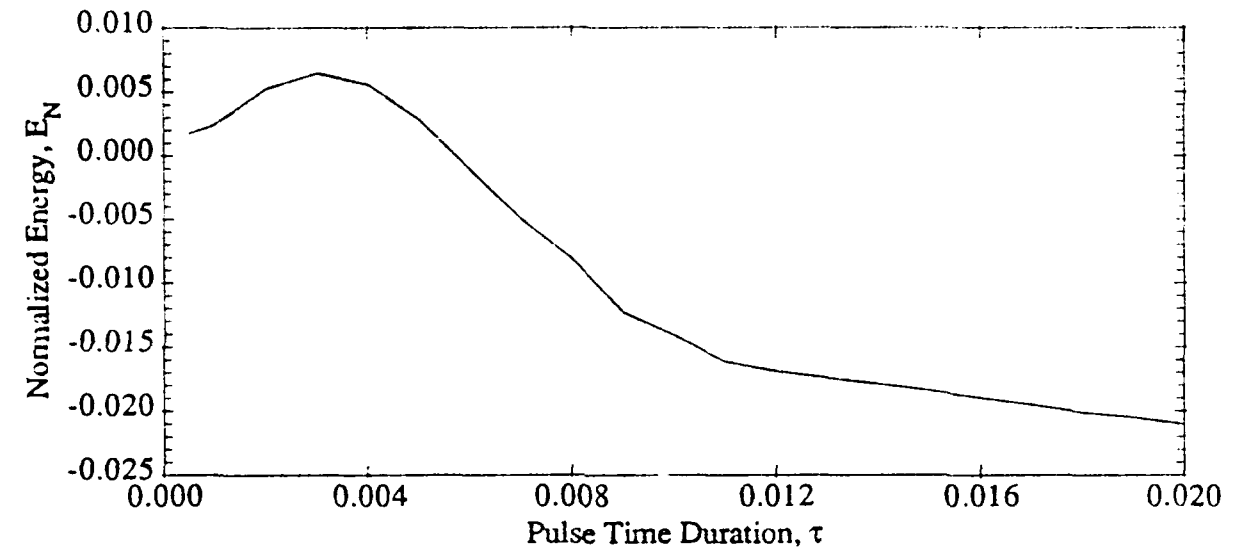forces with $f_o = 4785.2$ Hz and $t_o = 0.04$ seconds

Figure 7.6: Normalized energy, E_N, radiated vs. one pulse force time duration for
a) the driver end area and b) the non-driver end area, both resulting
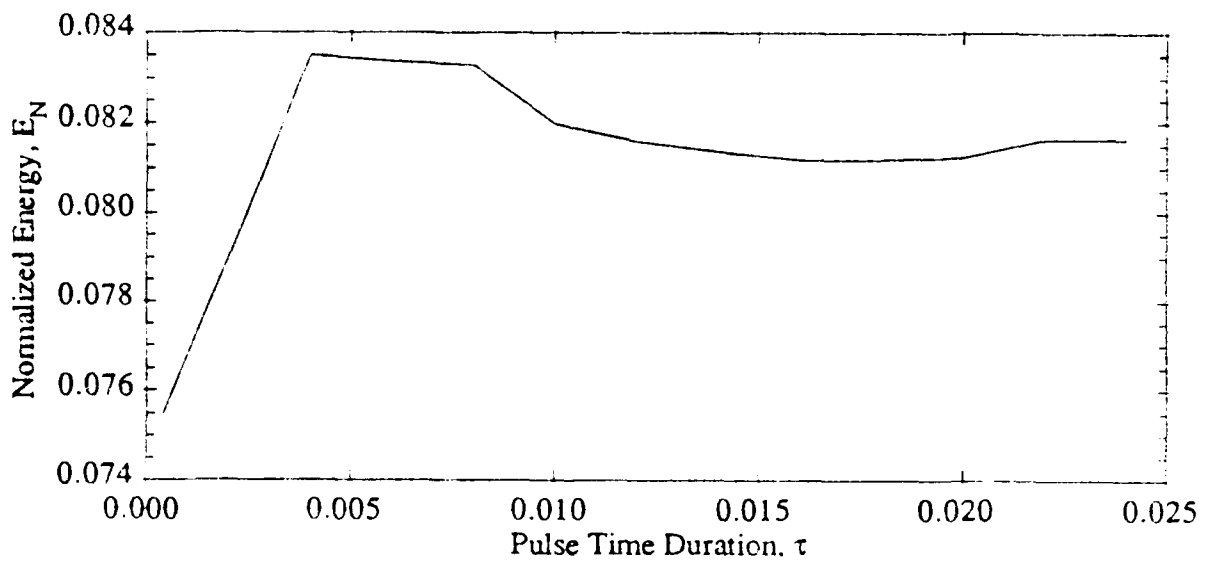from driving forces with $f_0 = 4785.2$ Hz and $t_0 = 0.04$ seconds

This fact is somewhat peculiar because some discontinuities occur on the shell in these areas that are often expected to radiate large amounts of energy (Smith 1072).

These facts, as well as the other complex behaviors noted in this section, at first appeared inexplicable from the normalized energy data obtained. But the very different behaviors of each of the shell areas was similar to the behavior of the plots of impulsive power spectra shown in the previous chapter. Therefore, impulsive power spectra will be compared to force spectra in the next section in order to explain the results.

7.1.3. Comparison of Force and Impulsive Power Spectra

Analysis of the impulsive power spectrum for the entire shell, shown in Figure 6.5a, revealed that both the 2966.3 Hz and 3808.6 Hz frequencies are very large local radiation maxima, as compared to the rest of the spectrum, for the entire shell. The 4785.2 Hz frequency, conversely, is amid four much smaller radiation peaks.

Further analysis shows that, for driver frequencies situated at local maxima in the impulsive power spectrum, energy is focused into these radiation peaks with increasing pulse time duration. This is because the frequency bandwidth is decreased while the magnitude of the force spectrum at the central frequency is increased as the pulse time duration, τ, is increased. This idea is shown more clearly in Figure 7.7 for a blown up portion of the spectrum shown in Figure 6.5a and force spectra for several pulse time durations.

On the other hand, the focus of energy into a narrower and narrower bandwidth causes a lesser quantity of normalized energy to be radiated by the shell for a driving frequency of 4785.2 Hz. This time, a blow up of the spectrum in Figure 6.5a reveals that as energy is focused into 4785.2 Hz, it is drawn away from the largest radiation peak of the four local peaks. The peak of interest is centered at approximately 4960 Hz, is about three times larger than any of the other three local maxima, and thus dominates the radiation.
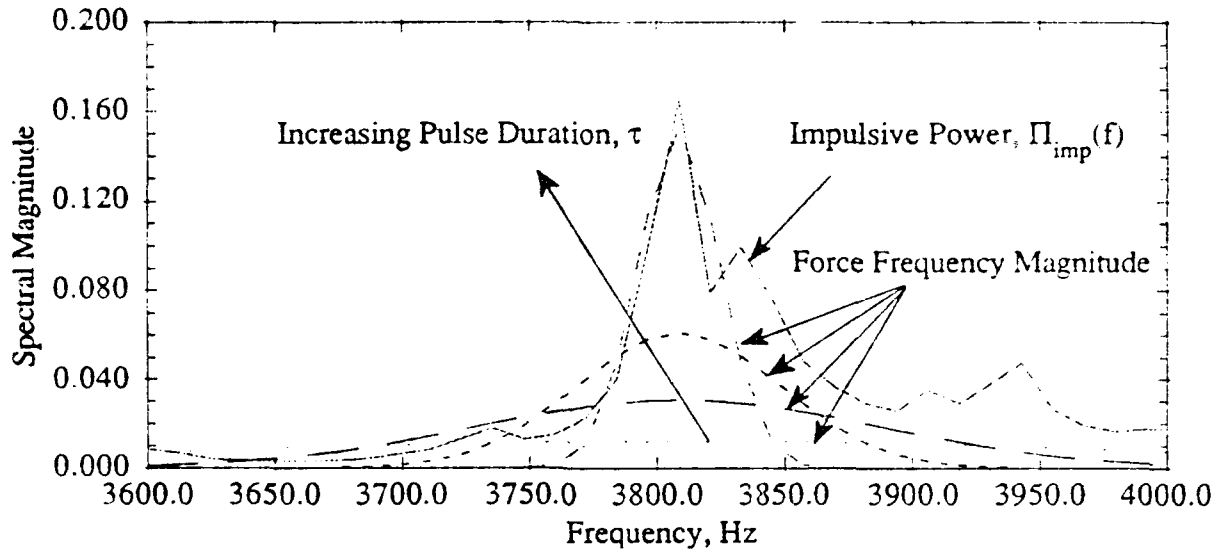
Figure 7.7: The impulsive power spectrum for the entire shell surface plotted with spectra of 3808.6 Hz driving forces for several values of tau
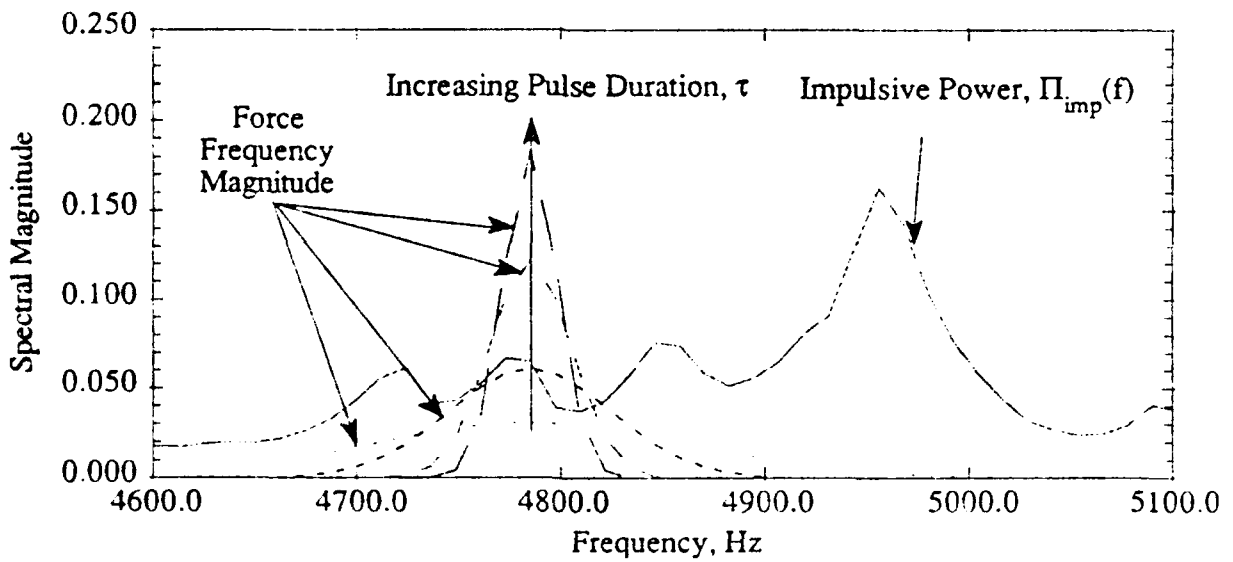
Figure 7.8: The impulsive power spectrum for the entire shell surface plotted with spectra of 4785.2 Hz driving forces for several values of tau

Similar observations are possible for the other results presented in this section. The pattern of normalized energy radiated or absorbed may be explained by examining the impulsive power spectrum for the desired area near the frequency of interest. In some instances, however, predicting a result is not as qualitatively obvious as the two cases expounded upon in this section. A quantitative resolution of this problem is left to further work.

A major consequence of this analysis is that no general relationship exists between force time duration and the fraction of input energy radiated to the farfield of the fluid. Thus, to achieve minimization of radiated energy, the impulsive power spectrum must be examined to determine the relationship between percent of input energy radiated and pulse time duration for each individual driving frequency. If a qualitative determination is not possible, the analysis can still be done in the time domain.

7.2. Normalized Energy vs. Two Pulse Time Spacing

<u>7.2.1. Precursory</u>

After relationship between pulse time duration and shell radiation was determined, it was suspected that including additional pulses to the forcing function might have a significant effect on the normalized energy radiated as well. Specifically, multiple pulses might lead to active sound cancellation for the shell, depending on the initial conditions at the time additional driving pulses are applied to the shell. Further, it was desired to know which initial conditions for additional pulses resulted in active sound cancellation.

Only two of the previous three frequencies, 3808.6 Hz and 4785.2 Hz, were chosen for this analysis. The major reason for this is that a 2966.3 Hz driver frequency causes the shell to vibrate much longer than the other frequencies. Therefore, it was not possible to include more than one individual pulse and still attain convergence in the normalized energy. Also, it was desired to include both types of frequencies described and used in section 7.1. One frequency ocurring at a large local maximum of the impulsive acoustic power spectrum, and another not

occuring at a large maximum were used in the multiple pulse time spacing study.

To address all of the possible initial conditions, it was decided to start with a pulse time spacing of s = 0.0 seconds, and increase the spacing one time bin (40 μsec) at a time until the maximum spacing at which convergence of the normalized energy was achieved. Some initial experiments with the normalized energy revealed that only forces with two pulses were feasible for shell excitation in order to attain normalized energy convergence for a two pulse time spacing of approximately s ≤ 0.01 seconds for both Gaussian force central frequencies. A pulse time duration parameter, τ, of 0.005 seconds was chosen for both central driving frequencies for the purpose of convergence as well. Further, an initial driving force time delay of t_0 = 0.0125 seconds was required for both the 4785.2 Hz and the 3808.6 Hz experiments to accommodate convergence requirements.

The results were obtained in the same fashion as those for the time duration experiment, only in this case the spacing between the two pulses was the variable. Reviewing quickly, the normalized energy value for a two pulse driver force, much like that in Figure 5.4, was calculated. Then the spacing was increased one time bin to 40 microseconds and normalized energy was calculated again and plotted as a function of s (time spacing). This process was repeated over and over until normalized energy from a driver force consisting of two distinct pulses, similar to Figure 5.5, was achieved. The process was continued until the maximum pulse separation for which the normalized energy converged was achieved. Results were calculated for the same four shell areas, the whole shell, the driver only, the driver end, and the non - driver end, as the pulse time duration results.

7.2.2. Results and Discussion

Figures 7.9 and 7.10 plot normalized energy vs. two pulse time separation for two pulse driving forces with a central frequency of 3808.6 Hz and a pulse time duration of τ = 0.005 seconds for the four areas of the shell. Figures 7.11 and 7.12 plot normalized energy

Figure 7.9: Normalized energy, E_N, radiated vs. two pulse force time separation for
a) the entire shell and b) the driver area only, both resulting from driving
forces with $f_0 = 3808.6$ Hz, $t_0 = 0.0125$ seconds, and $\tau = 0.005$

Figure 7.10: Normalized energy, E_N, radiated vs.two pulse force time separation for
a) the driver end area and b) the non-driver end area, both resulting
from driving forces with f_0 =3808.6 Hz, t_0 = 0.0125 seconds, and τ = 0.005

vs. two pulse time separation for forces with the same parameters except with a central frequency of 4785.2 Hz. In all eight of these plots, the normalized energy for a two pulse time spacing of zero seconds is the same as that for a one pulse force with $\tau = 0.005$ seconds and the same central frequency. This is because a two pulse force with zero space between pulses is really the same as a one pulse force with twice the amplitude. Normalized energy levels for one pulse forces of the same central frequency and time duration as the two pulse force were read from Figures 7.3 through 7.6 for each shell area and are plotted in Figures 7.9 through 7.12 for the corresponding shell area. The one pulse normalized energy is a thick straight horizontal line pointed out in each of the plots. Plotting this value on the same graph as the normalized energy vs. two pulse time spacing points out that the fraction of input energy radiated to the farfield is much less than one pulse for some spacings and much more for others.

Another observation pertaining to all eight plots in this section is that the fluctuations in normalized energy values have a definite period as the two pulse time spacing is increased. Namely, they oscillate in a nearly sinusoidal (or cosinusoidal) fashion. The frequency of oscillation is the same frequency as the central frequency of the excitation force. An explanation for this fact will be given in section 7.2.4.

Much like the results for single pulse forces, the results for two pulse forces varied for different regions of the shell. For forces with a central frequency of 3808.6 Hz, normalized energy values for the entire shell were as much as one and a half times that of a single pulse and as little as one third that of a single pulse. Normalized energy values greater than that for a one pulse force indicate that the two pulses are acting together to increase the fraction of input energy radiated by the shell. When normalized energy values are less than that for a single pulse, the second pulse is actively cancelling out energy that would have been radiated by the first pulse.
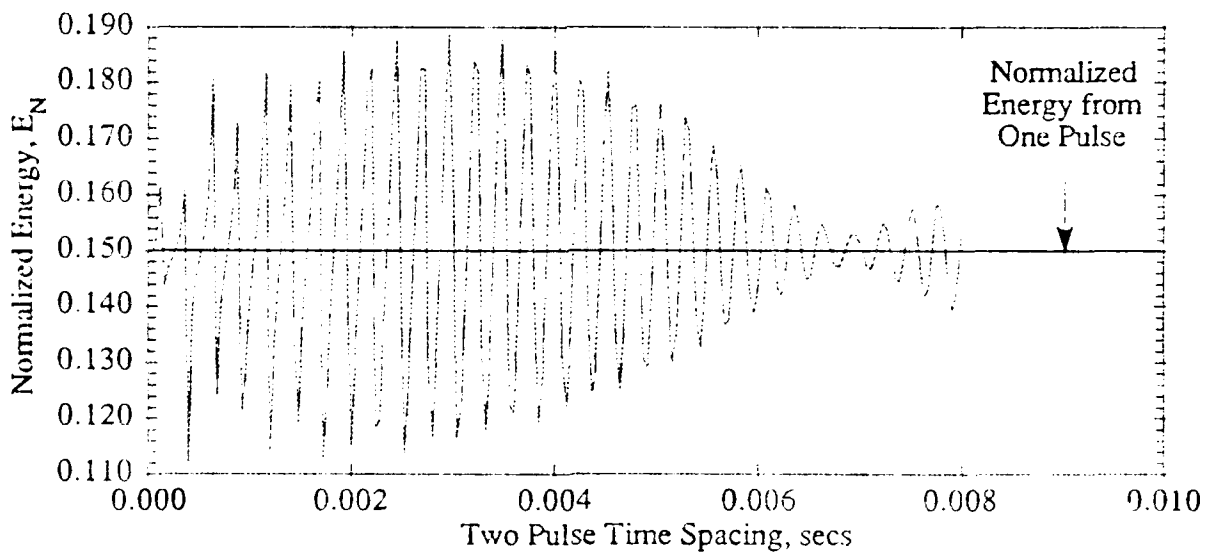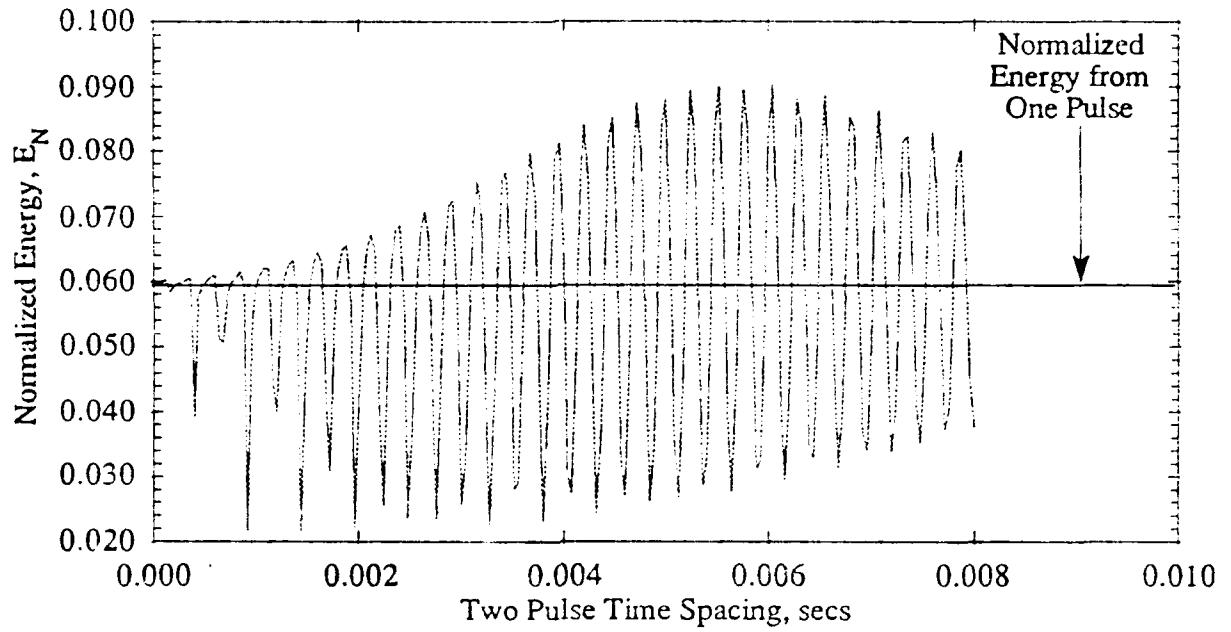
Figure 7.11: Normalized energy, E_N, radiated vs.two pulse force time separation for
a) the entire shell and b) the driver area only, both resulting from driving
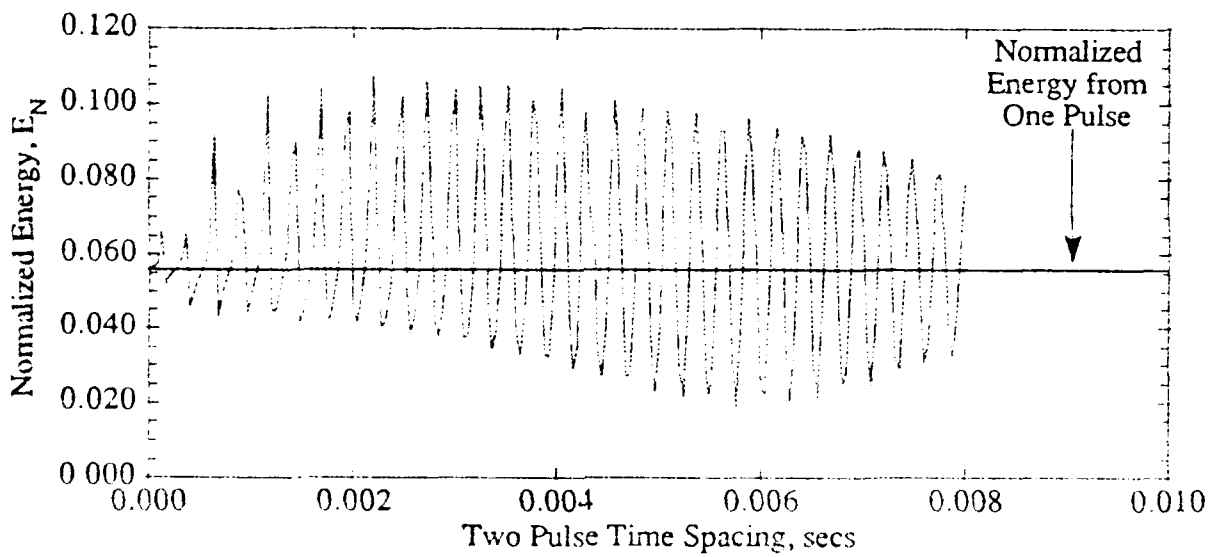forces with $f_o = 4785.2$ Hz, $t_o = 0.0125$ seconds, and $\tau = 0.005$
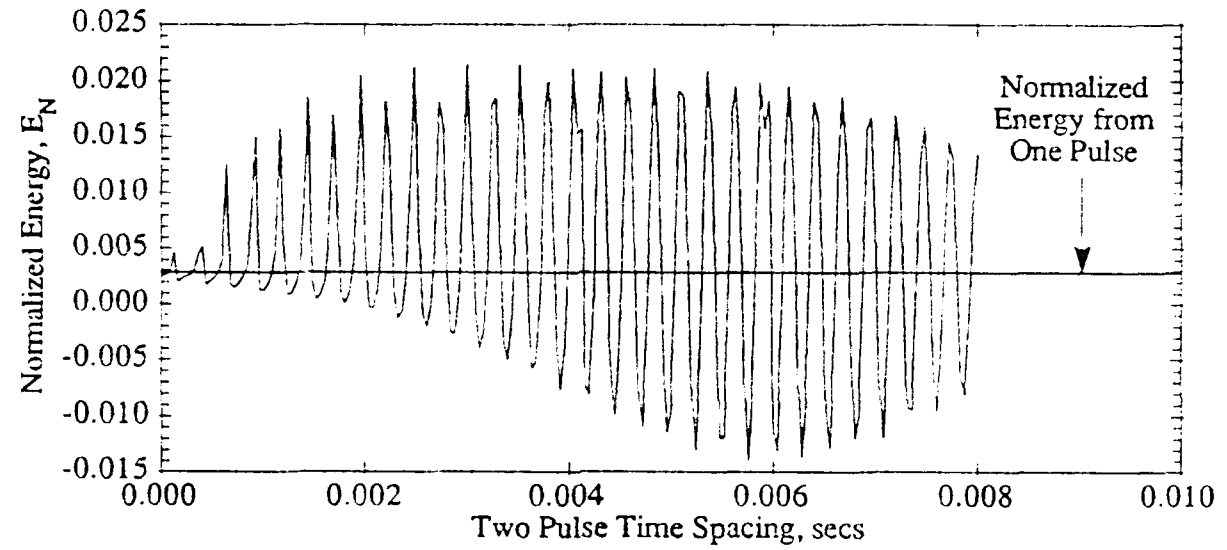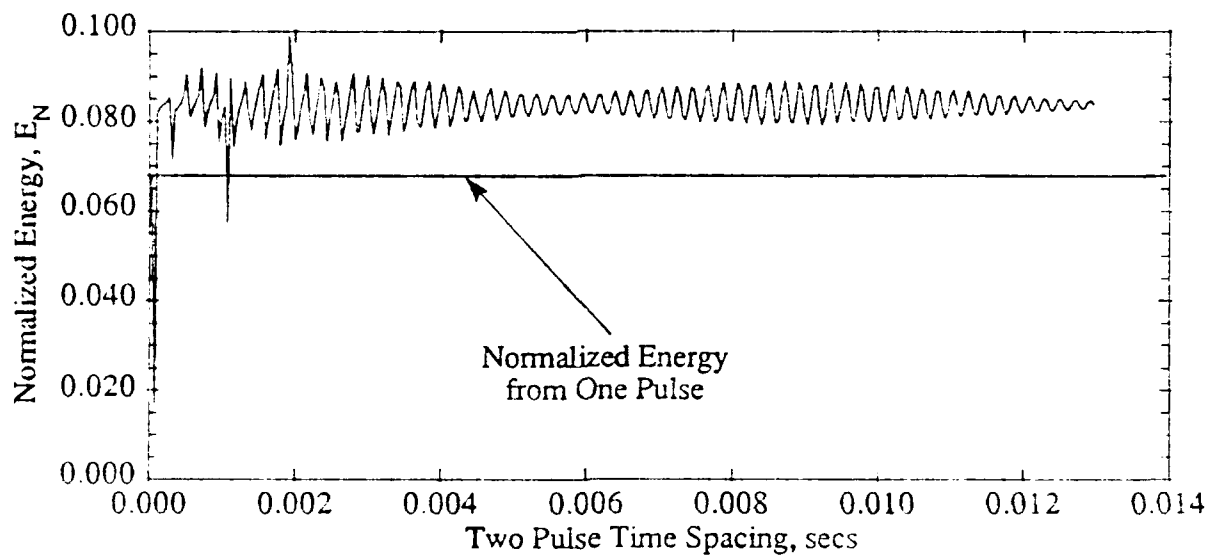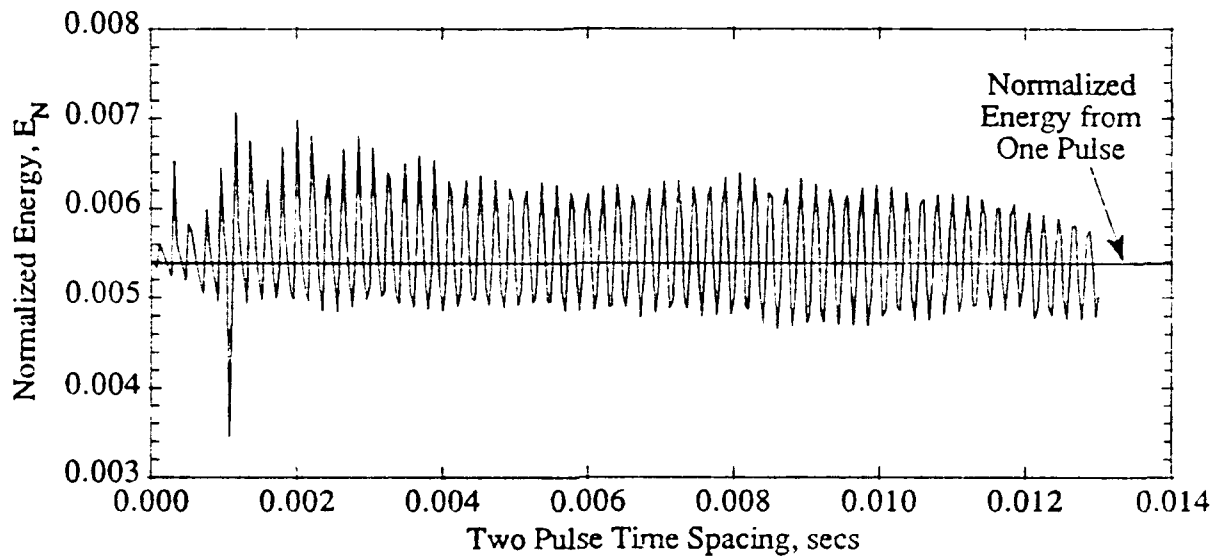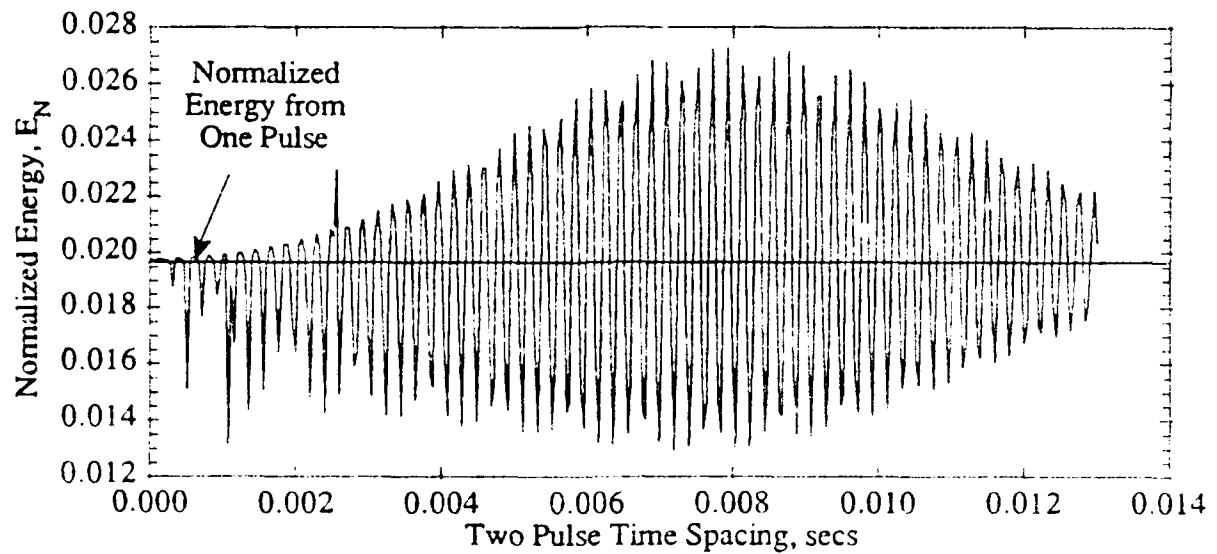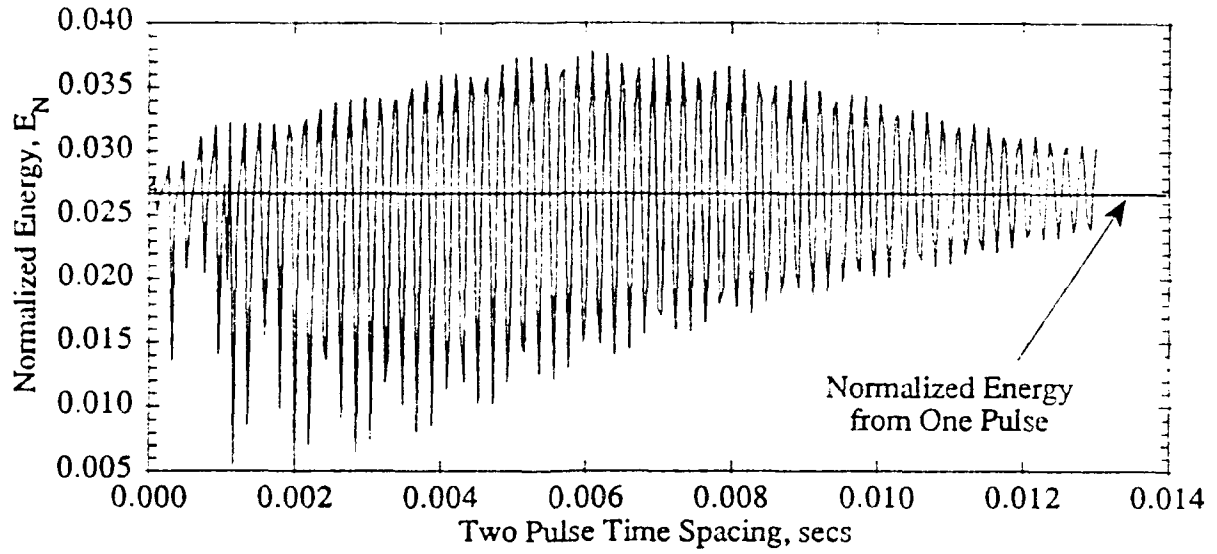
Figure 7.12: Normalized energy, E_N, radiated vs.two pulse force time separation for
a) the driver end area and b) the non-driver end area. both resulting
from driving forces with $f_0 = 4785.2$ Hz, $t_0 = 0.0125$ seconds, and $\tau = 0.005$

A key feature of Figure 7.9a is that normalized energy is reduced by as much as fifty percent for certain two pulse time separations. Figure 7.9b shows that oscillation of the normalized energy for the driver area decays to the normalized energy of one pulse and then begins to build up again. This fact would seem to indicate the presence of a beat frequency in the oscillation of the normalized energy in addition to the oscillation which matches the central frequency of the driving forces. Beat frequencies occur to a lesser degree in the other seven plots as well. Figure 7.10a is interesting because normalized energy values for the driver end of the shell become negetive for some two pulse time spacings as the pulse separation, s, is increased. This means that sound energy is alternately being radiated and then absorbed by this area of the shell.

When the central frequency of two pulse excitation forces was increased to 4785.2 Hz, the amount of active cancellation of sound energy obained for the entire shell, as shown in Figure 7.11a, was much less than that achieved for 3808.6 Hz. Only at a two pulse spacing of s = 1.2 milliseconds was the normalized sound energy decreased by as much as a third. The normalized energy seemed to oscillate only slightly from the one pulse value as two pulse time spacing was increased. Oscillations in normalized energy for the driver area remained greater than the normalized energy of one pulse for all but two values of s. Figure 7.11b shows than only one of these spacings, s = 120.0 microseconds, resulted in a normalized energy value of less than half the one pulse value for the driver area. Large cancellations are observed for both ends of the shell, as shown in Figure 7.12. However, the normalized energy radiated by the entire shell seemed to be dominated by the driver area. Evidence of this fact is the small variation in normalized energy for both the entire shell and the driver area.

7.2.3. A Look At Active Intensity

Active intensity is a tool used to gain physical insight when dealing with radiating structures. Since the amount of active cancellation obtained for the entire shell was quite

different for the two frequencies of section 7.2.2, the presence of a major difference in the physical behavior of the shell was evident. Active intensity proved quite useful in pointing out this difference.

Figures 7.13, 7.14, 7.16, and 7.17 show the active intensity, $I(\phi,z)$, for the entire shell when driven by various forces with two pulses. Figures 7.15 and 7.18 show differences in the active intensity. Axial points $z = 19$ to $z = 45$ and circumferential points $\phi = 1$ to $\phi = 64$ of the measurement surface are plotted since they correspond to the shell surface. Other points in the measurement surface outside the shell are not displayed because the amount of the sound radiated by the shell leaving through these points is negligible. The coordinates of the driver point, $\phi = 33$, $z = 25$, are pointed out on all plots in this section. Active intensity and difference in active intensity values are rep. ʻnted by 100 different shades of grey in the plots. Values are scaled so that the largest value is black and the smallest value is white.

Figure 7.13 displays the active intensity for a driving force with two pulses and $f_0 = 380.6$ Hz, $t_0 = 0.0125$ seconds, $\tau = 0.005$ seconds, and $s = 0.0$ seconds. This spacing corresponds to a point where normalized energy radiated is equal to the value for one pulse in Figure 7.9a. Since active intensity values range from positive to negative, black regions represent places where a large amount of sound energy is exiting the shell and white areas represent areas where a large amount of energy is entering the shell. Thus, black areas represent areas radiating sound while white areas represent areas absorbing sound. The color of grey in the strip along the left edge of the plot represents an area which is neither radiating nor absorbing energy. The aspect of this plot that is most important is that a large percentage of the area of the shell, particularly over and near the driver is radiating large amounts of sound. Meanwhile, only a small portion of the shell is absorbing sound in large quantities. Two areas, one in the top center and one in the bottom center of the plot, appear to be radiating or absorbing energy in much smaller quantities compared to the other areas previously noted.

In Figure 7.14, active intensity is plotted for a force consisting of two pulses where all

Figure 7.13: Active intensity, $I(\phi,z)$, for the entire shell resulting from a driving force with $f_o = 3808.6$ Hz, $t_o = 0.0125$ seconds, $\tau = 0.005$ seconds, and $s = 0.0$ seconds

Figure 7.14: Active intensity, $I(\phi,z)$, for the entire shell resulting from a driving force with $f_o = 3808.6$ Hz, $t_o = 0.0125$ seconds, $\tau = 0.005$ seconds, and $s = 0.00012$ secs.
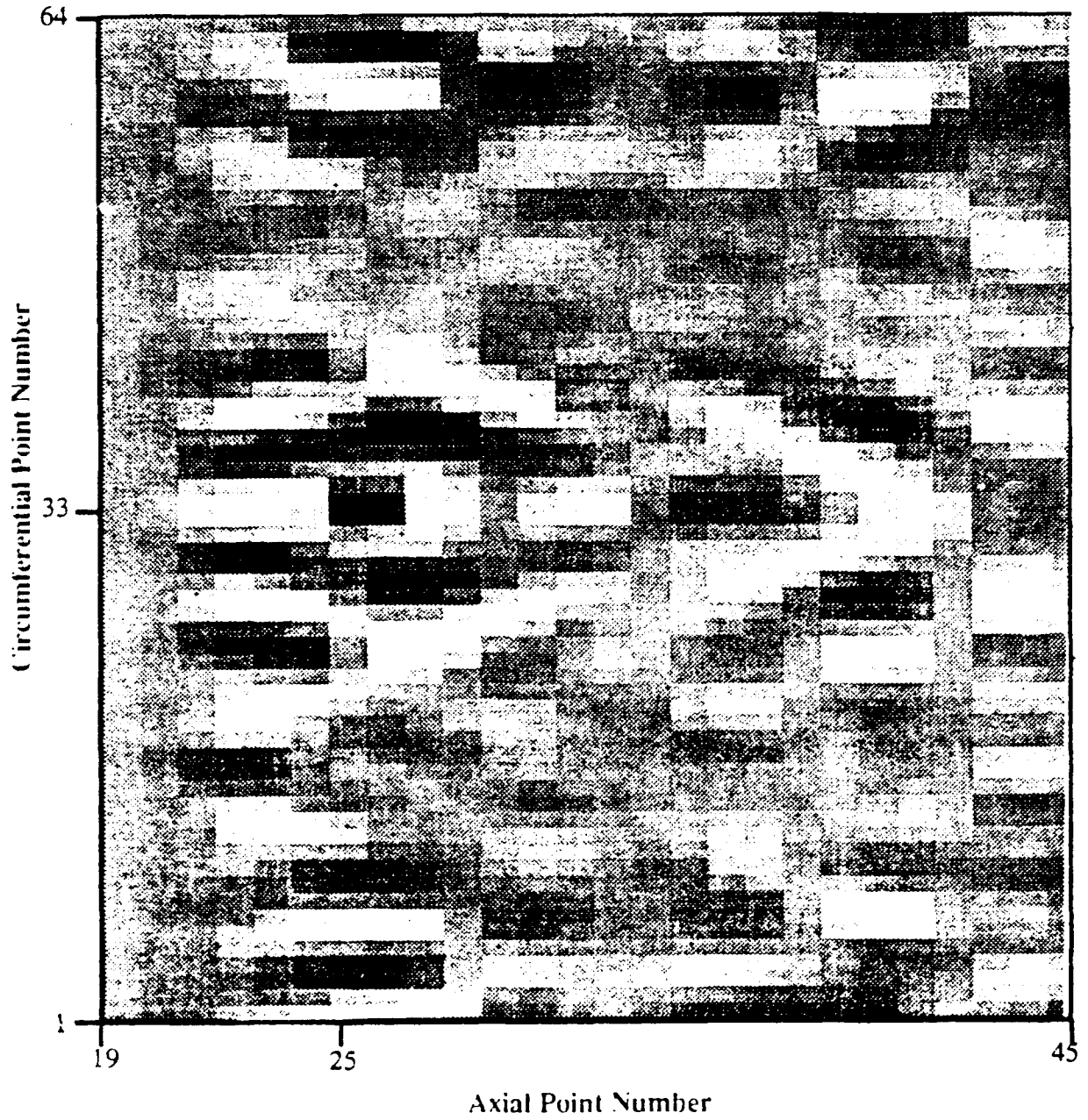
Figure 7.15: Active intensity from Figure 7.13 minus active intensity from Figure 7.14

force parameters are the same except s = 0.00012 seconds. This force spacing corresponds to the first dip in Figure 7.9a which has a normalized energy value that is below 0.004, significantly less than the value for a single pulse. Radiation and absorption patterns in this plot are almost exactly the same as those in Figure 7.13.

Plotted in Figure 7.15 is the active intensity for a pulse spacing with maximum E_N minus that for a spacing which results in a large active cancellation. The subtraction was done point by point. In this plot, black represents areas where this difference is large and positive while white areas represent places where the difference is large and negative. Thus black regions in the plot represent shell areas where the force with s = 0.0 seconds caused the shell to radiate much more sound than the force with s = 0.00012 seconds. White regions show where the force with s = 0.0 seconds caused the shell to absorb more energy than the force with s = 0.00012 seconds. Areas with the same grey coloring described in Figure 7.13 show little change when the spacing is increased. The most interesting feature of this plot is that the same areas which radiated or absorbed a lot of sound for s = 0.0 showed the largest difference in amplitude when the spacing was increased to 0.00012 seconds. This fact is evidenced by the similarity in appearance between all three plots. Figure 7.15 indicates, therefore, that a two pulse time spacing of 0.00012 seconds caused a decrease in the percentage of sound radiated by the shell by decreasing the amplitude of radiation, or absorption, in the areas of the shell where they are largest.

Figures 7.16 to 7.18 show the same comparison as that done in Figures 7.13 to 7.15, only this time a central frequency of f_0 = 4785.2 Hz was used. All other parameters were the same for Figures 7.13 and 7.16, and Figures 7.15 and 7.17, respectively. Again, the spacing s = 0.00012 seconds corresponded to a normalized energy value in Figure 7.11a that was below that for one pulse. In these plots, however, only three areas on and near the driver point appear to be radiating sound in significant amounts. A few other areas throughout the shell appear to be absorbing energy in significant quantities, but most of the shell is absorbing or
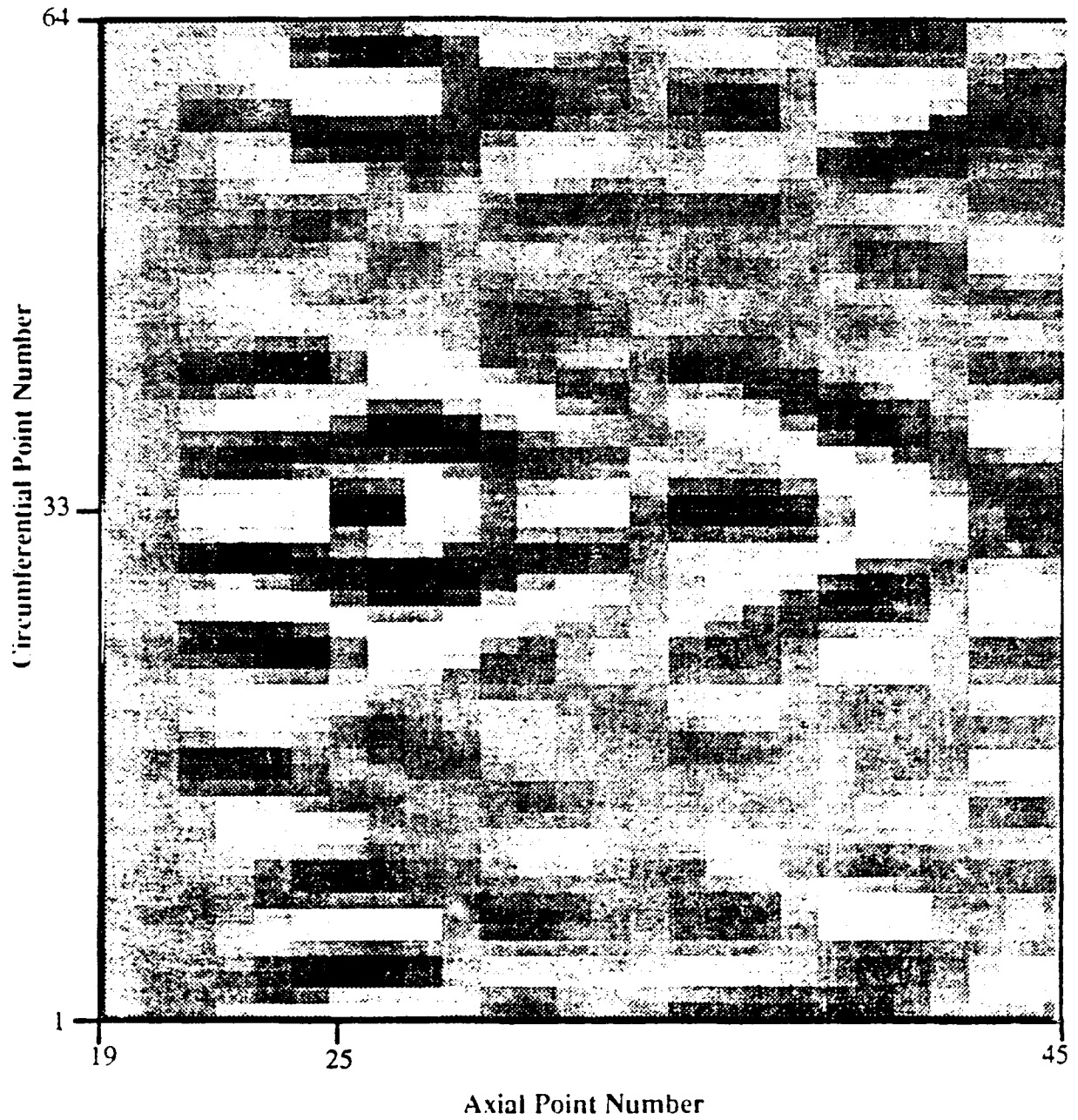
Figure 7.16: Active intensity, $I(\phi,z)$, for the entire shell resulting from a driving force with $f_0 = 4785.2$ Hz, $t_0 = 0.0125$ seconds, $\tau = 0.005$ seconds, and s = 0.0 seconds
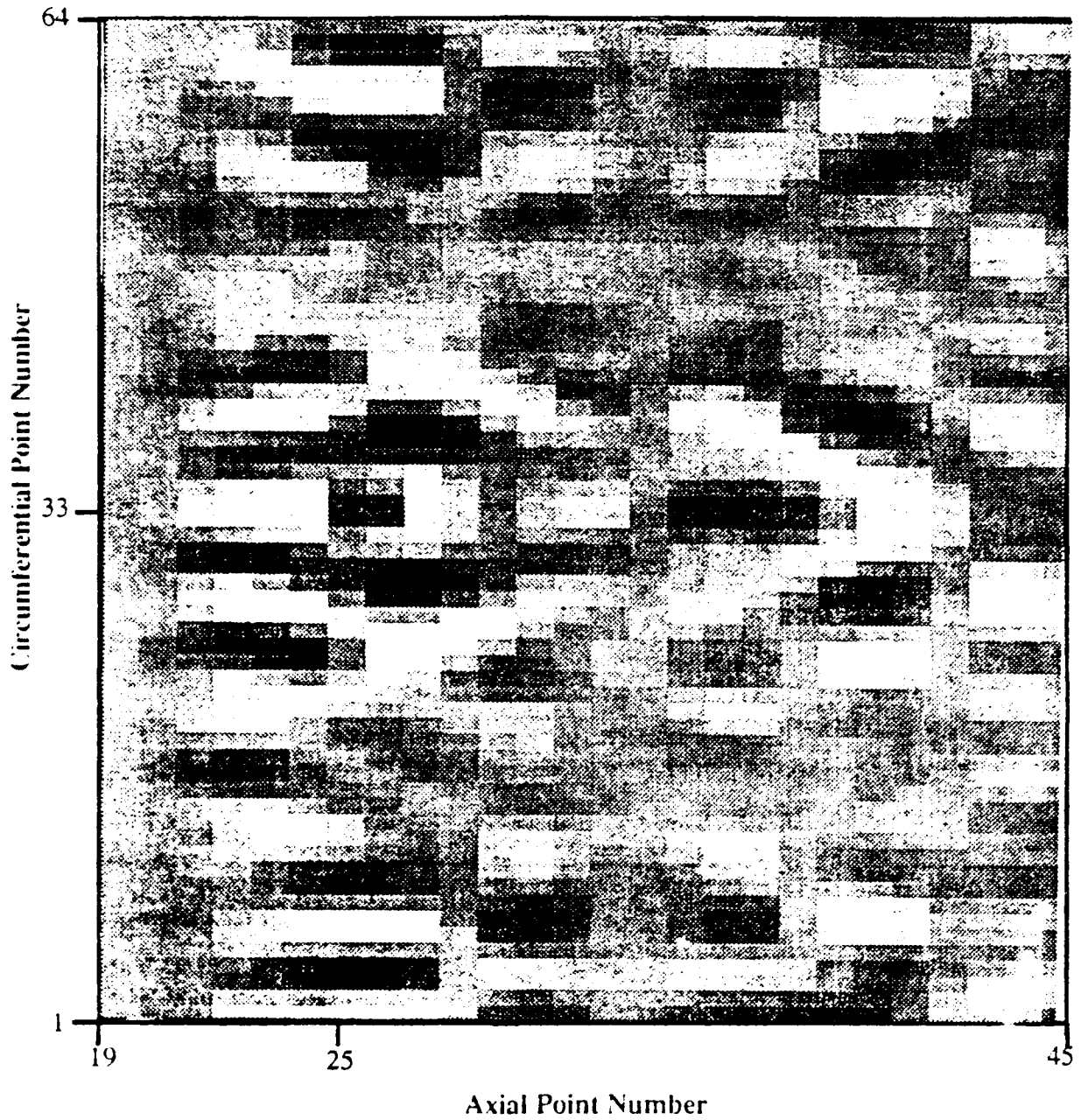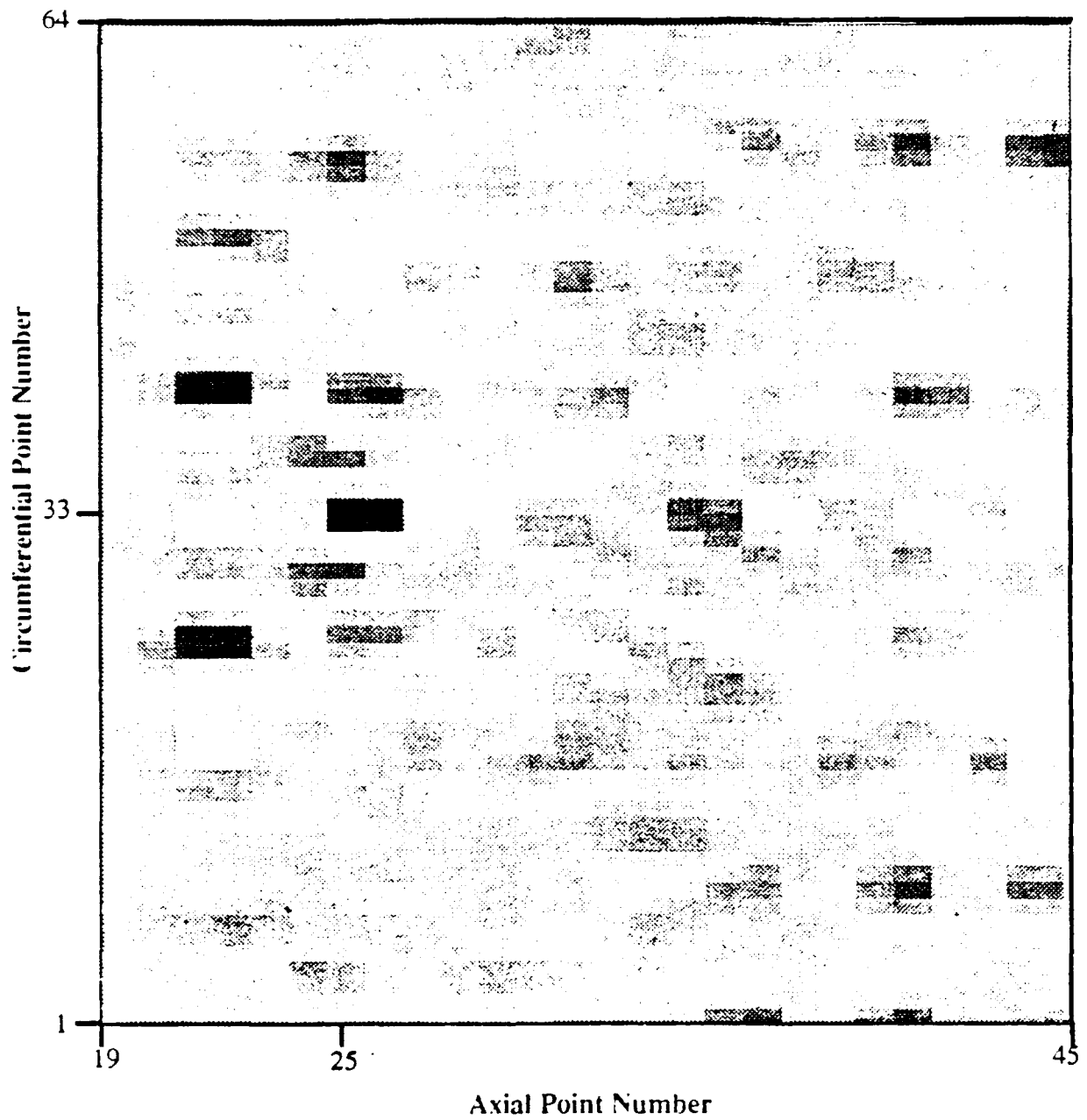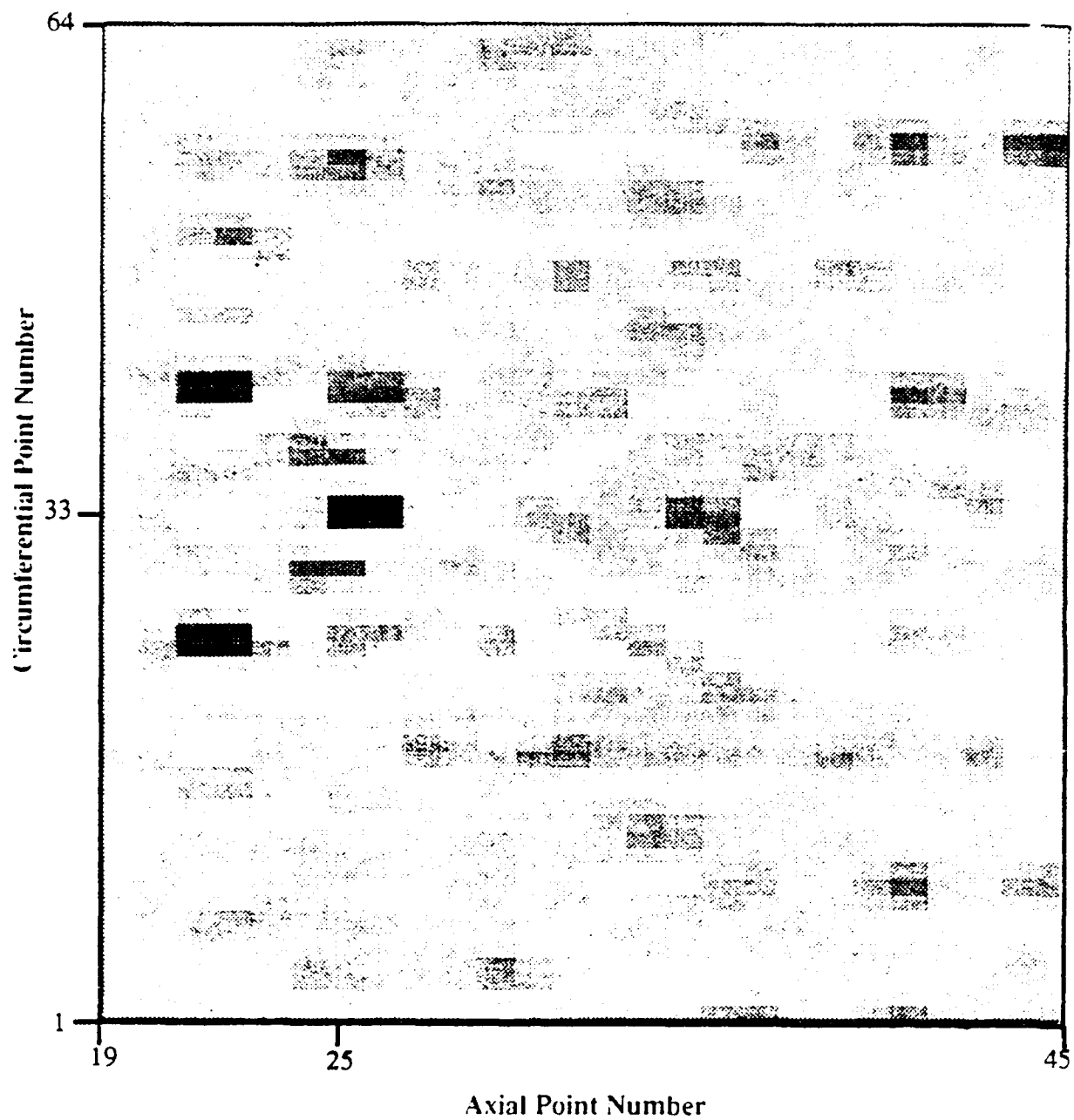
Figure 7.17: Active intensity, $I(\phi,z)$, for the entire shell resulting from a driving force with $f_o = 4785.2$ Hz, $t_o = 0.0125$ seconds, $\tau = 0.005$ seconds, and $s = 0.00012$ secs.
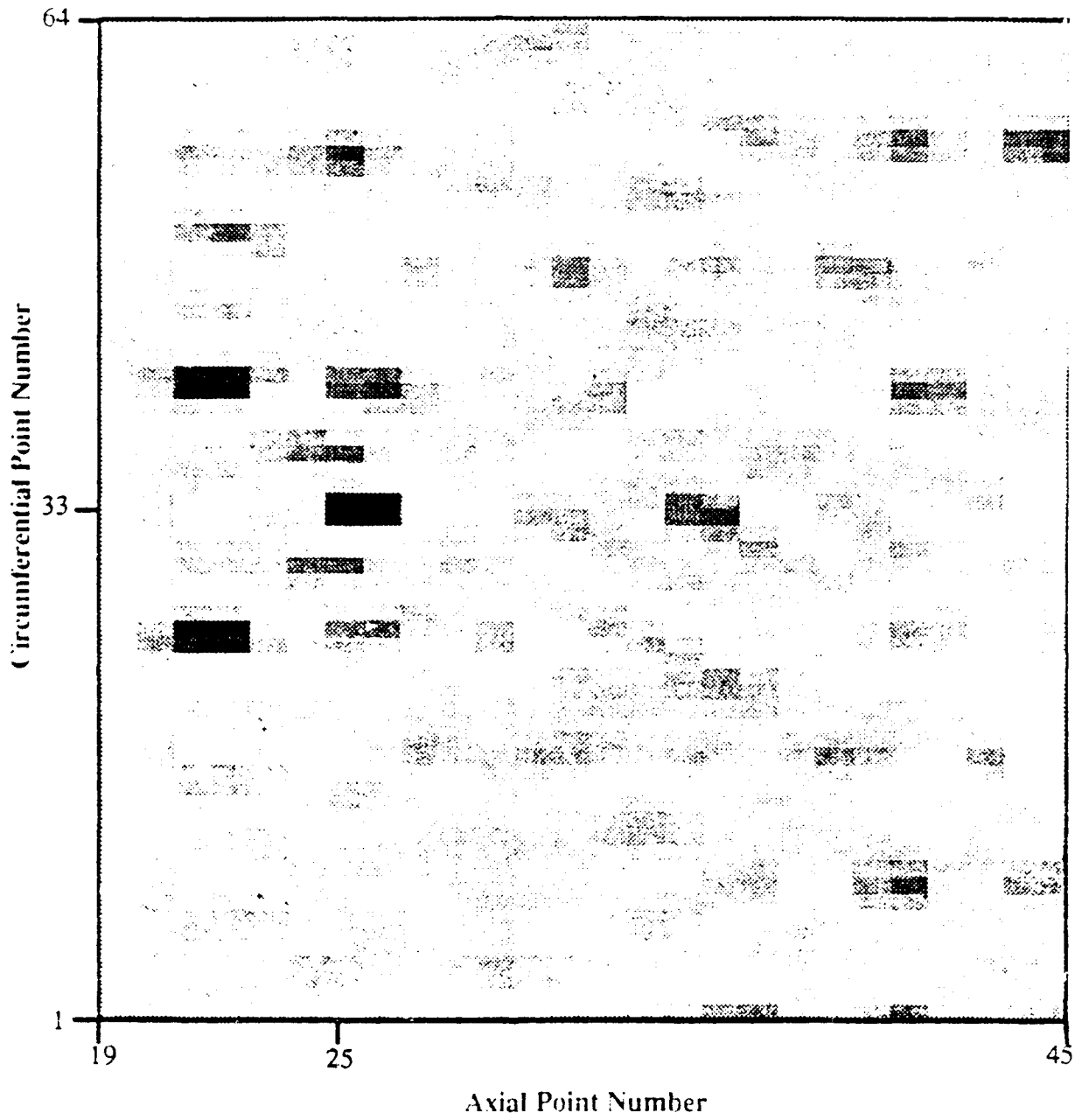
Figure 7.18: Active intensity from Figure 7.16 minus active intensity from Figure 7.17

radiating sound in much smaller quantities than the white or black areas shown in the plots. Once again, all three plots have a very similar appearance, indicating that only amplitudes were changed and not the position where radiation or absorption occur.

The most significant difference noticed when the two sets of plots are compared is that when the shell is driven by forces with $f_0 = 3808.6$ Hz, much more variation in absorption and radiation levels is observed than for forces with $f_0 = 4785.2$ Hz. Therefore, it is concluded that forces with a center frequency of 3808.6 Hz radiate a higher percentage of input energy because they cause more areas of the shell to radiate than those with a center frequency of 4785.2 Hz. Also, a larger difference in the amount of normalized energy radiated is observable when two pulse time spacing is varied for forces with $f_0 = 3808.6$ Hz than for those with $f_0 = 4785.2$ Hz because the former cause the shell to have more areas which can have a significant change in radiation or absorption.

Although this analysis does little to explain why, in terms of the shell structure, the behavior of the shell is so different for the two central frequencies studied, it does point out a similarity between the pulse time duration and two pulse time spacing results. Specifically, that the amount normalized energy radiated by the shell is different for different shell areas for both studies. Therefore, the impulsive acoustic power will be used to explain the results for normalized energy as a function of time spacing for forces with two pulses in the next section.

7.2.4. Impulsive Power Spectrum Model

Modeling the variation in normalized energy as a function of the time spacing between two force pulses in terms of the impulsive acoustic power is begun by examining the excitation force as a function of frequency. Equation (5.2.6) is repeated for $N = 2$ and the dependence on x_0 left out,

$$F_{syn}(f) = (\tau/2) (e^{2\pi j f t_o} + e^{2\pi j f [t_o + s]}) \; e^{-\pi \{(f - f_o)\tau\}^2} + e^{-\pi \{(f + f_o)\tau\}^2} , \qquad (7.2.1)$$

In this case F(f) is the sum of two individual one pulse forces. Call these two forces $F_1(f)$ and $F_2(f)$, such that $F(f) = F_1(f) + F_2(f)$. Equation (7.2.1) shows that F_1 and F_2 are equal except for a time shift, s, the time spacing between the two pulses. Thus, for a two pulse force in the frequency domain,

$$F_1(f) = F_2(f) \cdot e^{-j2\pi fs}. \tag{7.2.2}$$

and

$$F(f) = F_1(f) \cdot [1 + e^{-j2\pi fs}]. \tag{7.2.3}$$

This expression can also be written as,

$$F(f) = F_1(f) \cdot e^{(-j2\pi fs)/2} \cdot [e^{(j2\pi fs)/2} + e^{(-j2\pi fs)/2}], \tag{7.2.4}$$

or more conveniently as

$$F(f) = 2 \cdot F_1(f) \cdot e^{(-j2\pi fs)/2} \cdot \cos[(2\pi fs)/2]. \tag{7.2.5}$$

Next, recall the expression for total energy radiated by the shell in Equation (6.4.1) which related the product of the forcing function and its complex conjugate to the impulsive acoustic power in the frequency domain. Computing the product of the force with two pulses in Equation (7.2.5) and its own complex conjugate via

$$F(f) \cdot F^*(f) = 2 \cdot F_1(f) \cdot F_1^*(f) \cdot [\cos(2\pi fs) + 1], \tag{7.2.6}$$

and substitute this result into Equation (6.4.1), the result is

$$E_{tot} = \int_{-\infty}^{\infty} 2 \cdot F_1(f) \cdot F_1^*(f) \cdot \Pi_{imp}(f) df + \int_{-\infty}^{\infty} 2 \cdot F_1(f) \cdot F_1^*(f) \cdot \Pi_{imp}(f) \cos(2\pi fs) df. \tag{7.2.7}$$

Further analysis reveals that $F_1(f)$ times its own conjugate is merely the magnitude of F_1 squared. Thus, when the total energy is normalized by the total input energy of the forcing

function, the normalized energy, E_N, can be thought of as

$$\Xi_N = \int_{-\infty}^{\infty} \alpha(f) \cdot \Pi_{imp}(f) df + \int_{-\infty}^{\infty} \alpha(f) \cdot \Pi_{imp}(f) \cos(2\pi fs) df, \qquad (7.2.8)$$

where

$$\alpha(f) = \frac{[F_1(f) \cdot F_1^*(f)]}{E_{in}} = \frac{|F_1(f)|}{E_{in}}. \qquad (7.2.9)$$

Hence, α is a constant of proportionality related to the magnitude of the forcing function at a given frequency and the input energy, E_{in}, given in Equation (6.2.5).

Now suppose that, instead of an impulsive acoustic power spectrum with many frequencies as shown in Figures 6.5 and 6.6, the impulsive acoustic power spectrum being studied has values greater than zero at only two frequencies, f_0 and f_1, where f_0 is the central frequency of the excitation force containing two pulses. This idea is shown pictorially in Figure 7.19.
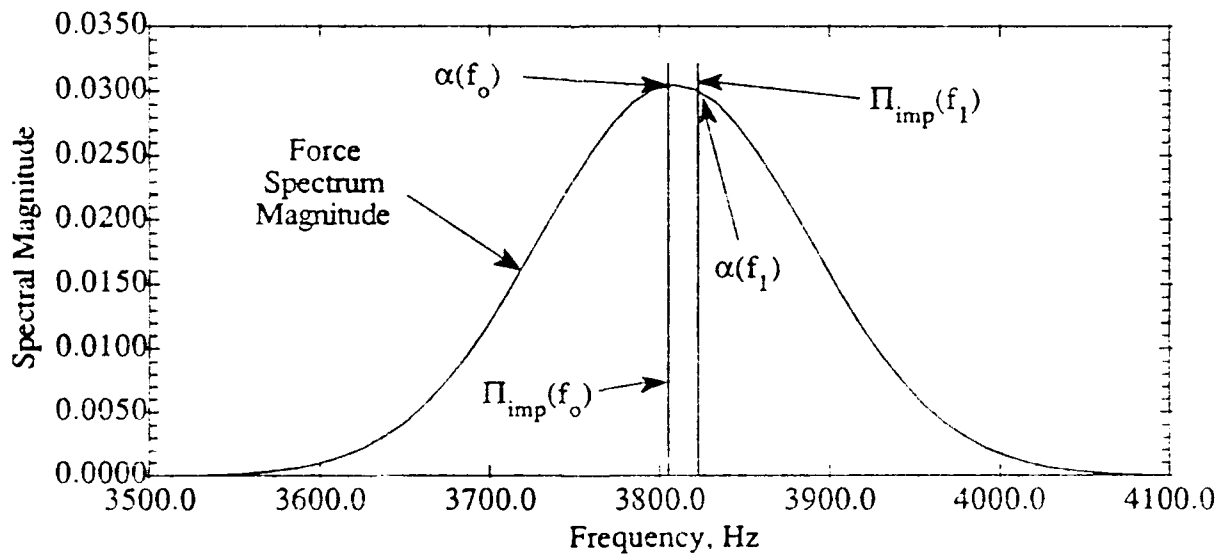

Figure 7.19: Diagram of an impulsive acoustic power spectrum consisting of only two frequencies, f_0 and f_1, where f_0 is the center frequency of the driving force spectrum shown in the diagram

Then, according to Equations (7.2.8) and (7.2.9), the normalized energy as a function of two

pulse spacing, s, for such a spectrum is the sum,

$$E_N = \alpha(f_o) \cdot \Pi_{imp}(f_o) \cdot [1 + \cos 2\pi f_o s] + \alpha(f_1) \cdot \Pi_{imp}(f_1) \cdot [1 + \cos 2\pi f_1 s] . \quad (7.2.10)$$

Further, if $\alpha(f_o) \; \Pi_{imp}(f_o) = \alpha(f_1) \; \Pi_{imp}(f_1)$ then

$$E_N = [\alpha(f_o)\Pi_{imp}(f_o) + \alpha(f_1)\Pi_{imp}(f_1)] \; (1 + \cos \pi (f_o + f_1) s + \cos \pi (f_o - f_1) s) . \quad (7.2.11)$$

As an example Equation (7.2.10) was computed for the case where $f_0 = 3808.6$ Hz,

$f_1 = 3881.8$ Hz and $\alpha(f_o) \; \Pi_{imp}(f_o) = \alpha(f_1) \; \Pi_{imp}(f_1) = 1.0$. Two pulse spacing was varied from

s = 0.0 to s = 10.16 milliseconds, and the results displayed in Figure 7.20. After examining

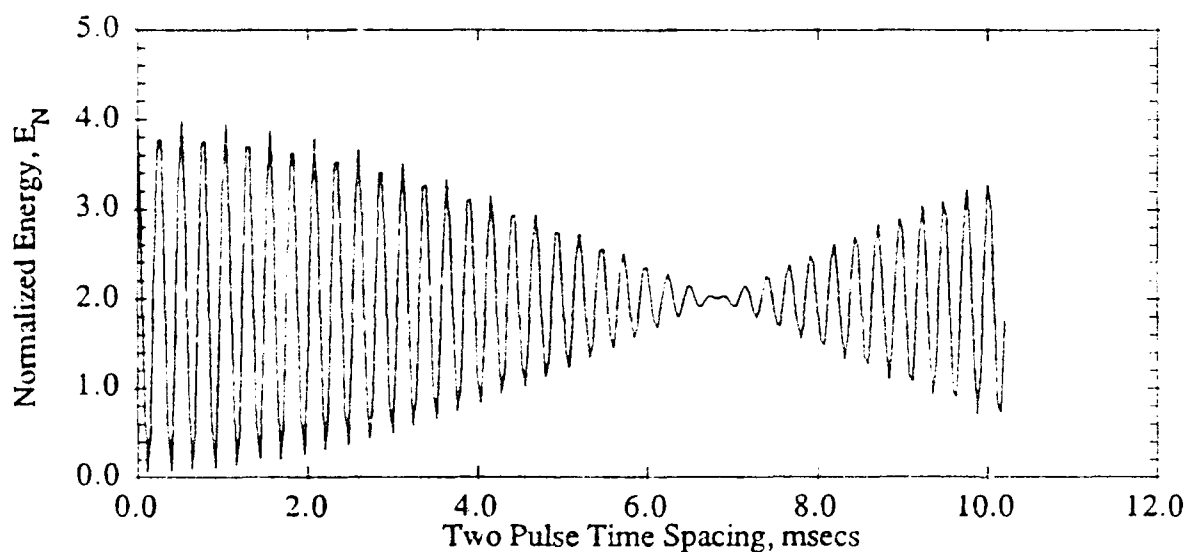Figure 7.20: Computed result of Equation (7.2.10) for $f_0 = 3808.6$ Hz, $f_1 = 3881.8$ Hz, and
$\alpha(f_o) \; \Pi_{imp}(f_o) = \alpha(f_1) \; \Pi_{imp}(f_1) = 1.0$

Eq. (7.2.11) closely, it is obvious that the normalized energy is oscillating with a frequency of

(3808.6 + 3881.8) / 2, and is windowed by a beat frequency of (3881.8 - 3808.6) / 2. Close

study of Figure 7.20 confirms this observation.

It is now very apparent that the impulsive acoustic power model describes what is happening with the normalized energy in Figures 7.9 to 7.12, even though the impulsive power spectra for these plots consist of many frequencies, as shown in Figures 6.5 and 6.6. In fact, the plot in Figure 7.20 bears a good deal of resemblance to that shown in Figure 7.9a.

The main oscillation in the plots occurs at a frequency close to f_0 because $\alpha(f_0) \Pi_{imp}(f_0)$ will be much larger than for any other frequency due to the Gaussian nature of the force magnitude. Thus, f_0 dominates the integration over all frequencies in Equation (7.2.9). All of the graphs in Figures 7.9 to 7.12 appear to begin their oscillations at the same normalized energy values as that for the one pulse force for the same area and time duration. According to Equation (7.2.10), this value, for the special case we are considering in this section, is $\alpha(f_0) \Pi_{imp}(f_0) + \alpha(f_1) \Pi_{imp}(f_1)$, when the space between pulses is zero and appropriate f_0 and f_1 are chosen for each case. This value will not oscillate because the pulse spacing will never change, but will depend on the variation in $\alpha(f)$ for each frequency in the excitation force spectrum as force time duration is varied.

CHAPTER 8

CONCLUSIONS

8.1. Summary and Conclusions

To properly calculate the total sound energy radiated by a structure via computer simulation, the quantity must converge within the total sample time of the original measurement. Ensuring that this is so is only possible by computing, in the time domain, the total sound energy radiated for some of the forces. Then a judgement can be made on the point of energy convergence for each type of force to be used for simulation of sound.

Results from the first study, the relationship of single pulse force time duration to normalized energy radiated by the shell, exposed the fact that the calculation of energy is not linear. The percentage of input mechanical energy acoustically radiated by the shell is found to depend on how the forcing function spectrum interacted with the spectrum of the impulsive acoustic power for the region of the shell being studied, and is not dependent, in general, on the amount of mechanical energy input to the shell. For a frequency occurring at a large local maximum in the impulsive acoustic power spectrum, normalized energy increases with increasing pulse time duration. This is because the corresponding narrowing of the force frequency bandwidth and increase in force spectrum magnitude around the central frequency of the forcing function cause more input energy to be focused into the local maximum of the impulsive acoustic power spectrum. Conversely, energy is focused away from a larger peak, which occurred next to the small local maximum in the impulsive power spectrum, as pulse time duration is increased for the other central frequency studied. Thus, if one is designing a forcing function which will minimize sound radiation, the impulsive power spectrum must be studied to determine if long or short pulse durations are needed for a particular central frequency of the driver. Such subjective observations are much tougher to make for situations where the behavior of the impulsive acoustic power spectrum is not so obvious. Proposing a

method to make predictions quantitatively is left to recomendations for further work.

In the second study, varying the time spacing between pulses of a force with two pulses caused fluctuations in the normalized energy radiated by the shell. The fluctuations oscillate at the same frequency as the central frequency, f_0, of the excitation force. Again, the results can be predicted for simpler situations by simultaneously examining the force and impulsive power spectra. Then a two pulse spacing which produces the least amount of sound raciation can be found and used when designing a forcing function for active cancellation. A simple model using r impulsive acoustic power spectrum existing at only two frequencies, one of them being the center frequency, f_0, of the driving force, is sufficient for understanding the basic variations observed in normalized energy results for force with two pulses of various time spacings. Further development of this model, as well as a means for chosing coefficients when $\alpha(f_0) \Pi_{imp}(f_0) \neq \alpha(f_1) \Pi_{imp}(f_1)$, and predicting exact values of normalized energy is left for further work.

8.2. Recomendations for Further Work

The first step in carrying on further work on this research would be to produce a computer alogorithm that would accurately predict the results obtained in Chapter 7. Once convergence of the total sound energy radiated by the shell is established for all forces to be used, the total energy radiated could be calculated via Equation 6.4.2 and then normalized by Equation 6.2.6. All frequencies in the impulsive acoustic power spectrum would be taken into account, and no subjective determination of which two frequencies could accurately model the normalized energy for a given situation would need to be made. Also, exploration of a means to model the impulsive acoustic power spectrum with more than two frequencies, say five or ten, but less than the entire spectrum is necessary.

This would save a great deal of time compared to the current method because the impulsive power would only have to be calculated once. The force spectrum and its conjugate would be multiplied by the impulsive power only once, instead of the 1024 (64 times 64)

required to multiply the force by each of the two transfer functions. The parameter of interest, either time duration or two pulse time spacing, could be varied and then the normalized energy calculated much more quickly. Another possibility is to include an option that would search for the type of force which produced the lowest fraction of input energy radiated to the farfield. This capability would then point out the force or forces which are correctly designed for minimal sound radiation. Further work in this direction would follow directly from the work done in this thesis.

However, the next step would be more difficult. This step would be to try to understand which initial conditions for the second pulse cause an increse in the normalized energy and which ones cause a decrease. For instance, it would be interesting to find a correlation between the fluctuations shown in acoustic pressure, velocity, instantaneous power, and the time integral of the instantaneous power, and the fluctuations in normalized energy.

Finally, it is very desirable to understand why, in terms of the mechanics of the shell structure and fluid - shell interaction, normalized energy varied the way it did in the results. It is likely that this endeavor would lead to employing modal analysis techniques on the shell. But further analysis in the time domain could also prove to be very useful.

REFERENCES

Bendat, Julius S., and Allan G. Piersol. Engineering Applications of Correlation and Spectral Analysis. New York: John Wiley and Sons, 1980.

Bracewell, Ronald N., The Fourier Transform and Its Applicatoins. 2nd. ed. rev. New York: McGraw-Hill, 1986.

Gabor, D. "Theory of Communication." J. Inst. Elec. Eng. 93, 429-457 (1946).

Mann, J. Adin, III, Earl G. Williams, Karl Washburn, and Karl Grosh. "Time-Domain Analysis of the Energy Exchange Between Structural Vibrations and Acoustic Radiation Usin Near-field Acoustical Holograph Measurements." J. Acoustical Soc. of America 90 (3), 1656-64 (1991).

Smith, P. W., Jr. "Phase Velocities and Displacement Characteristics of Free Waves in a Thin Cylindrical Shell." J. Acoustical Soc. of America 27 (6), 1065-1072 (1955) .

Tse, Francis S., Ivan E. Morse and Rolland T. Hinkle. Mechanical Vibrations: Theory and Applications. 2nd ed. Boston: Allyn and Bacon, 1978.

Washburn, Karl B., Karl Grosh, and Earl G. Willams. "Modal Nalysis of Fluid-Loaded, Axisymmetric Shells Using Nearfield Acoustical Holography Data." Proceedings of the First International Congress on Recent Developments in Air- and Structure- Borne Sound and Vibration, 155-163 (March, 1990).

Williams, Earl G., Henry D. Dardy and Karl B. Washburn. "Generalized Nearfield Acoustical Holography for Cylindrical Geometry: Theory and Experiment." J. Acoustical Soc. of America 81, 389-407 (1987).